3D Computer Modeling of Magnetrons

by

Lili Ma

A thesis submitted to the University of London in partial fulfillment of the requirements for the degree of Doctor of Philosophy

Department of Electronic Engineering
Queen Mary, University of London
United Kingdom

December 2004

TO MY FAMILY

Abstract

The research work presented in this thesis is primarily based on computer modelling of magnetrons using a 3D FDTD/PIC code called MAGIC. The usual modelling process has been substantially extended to include realistic details of two e2v technologies' S and X band magnetrons. Considerable insight into the magnetron operation has thus been obtained.

An investigation into the melting of the output coupling rods in the S band MG5193 magnetron revealed that multipacting taking place between the coupling rods and the central support rod is the most likely cause, rather than an RF mismatch or RF current overheating. Also, a good agreement between the simulated and measured frequency spectrum of the S band MG5193 anode has been achieved by suitably adjusting the dimensions of the bare anode, the strapping system and the 'tuner'.

Possible reasons for the high overall efficiency of the X band MG5241 magnetron model have been investigated by modelling the end hats emission, the output coupling circuit, the copper surface losses and the rate of rise of anode voltage, but none proved to be relevant. However, the investigations revealed some important features of magnetron operation.

Computer modelling revealed for the first time non-uniform electron emission and back bombardment along the length of the cathode. Also it was shown that in computer modelling it is essential to use a real rather than a uniform magnetic field profile. Simulation runs with different cathode emission profiles have indicated marked influence of the emission distribution on the overall efficiency of the magnetron.

Computer modelling also indicated that high energy back bombardment electrons are present in the X band magnetron and that an artificially high initial velocity of emitted electrons significantly reduces the overall efficiency. It is therefore concluded that the high energy of secondary electrons is the likely reason for a relatively low efficiency of

the X band magnetron.

Perhaps one ought to add that all the new and additional information could not have been obtained without a powerful 3D computer code.

Acknowledgments

I would like to express my gratitude to my supervisor, Dr. X. Chen, for his supervision, guidance and support throughout this project.

Many thanks are also due to the following people who have kindly offered their help and support:

- Mr. M. Esterson specifically, who guided me through my four year's PhD study. His knowledge of magnetrons and intelligent way of analyzing has been great help.

- Professor P. A. Lindsay for his inspiring suggestions, from the view of fundamental magnetron theory.

- Dr. L. Ludeking for his support on MAGIC simulation techniques.

- Mr. P. Burleigh, Mr. M. Brady, Mr. K. Saleem and Mr. D. Wilson for their suggestions regarding engineering problems and many useful discussions.

- Dr. Z. Wang for his help on computer modelling.

- All my colleagues at the Electronic Engineering Department, Queen Mary College, for their assistance.

Finally I would like to convey my gratitude to my husband and my parents, for their understanding, encouragement and everlasting support.

Table of Contents

List of Figures

List of Tables

List of Abbreviations

ABCS	Absorbing Boundary Conditions
CFA	Cross-Field Amplifier
CW	Continuous Wave
FDTD	Finite Difference Time Domain
FFT	Fast Fourier Transform
HPM	High Power Microwave
PIC	Particle-In-Cell
RF	Radio Frequency
RRV	Rate of Rise of Voltage
TWT	Travelling Wave Tube

Chapter 1

Introduction

1.1 Introduction to Microwave Tubes

The magnetron was the first truly practical microwave device. It was developed in England in the 1930's and it provided the impetus for the development of microwave radar during World War II. Since then, many microwave devices have been developed for the generation and amplification of microwave radiation. Although in recent years solid-state devices have been occupying many areas that were once reserved for microwave tubes, microwave electron tubes have certain unique properties that are unlikely to be surpassed by solid-state devices, especially in the domain of high power (10KW $\sim$ 10MW) and high frequency (1GHz and higher) applications [1, 2]. In this chapter general operation mechanisms and various applications of microwave electron tubes will be described.

1.1.1 Fundamentals of microwave tubes

There are various types of microwave tubes, but they all share some features and fundamental operating mechanisms. A typical electron tube consists of two or more electrodes enclosed in a glass or metal-ceramic envelope that is evacuated. A cathode is used to

emit electrons either by thermionic emission or electric field emission, or some other methods, such as secondary emission. Fundamental to all electron tubes are the dynamics of charged particles under different electric- and magnetic-field configurations. The principle of operation is to affect the kinetic or potential energy of electrons so as to generate electromagnetic radiation; for example when an electron is decelerated, it loses its kinetic energy to the RF field. Thus, the DC energy stored in an external power supply can be converted to microwave energy in the load circuit. Another feature is that there must be a way for the RF energy to be coupled out of the tube. This is always accomplished with the help of transparent windows, capacitive or inductive coupling probes or loops. There are several important parameters characterising microwave tubes such as power output, frequency, bandwidth, tuning range, efficiency and noise.

1.1.2 Different microwave tubes and their applications

Depending on the different interaction mechanism between the electron beam and the electro-magnetic field, microwave tubes can be grouped into two categories: the 'O' type and the 'M' type. The 'O' type is also called a linear-beam type. A simple schematic is shown in Figure 1.1. In this type of tube, the electron beam traverses the length of the tube and is parallel to the magnetic field, which is used for focusing only.

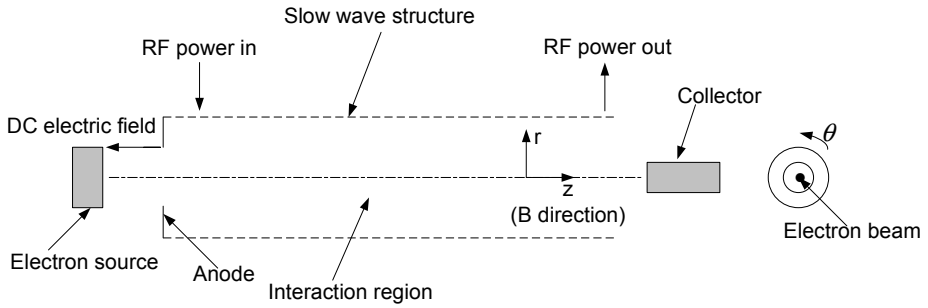

Figure 1.1: The beam-wave interaction is 2D in 'O' type devices.

The 'M' type are also called crossed field devices. A simple schematic is shown in Figure 1.2. In this type of tube, magnetic field is perpendicular to both the electron beam and the accelerating electric field and plays a direct role in the interaction process.

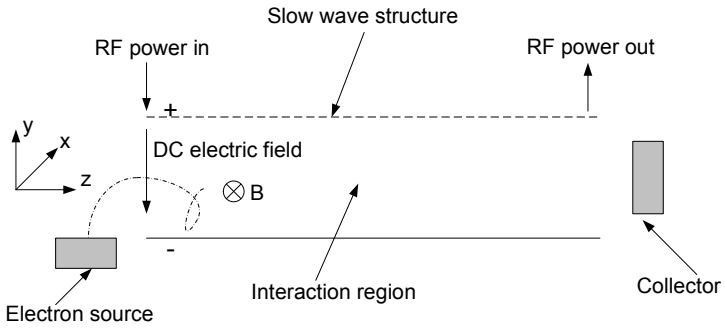

Figure 1.2: The beam-wave interaction is 3D in 'M' type device.

Apart from the above two categories, there are microwave tubes that belong to neither, such as the vircator, also called a 'space charge' type device. Most microwave tubes can be designed to operate either as oscillators or amplifiers.

The traveling wave tube is a typical 'O' type microwave device. The traveling wave tube (TWT), used as an amplifier, consists of an electron gun, a static magnetic field parallel to the axis of the structure which focuses the electron beam, a slow-wave structure and a beam collector. Figure 1.3 is an example of a TWT in which the slow wave structure is a helix.

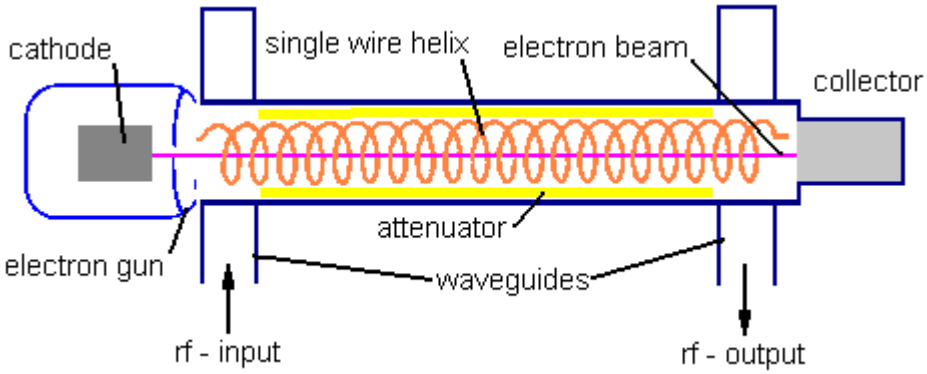

Figure 1.3: A diagram of a travelling wave tube [3]

The RF input is coupled to the slow wave structure at the electron gun end. The slow-wave structure slows down RF wave so that it travels at nearly the same speed as the electron beam, which makes the beam-wave interaction possible. During this process, some of the energy of the electron beam is transferred to the RF field and amplifies it. The amplified RF signal is coupled out at the end of the slow wave structure. The

remaining energy of the electron beam is dissipated in the collector. To prevent the tube self-oscillating an attenuator is added along the slow wave structure. A traveling wave tube is a broadband device because there exist no inherent resonances in the structure. Traveling-wave tubes are generally used to amplify microwave signals over broad bandwidths up to 0.8GHz. The efficiency of TWT is relatively low, typically about 20% [4]. For the above reasons an important application of TWTs is in satellite communication.

Microwave magnetron is an M-type device and an oscillator. It consists of a cylindrical cathode and a coaxial anode, which contains several individual resonant cavities. The most efficient oscillation mode is the π mode, when the adjacent cavities are 180° out of phase. A static magnetic field is parallel to the axis of the cathode.

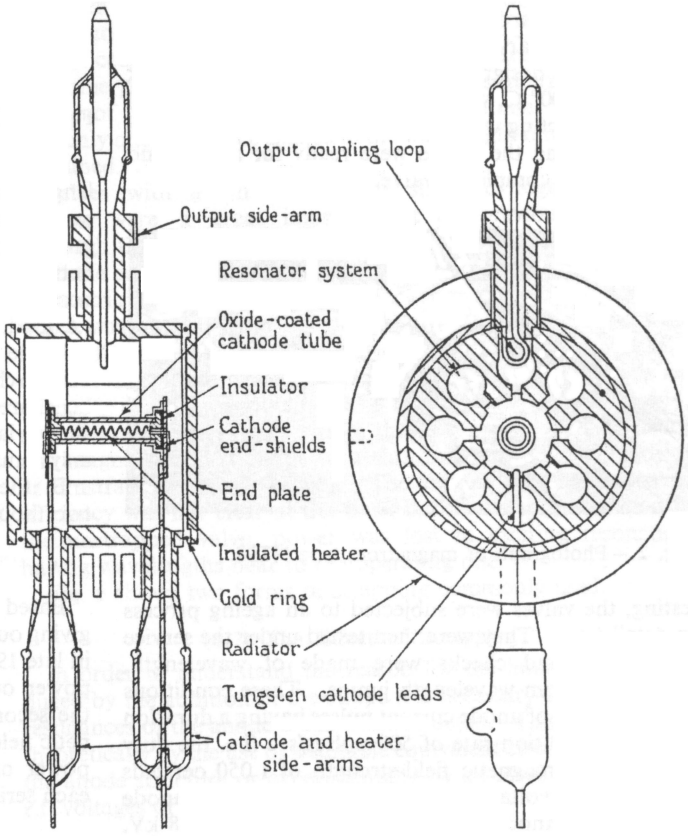

Figure 1.4: An eight cavity magnetron (type NT98) [5]

Figure 1.4 shows the drawing of the first cavity magnetron designed by Randall and Boot [5], which is an eight cavity, non-strapped magnetron. What differentiates cross-

field tubes from linear beam tubes is that magnetic field participates in the beam-wave interaction. During the start-up of oscillations the electron cloud rotates around the cathode surface and generates noise. When the RF field grows and the anode voltage exceeds a certain value, electrons begin to transfer their energy to the RF field. When the anode voltage and the static magnetic field are properly selected, the π mode oscillations will dominate.

The magnetron has the advantage of being able to generate high power (from several kilowatts to megawatts) at high efficiency (40 to 70%) [4]. Magnetrons are widely used in radar systems, medical X-ray sources and microwave ovens. Other cross-field tubes include cross-field amplifiers (CFAs) [4], amplitrons [6], gyrotrons [7], etc. A detailed mechanism of operation and typical characteristics of magnetrons will be discussed in chapter 2.

1.2 Motivation and Contributions

1.2.1 Characteristics of magnetron modelling

Compared with other microwave tubes, magnetrons are more difficult to model. Firstly, magnetrons require 3D rather than 2D modelling. In 'O' type devices, the magnetic field is parallel to the axis of the tube, see Figure 1.1. If the electron trajectories are symmetrical about the axis, only two dimensions are required for modelling, namely z and r.

In 'M' type devices, the DC electric field and the magnetic field are perpendicular to each other, see Figure 1.2. The DC electric field, together with the magnetic field control the electron trajectory in the y-z plane. Because the electron beam must be constrained in the direction perpendicular to the surface of the paper, i.e. x direction, three dimensions are necessary for adequate modelling of the interaction process, namely x, y, z.

Secondly, for example magnetrons always have complicated anode and cathode end structures which cannot be represented in 2D, such as anode strapping, which is required for adequate mode separation and end hats, used for constraining electron flow at the two ends of the cathode.

Lastly, the axially non-uniform magnetic field distribution invariably present in real tubes also requires 3D modelling.

Hence, 2D simulation is not sufficient for a proper study of the interaction process in most magnetrons. However, all the early magnetron modelling was in 2D and therefore it could not simulate magnetron operation realistically. With the development of more powerful computer codes, it is now possible to take into account all the effects mentioned above [8–10].

1.2.2 Challenging problems

The work presented in this thesis is solely based on 3D simulation using a powerful FD-TD (Finite-Difference, Time-Domain) and PIC (Particle-In-Cell) code called MAGIC [11]. A number of challenging problems of magnetron operation such as multipactor effect, moding and power dissipation inside the magnetron, which could not be modelled in 2D, can now be investigated by 3D computer modelling. In addition to the above problems, in this thesis an effort has been made to investigate various factors that affect the operating efficiency of a magnetron. Another novel contribution is the modelling of electron emission energy and back bombardment energy distribution along the length of the cathode.

I. Multipactor effect

Multipactor is a vacuum resonance discharge, which can be destructive. To our knowledge, the effect has not been investigated in magnetron modelling before. The electromagnetic conditions for multipactor to take place are very critical and thus difficult

to simulate. In chapter 4, preliminary modelling work has been done on the multipactor effect in the output system of an S band magnetron.

II. Moding problem

Moding is the competition between various resonant frequencies in the magnetron. When moding occurs, it spoils the operation of a magnetron. One of the tasks is an investigation of mode competition during the start-up of oscillation.

III. Various factors affecting the magnetron efficiency

Various factors that may affect the magnetron operating efficiency, such as the end hats emission, the output coupling circuit, the RRV (Rate of Rise of Voltage), the surface copper loss, the initial velocity of cathode emission, etc, have been investigated. Some of these effects, such as the end hats and cathode emission, are very difficult to study using theoretical or experimental methods. In practice such investigations become possible only by using 3D computer modelling.

IV. Emission and back bombardment distribution

An important contribution reported in this thesis is that for the first time the non-uniform distribution of cathode emission using a space-charge-limited emission model has been demonstrated. The important back bombardment distribution has also been investigated.

1.2.3 Contribution to industrial design

The usual trial and error process in the development of magnetrons is time consuming and expensive. Through computer modelling, this process can be shortened and made more cost efficient. Also, computer modelling can be used to obtain some important information on magnetron operation such as the starting-up characteristics and power dissipation on the anode and cathode due to electron bombardment. Some of these aspects, such

as the axial distribution of electron energy in cathode bombardment are very difficult to investigate experimentally. Thus our computer simulation may contribute directly to the design of new magnetrons. It is expected that from the manufacturer's point of view this would substantially reduce the time and cost of development of new devices.

1.3 Organization of the Thesis

Chapter 2 gives an introduction to the development and the operation mechanism of magnetrons. Detailed discussion has been presented on the beam-wave interaction, various operation modes and the required relationship between the anode voltage and the magnetic field. Finally the theory of anode voltage-magnetic field relation has been applied to S/X band magnetrons investigated in this project.

Chapter 3 describes the FDTD (Finite Difference Time Domain) and PIC (Particle In Cell) computer simulation techniques. This covers the FDTD algorithm, its numerical stability, uncertainty and absorbing boundary conditions (ABCs). The PIC technique has been discussed with emphasis on several issues such as the basic processing cycle, leap-frog integration that forwards the particles and the weighting of the particles on discrete grids.

Chapter 4 presents the investigation of an S band magnetron (e2v MG5193). In particular the RF power transmission in the output circuit has been studied. Also a preliminary study of the multipactor effect has been discussed.

Chapter 5 presents an extensive simulation work on an X band magnetron (e2v MG5241). Different meshing schemes have been tested and an optimized computer model has been developed. In cold test modelling the resonance spectrum and the corresponding Qs have been obtained. In hot test simulations different cathode emission models have been compared and various factors that may affect the magnetron efficiency have been investigated.

Chapter 6 investigates the non-uniform emission and back bombardment of the cathode in MG5241 magnetrons, including the effect of uniform and non-uniform magnetic field distribution.

Chapter7 investigates the energy distribution of cathode back bombardment, again in MG5241 magnetrons. It is found that high energy secondary emission electrons are present in large numbers. An additional investigation of initial electron velocities has shown that in all cases high energy secondary emission significantly affects the efficiency of the magnetron.

Chapter 8 contains final conclusions and suggestions for future work.

References

[1] D.M.Pozar, Ed., *Microwave engineering.* Addison-Wesley, 1990.

[2] R.S.Symons, "Modern microwave power devices," *IEEE AESS Systems Magazine*, pp. 19–26, January 2002.

[3] http://www.tpub.com/neets/book11/45d.htm, Ed., *Electrical Engineering training series.* Integrated publising, 2004.

[4] S.Y.Liao, Ed., *Microwave devices and circuits.* Prentice Hall Internationsl, 1990.

[5] W.E.Willshaw, L.Rushforth, A.G.Stainsby, R.Latham, A.W.Balls, and A.H.King, "The high power pulsed magnetron development and design for radar application," *The Journal of the Institution of Electrical Engineers, Proceedings at the Radiolocation Covention*, pp. 985–1005, March-May 1946.

[6] L.Ludeking, R.Smith, and R.Wortman, "An examination of the performance of backward wave CFA's in simulation and experiment," in *Pulsed Power Plasma Science*, ser. Digest of Technical Papers, vol. 1, no. 17-22, June 2001, pp. 229–231.

[7] V.A.Flyagin and G.S.Nusinovich, "Gyrotron oscillators," *Proceedings of the IEEE*, vol. 76, no. 6, pp. 644–656, June 1988.

[8] X.Chen, M.Esterson, and P.A.Lindsay, "3D simulation of microwave magnetrons,"

Digest, IEE Colloquium on High Frequency Simulation II, pp. 1–4, Nov 1997.

[9] X.Chen, P.A.Lindsay, and M.Esterson, "3D modelling of high power, explosive emission magnetrons," in *Displays and vaccum electronics*, ser. ITG-Fachbericht 150/IEEE, Berlin, 1998, pp. 453–458.

[10] Z.Wang, X.Chen, and M.Esterson, "Characterisation of resonance modes of a magnetron cavity using MAGIC- a FD-TD code," *Effective Microwave CAD Tools, IEE Coloquium*, pp. 1–4, 1999.

[11] L.Ludeking, Ed., *Manual of MAGIC Tool Suite*. Mission Research Corporation, 2002.

Chapter 2

Operating Principle of Magnetrons

Introduction

In this chapter, the various types of magnetrons will be introduced. The operating mechanism of these magnetrons, especially the modern resonant cavity magnetron will be discussed. Theoretical analysis will be applied to the two magnetrons in S/X bands, which were studied in the later modelling work.

2.1 Early Magnetrons

Magnetron is a kind of cross-field device, in which crossed electric and magnetic fields are used. The first magnetron was mentioned by Hull in 1921, who used a cylindrical anode with coaxial filament (see Figure 2.1(a)). In 1929 Okabe developed the spilt anode magnetron, in which the anode was divided into two halves (see Figure 2.1(b)). Later on other workers further developed the split anode magnetron by dividing the anode into more segments (see Figure 2.1(c)). In all these magnetrons, the anode segments

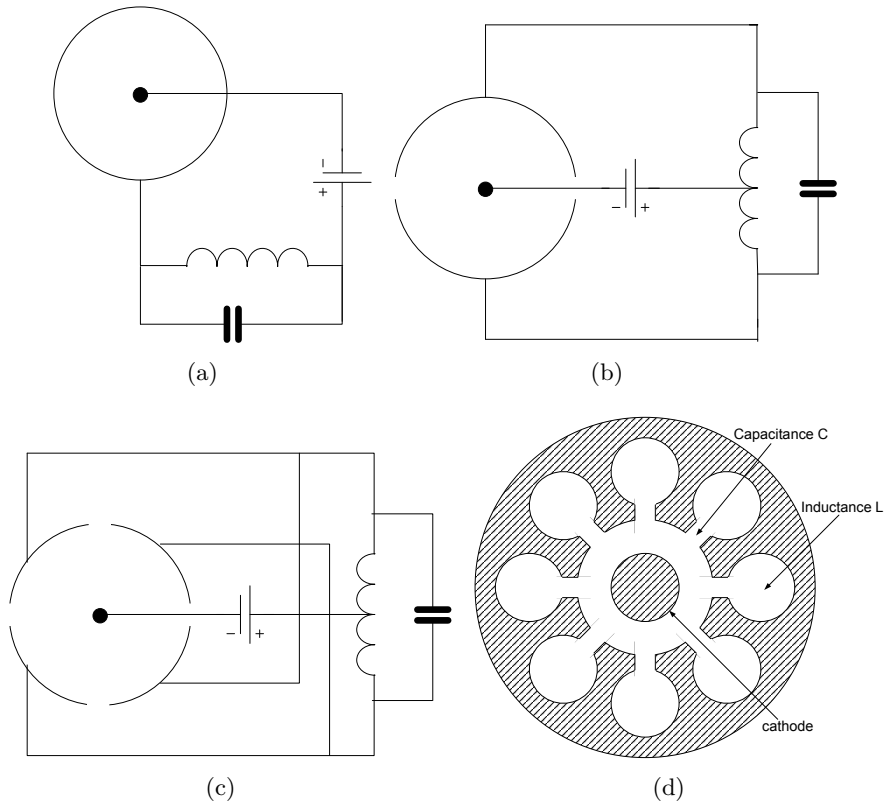

Figure 2.1: Early magnetrons (a) Cylindrical anode magnetron, (b)Split anode magnetron (c) Multi-segment magnetron (d) Resonant cavity magnetron

are connected to outer oscillation circuits. In 1940, Randall and Boot introduced the first modern resonant cavity magnetron [1], in which the resonant cavities replaced the resonant circuits connected to the anode segments (see Figure 2.1(d)). The power output of this type of magnetron was dramatically increased compared with the previous types. It is with this type of magnetron that the development of modern radar became possible. All these magnetrons rely on two types of operation mechanisms, the negative resistance oscillation and the electron transit time oscillation.

2.2 Negative Resistance Magnetron

The split-anode negative resistance magnetron is operated with its two halves of the anode at different RF potentials. The equipotentials in a negative resistance magnetron

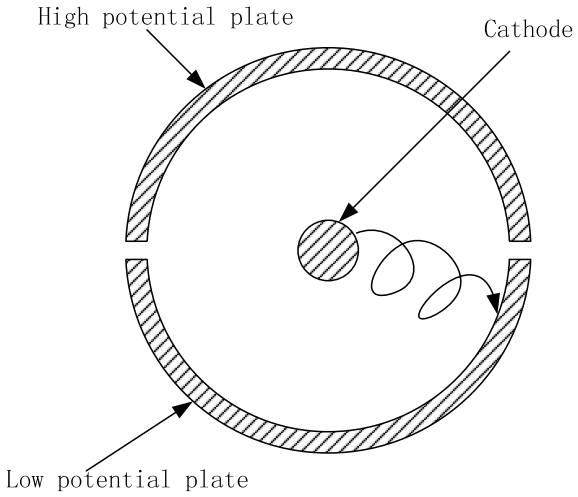

Figure 2.2: Electron trajectory in a split anode negative resistance magnetron

tend to point towards the anode segment with lower potential. Under the combined influence of the electric and magnetic fields, the electron leaving the cathode follows a cycloid path, with its rolling center along the equal potentials and finally strikes the lower potential anode segment, see Figure 2.2. In practice, only few electrons reach the higher potential segment of anode; most of the electrons strike the lower potential segment of the anode, resulting in more current flow in the lower potential segment. This explains the effect of the negative resistance oscillation. The limit of this type of magnetron is that the RF oscillation period must be considerably greater than the electron transit time. The reason is that throughout the time of the electron journey from the cathode to the anode, the potentials of the two anode segments must keep polarity unchanged. When the operating frequency is increased, the efficiency drops. This type of magnetron is capable of operating at wavelength down to 100cm and gives output in the order of 100watts with an efficiency of 25% [1].

2.3 Principle of Transit Time Oscillation

The cylindrical anode magnetron, the multi-segment anode magnetron and the resonant cavity magnetron all depend on electron transit time oscillation, which makes higher

frequency oscillation possible. The beam-wave interaction inside a magnetron is very complicated. In this section a simplified planar diode and cylindrical diode will be discussed first to explain the basic kinetic motion of electron between the cathode and the anode under the influence of the crossed electric and magnetic fields. On this basis the operation of resonant cavity magnetron will then be discussed in section 2.4.

2.3.1 Kinetic motion of electrons in a planar diode

Figure 2.3 demonstrates a planar diode, which consists of two infinite large plane electrodes with potential difference of V_a. The distance between the two electrodes is d_0. Thus the electric field between the cathode and anode is $\vec{E} = V_a/d_0$. A uniform magnetic field is applied perpendicular to the electric field and parallel to the two electrodes.

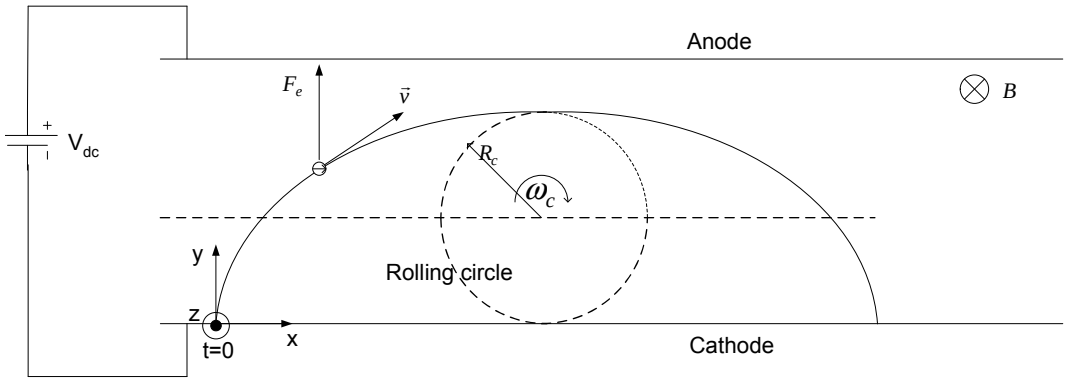

Figure 2.3: Electron trajectory in a planar crossed field diode

An electron emitted from the cathode moves under the influence of electric force $\vec{F}_e = e\vec{E}$ and magnetic force $\vec{F}_m = e\vec{v}\times\vec{B}$ between the anode and the cathode. In order to solve the trajectory of the electron, the kinetic motion equation is combined with the two force equations as below:

$$m\frac{d\vec{r}^2}{dt^2} = e(\vec{E} + \vec{v}\times\vec{B}) \tag{2.1}$$

$$\vec{F}_e = e\vec{E} \tag{2.2}$$

$$\vec{F}_m = e\vec{v}\times\vec{B} \tag{2.3}$$

In the Cartesian coordinate system, the electron velocity can be resolved into the horizontal component dx/dt and the vertical component dy/dt. Eqs 2.1 to 2.3 can then be rewritten as below:

$$e\vec{E} - e\vec{B}\frac{dx}{dt} = m\frac{d^2y}{dt^2} \tag{2.4}$$

$$e\vec{B}\frac{dy}{dt} = m\frac{d^2x}{dt^2} \tag{2.5}$$

The solution of the above equations, which neglect the space-charge effects, shows that the electron trajectory is a cycloid:

$$x = A_1\sin(\omega_c t + \phi) + A_2 t + x_0 \tag{2.6}$$

$$y = A_1\cos(\omega_c t + \phi) + y_0 \tag{2.7}$$

$$\frac{dx}{dt} = \omega_c A_1\cos(\omega_c t + \phi) + A_2 \tag{2.8}$$

$$\frac{dy}{dt} = -\omega_c A_1\sin(\omega_c t + \phi) \tag{2.9}$$

Where A_1, A_2, x_0, y_0 and $\omega_c = eB/m$ are all constants, which can be determined by the initial condition. If we let the electron start from the origin, the initial conditions can

be expressed as:

$x|_{t=0} = 0$; $y|_{t=0} = 0$; $dx/dt|_{t=0} = v_{x0}$; $dy/dt|_{t=0} = v_{y0}$.

Applying the initial condition to Eqs 2.6 to 2.9, the constants can be determined as shown:

$$A_2 = \frac{E}{B}$$

$$A_1 = \frac{1}{\omega_c}\sqrt{v_{y0}^2 + (A_2 - v_{x0}^2)}$$

$$x_0 = \frac{v_{y0}}{\omega_c}$$

$$y_0 = \frac{(A_2 - v_{x0})}{\omega_c}$$

$$\sin\phi = -\frac{x_0}{A_1}$$

$$\cos\phi = -\frac{y_0}{A_1}$$

For the convenience of calculations, constant ϕ is not given in an explicit form. Rearranging the solutions Eqs 2.6 to Eq 2.9, the following equations can be obtained:

$$x = -y_0 \sin(\omega_c t) - x_0 \cos(\omega_c t) + A_2 t + x_0 \tag{2.10}$$

$$y = -y_0 \cos(\omega_c t) + x_0 \sin(\omega_c t) + y_0 \tag{2.11}$$

$$\frac{dx}{dt} = -\omega_c y_0 \cos(\omega_c t) + \omega_c x_0 \sin(\omega_c t) + A_2 \tag{2.12}$$

$$\frac{dy}{dt} = \omega_c y_0 \sin(\omega_c t) + \omega_c x_0 \cos(\omega_c t) \tag{2.13}$$

Considering a simple condition that the electron starts with zero velocity ($v_x = 0$, $v_y = 0$) from the cathode, it can be seen in Figure 2.3 that the electron travels like a point on a circle rolling along the cathode surface, its angular frequency is $\omega_c = eB/m$. Within one period $T = 2\pi/\omega_c$, the electron will complete a revolution and go back to the cathode. Since the magnetic field does not contribute to the electron energy change, the maximum velocity occurs at the top of the cycloid orbit as shown in Figure 2.3, where $v_y = 0$, $y = y_{max}$.

The radius of the rolling circle is determined by $R_c = y_{max}/2$. Since $y_{max} = y(T/2)$, substituting the initial conditions into Eq 2.11, the radius of the rolling circle can be obtained as

$$R_c = \frac{mE}{eB^2} \tag{2.14}$$

From Eq 2.14 the maximum distance an electron travels in x direction within one cyclotron period T is

$$x_{max} = x(T) = 2\pi R_c = \frac{2\pi mE}{eB^2} \tag{2.15}$$

For a given electric field, the radius of the electron orbit will vary with the magnetic field. For a cutoff condition, when an electron trajectory just grazes the anode, that is $y_{max} = d_0$, the magnetic field is B_c. Solving the Eq 2.14 and substituting for E the value V_a/d_0, the cutoff magnetic field is given by

$$B = B_c = \sqrt{\frac{2mE}{ed_0}} = \frac{1}{d_0}\sqrt{\frac{2m}{e}V_a} \tag{2.16}$$

The trajectories of electrons for different magnetic fields are shown in Figure 2.4. Curve '1' stands for electron orbit when the magnetic field is zero; if magnetic field is smaller than B_c, the electron will strike the anode, curve '2'; otherwise, the electron will miss the anode and continue its cycloid orbit, curve '4'; curve '3' represents the cut off condition when $B = B_c$, the electron just grazing the anode. In Figure 2.4, the elecrton is assumed to have zero initial velocity, $v_{x0} = v_{y0} = 0$.

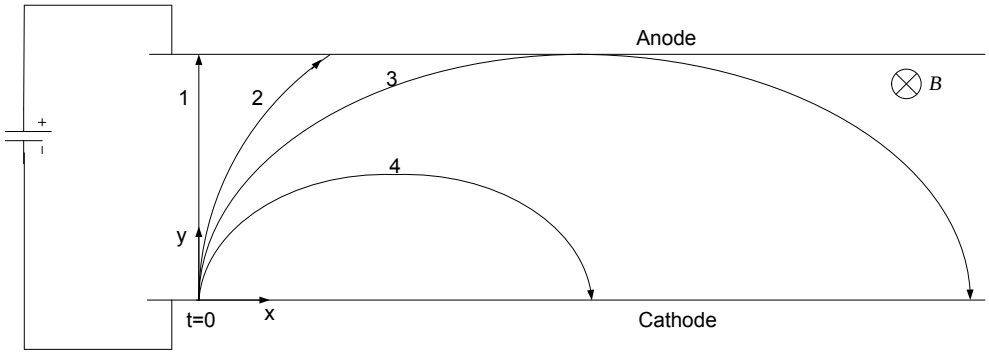

Figure 2.4: Electron trajectories in a planar crossed field diode for different magnetic fields

When the intial velocity of the electron is non-zero, the elecron trajectory will be quite different. Figure 2.5 demonstrates the electron trajectories with different initial velocity components, v_{x0} and v_{y0}. The magnetic field is 0.41T, the DC voltage is 5.7kV, the distance between cathode and anode is 0.92mm, which are the operating parameters and dimension used for the X band magnetron, which has been investiagted in Chapter 5. In this diagram, the electrons leave the cathode surface with zero velocity (curve 1), velocity normal to the cathode surface (curve 3) and velocity at 45 degrees to the normal (curve 2) respectively.

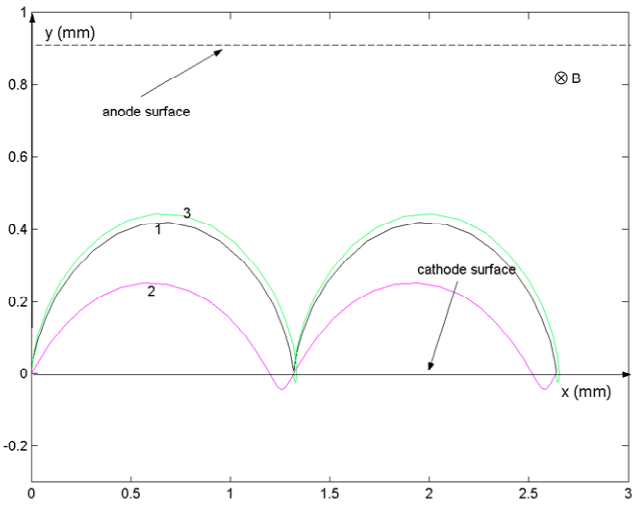

Figure 2.5: Electron trajectories with different intial velocities and directions. Electron trajectory 1: the initial velocity is zero; Electron trajectory 2: $v_x|_{t=0} = v_y|_{t=0} = E/(2B)$; Electron trajectory 3: $v_x|_{t=0} = 0$, $v_y|_{t=0} = E/(2B)$; where $E = V_{dc}/d$, $V_{dc} = 5.7kV$, $d = 0.92mm$.

Now consider an AC field applied between the cathode and the anode. The magnetic field is bigger than the cut off magnetic field B_c, thus the electron will not strike the anode directly. Electrons emitted at various positions of the RF period of the AC field will be either accelerated or decelerated. Figure 2.6 demonstrates the trajectories of the two kinds of electrons.

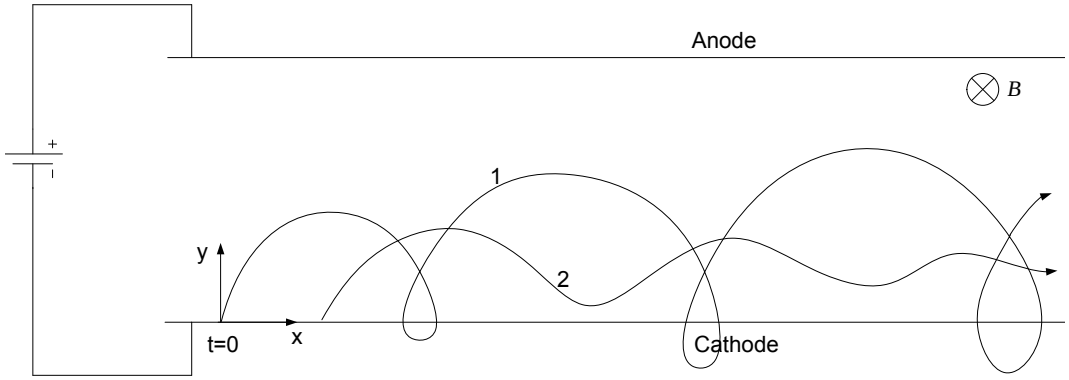

Figure 2.6: Electron trajectories in the presence of AC field

When an electron is accelerated by the AC field, the rolling circle of its cycloid path will increase; it will be deflected by the magnetic field more sharply and strike back to the cathode quickly as demonstrated by curve '1'. When an electron is decelerated by the AC field, it will experience weakened magnetic force, thus its rolling circle will be reduced in size. This electron will finally move horizontally with drifting velocity E/B as demonstrated by curve '2'. In the first case, the electron absorbs energy not only from the DC field but also from the AC field. Since this kind of electrons will strike back the cathode quickly, they will not affect the AC field much. In the latter case, the electron will give up some of its energy absorbed from the DC field to the AC field. Thus the AC field will experience a net gain of energy. This energy is obtained from the DC field through the electrons.

2.3.2 Kinetic motion of electrons in a cylindrical diode

All the real magnetrons consist of coaxial cylindrical electrodes. Based on the above planar diode, a cylindrical diode will be discussed here. Figure 2.7 is the geometry of a cylindrical diode, with cathode radius r_c and anode radius r_a. The magnetic field is parallel to the axis of the diode and perpendicular to the electric field.

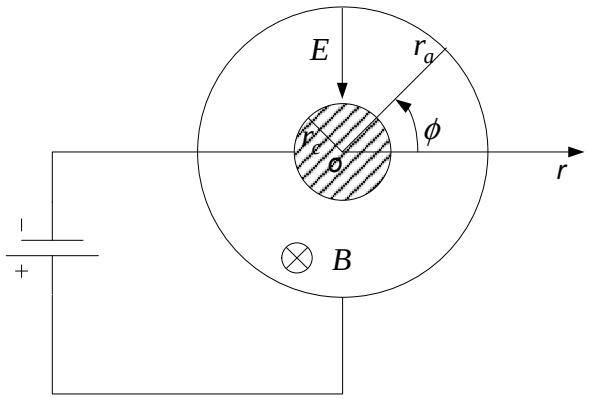

Figure 2.7: Geometry of a cylindrical diode [1]

Using the same analysis as in section 2.3.1, the kinetic equations of the electron in cylindrical coordinates are given by

$$eE - eBr\frac{d\phi}{dt} = m[\frac{d^2r}{dt^2} - r(\frac{d\phi}{dt})^2] \tag{2.17}$$

$$eB\frac{dr}{dt} = m\frac{1}{r}\frac{d}{dt}(r^2\frac{d\phi}{dt}) \tag{2.18}$$

Rearranging Eq 2.18 results in the following equation

$$d(r^2\frac{d\phi}{dt}) = \frac{eB}{m}rdr \tag{2.19}$$

Considering that the electron leaves the cathode with zero initial velocity, $d\phi/dt|_{r=r_c} = 0$, integration of Eq 2.19 yields

$$\frac{d\phi}{dt} = \frac{\omega_c}{2}(1 - \frac{r_c^2}{r^2}) \tag{2.20}$$

where $\omega_c = eB/m$ is the electron cyclotron frequency. The angular velocity of the electron is then obtained.

$$\omega_0 = \frac{\omega_c}{2}(1 - \frac{r_c^2}{r^2}) \tag{2.21}$$

In the cut-off condition, when the electron can just graze the anode, its radial velocity is zero, $dr/dt|_{r=r_a} = 0$. Since we assume the electron leaves the cathode with zero initial velocity, according to the energy conservation, when the electron reaches the anode, its kinetic energy can be written as

$$\frac{1}{2}mv_t^2 = eV_a \tag{2.22}$$

where the angular velocity is

$$v_t = r_a\frac{d\phi}{dt} \tag{2.23}$$

Substituting Eqs 2.20 and 2.22 in Eq 2.21, the cut off condition between the magnetic field and DC voltage can be obtained

$$B = B_c = \frac{\sqrt{8mV_a/e}}{r_a(1 - r_c^2/r_a^2)} \tag{2.24}$$

or

$$V_a = \frac{e}{8m}r_a^2(1 - \frac{r_c^2}{r_a^2})^2B_c^2 \tag{2.25}$$

where V_a is the DC voltage between anode and cathode. For a given V_a, when $B < B_c$ the electron will strike the anode; otherwise it will miss the anode. If we keep the magnetic field constant, the electron orbit will strike the anode when $V_a > (V_a)_c$; otherwise, it will miss the anode. Figure 2.8 shows the different electron orbits in a cylindrical crossed field diode (smooth anode magnetron).

When an RF field is present, the interaction between the electron and the RF filed under the influence of the DC voltage and the magnetic field is similar to that of the planar diode. Electrons will be either accelerated or decelerated by the RF field. When the DC voltage and the magnetic field are properly selected, the energy will be transferred

from the DC field to the RF field via the electrons.

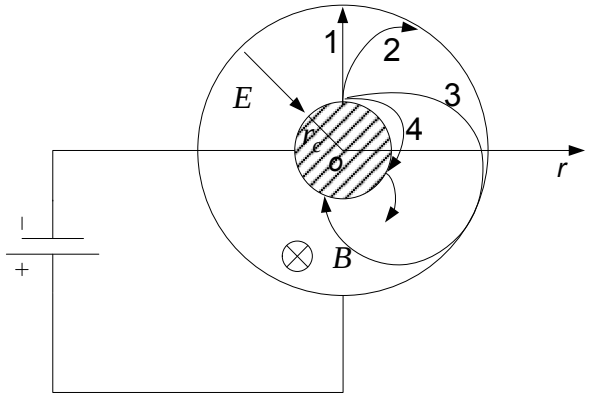

Figure 2.8: Electron trajectories in a cylindrical diode for different magnetic fields. 1. $B = 0$; 2. $B < B_c$; 3. $B = B_c$; 4. $B > B_c$.

2.4 Resonant Cavity Magnetron Operation

The operational mechanism of an eight-cavity, hole and slot magnetron is discussed here. The anode block of this kind of magnetron is composed of eight coupled resonators surrounding the cathode. Figure 2.9 shows the cross section of the magnetron anode. In the axial direction the resonant cavities open into end spaces . The inner surface of the anode block consists of alternate vanes and gaps. RF fields excite inside the magnetron can be assumed to consist of two waves, travelling in opposite directions. Electrons are emitted from the cathode. Through the interaction between the electron cloud and the electro-magnetic field, DC input power is converted to RF output power.

The resonant system is the most important part for the magnetron design. It determines the frequency and configuration of the RF field and the interaction between the electron cloud and the RF field, leading to an efficient energy conversion. A good resonant system should have the characteristics of making the magnetron work in a stable manner. This includes stability against small frequency changes and frequency jumps between different operation modes. This aspect of beam-wave interaction will be discussed in more detail presently.

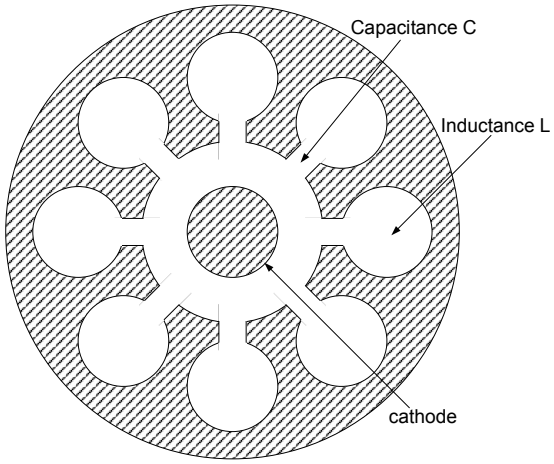

Figure 2.9: The cross section of an eight cavity hole and slot magnetron. The hole and slot structures provide inductance and capacitance for individual resonators.

2.4.1 Equivalent circuit and oscillation modes

Here the circuit theory is used to explain the range of possible RF oscillations. In a resonant cavity magnetron individual cavities replace resonant circuits. Usually the individual cavities are operating at their lowest oscillation mode. An equivalent oscillating circuit is shown in Figure 2.10. Complicated electro-magnetic coupling exists between the individual cavities. 'L' and 'C' are inductance and capacitance representing a single cavity. 'C'' is the capacitance between the individual anode segment and the cathode. The lines of magnetic flux in one individual cavity couple to another cavity in the end spaces; this kind of magnetic coupling is represented by 'M' in the equivalent circuit of Figure 2.10 [2].

The oscillation frequency of an individual resonator is $\omega_0 = 1/\sqrt{LC}$. Because the eight cavities are symmetrically distributed, the phase differences between adjacent cavities are the same, say ϕ. In each cavity, the oscillating voltage between the anode vanes can be described by,

$$V_1 = V_m \sin(\omega_0 t) \tag{2.26}$$

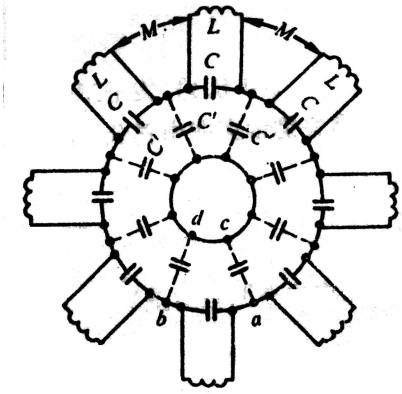

Figure 2.10: Equivalent circuit of an eight-cavity magnetron [2]

$$V_2 = V_m \sin(\omega_0 t - \phi) \tag{2.27}$$

$$V_3 = V_m \sin(\omega_0 t - 2\phi) \tag{2.28}$$

.....

$$V_8 = V_m \sin(\omega_0 t - 7\phi) \tag{2.29}$$

$$V_9 = V_m \sin(\omega_0 t - 8\phi) \tag{2.30}$$

where V_m is the amplitude of the RF voltage.

Since magnetron is a closed circuit, V_9 should be equal to V_1 when the system is oscillating. This leads to $8\phi = 2\pi n$ (n=0, 1, 2...). In general, the number of resonator cavities is N, the phase condition for oscillations to exist is given by

$$N\phi = 2\pi n \tag{2.31}$$

thus,

$$\phi = \frac{2\pi n}{N} \tag{2.32}$$

where n is an integer from zero to N-1. From Eq 2.32, it is obvious that there are several different modes that can satisfy the same phase condition for the oscillations to exist. Modes $n = N/2 + m$ and $n = N/2 - m$ $(m = 1, \cdots N/2)$ are pairs of degenerate modes. These modes are also called 'doublets'. If the magnetron is a perfect symmetrical structure, the two components of a doublet would have the same wavelength. Thus the total possible modes in a N cavity system are from n=1 to n=N/2. When n=N/2, $\phi = \pi$, its corresponding doublet is the n=0 mode; this means zero charge distribution on the anode segments, and the mode does not exist. Thus, the π mode is a non-degenerate mode, or a stationary wave mode. All the other modes are traveling waves or having a traveling wave component superimposed on a standing wave. In reality exact symmetry is not attainable. Also there is asymmetry caused by the output-coupling loop. Thus the two components of a doublet have slightly different wavelengths.

For an eight-cavity magnetron, the possible modes are n=1, 2, 3, 4, 'n=4' corresponding to the π mode. The charge and electric field distribution of the four possible modes are illustrated in Figure 2.11.

If ω is the resonant frequency of mode n, the time needed for traveling wave to travel around the anode for one round would be 'nT', where $T = 2\pi/\omega$; therefore its rotating frequency would be

$$\Omega = \frac{2\pi}{nT} = \frac{\omega}{n} \tag{2.33}$$

So the rotating velocity around the anode is slowed down by a factor 'n'. It is this that makes it possible for the electron to rotate in synchronism with the RF field, which enables the energy transfer to the RF field.

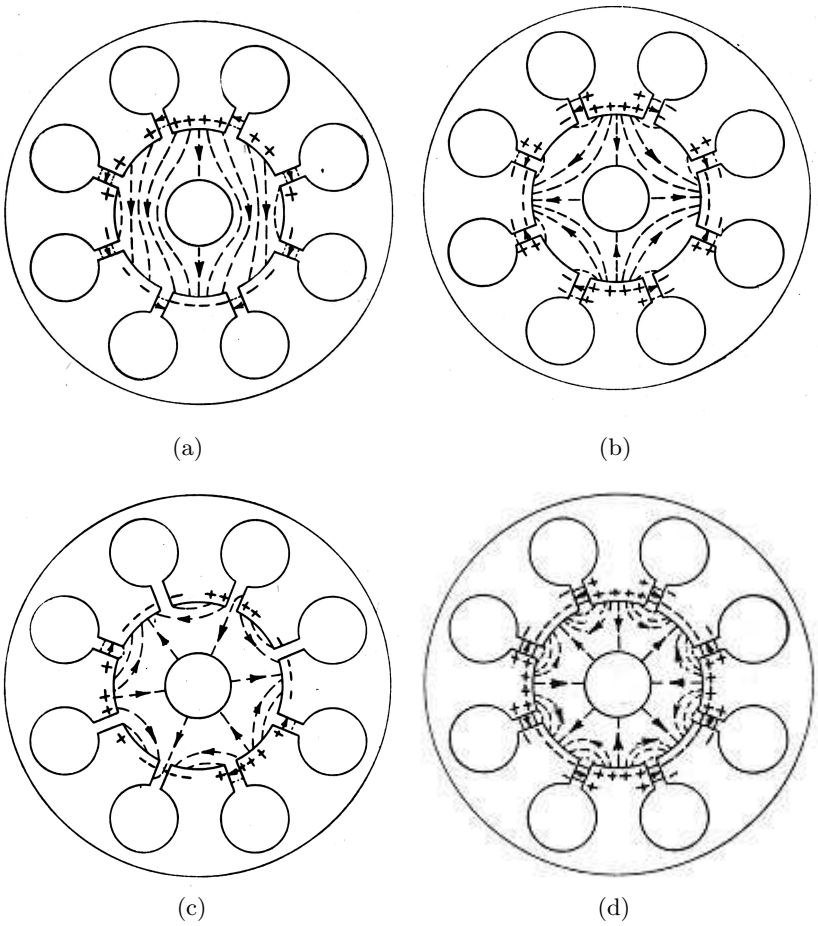

Figure 2.11: Field and charge distribution of different modes in an eight-cavity magnetron (a)n=1 (b)n=2 (c)n=3 (d)n=4

2.4.2 The Hartree/Hull conditions

For a magnetron to operate properly, special conditions between the applied anode voltage and the static magnetic field must be satisfied. In this section, the two equations regarding these conditions will be introduced and applied to the two magnetrons (S/X band), which are the subject of the simulation work in the later chapters.

It is discussed in Section 2.3.2 that in the cylindrical diode magnetron, for an electron to touch the anode, the cutoff condition is

$$V_0 = \frac{er_a^2}{8m}[1 - (\frac{r_c}{r_a})^2]^2 B_0^2 \tag{2.34}$$

Where

V_0	Cutoff anode voltage;
r_a	Radius of anode;
r_c	Radius of cathode;
B_0	Cutoff static magnetic field.

In the absence of RF field, with a given magnetic field, when the anode voltage is smaller than V_0 , the electron will not reach the anode. This voltage V_0 is called the cutoff voltage, or Hull voltage.

When a magnetron is operating below the cutoff voltage, the electron cloud will be formed between the cathode and the anode. For the magnetron to start oscillating, it is required that the electrons should rotate synchronously with the RF field at the anode surface, so that

$$\omega_e = \frac{\omega}{n} \tag{2.35}$$

where

ω_e	The angular frequency of electron;
ω	The angular frequency of RF field;
ω/n	The rotating frequency of the corresponding traveling wave;
n	The mode number of the traveling wave.

Applying this synchronous condition to the two equaions Eq 2.17 and Eq 2.18, which govern the electron movement in a cylindrical coordinate system, the threshold voltage for RF oscillation to start in a magnetron can be obtained.

$$V_t = \frac{r_a^2}{2}(1 - \frac{r_c^2}{r_a^2})\frac{\omega}{n}B - \frac{r_a^2}{2}\frac{m}{e}(\frac{\omega}{n})^2 \tag{2.36}$$

The threshold voltage is also known as the Hartree voltage after Hartree who developed the theory. Rigorous solutions of this problem can be found in [2, 3]. This voltage

is the condition at which oscillations should start provided at the same time that B is sufficiently large so that the undistorted space charge does not extend to the anode. Assuming a constant ratio of r_c/r_a, consider the effect of keeping B and ω fixed, V_t is proportional to r_a^2 , so that operating conditions remain unchanged if the operating voltage is increased proportional to the square of the anode radius.

Eq 2.34 combined with Eq 2.36 determine the operation zones of a magnetron, as shown in Figure 2.12, which describes the situation in an eight-cavity magnetron.

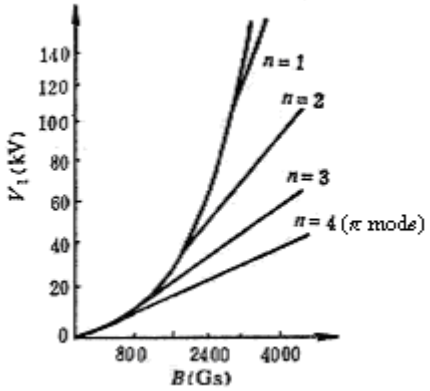

Figure 2.12: The Hartree diagram of an eight-cavity magnetron [2]

Eq 2.34 is a parabolic curve, above which, magnetron cannot operate. Eq 2.36 is a straight line that is tangent to the parabolic curve. In the Hartree diagram shown in Figure 2.12, π mode has the lowest Hartree voltage. Below this voltage, magnetron also cannot operate, because in this region, the DC field is too weak to move the electrons into synchronism with the slowest rotating RF field, i.e. the π mode. When the anode voltage is slightly above the Hartree voltage, the magnetron starts to oscillate. It has been observed that the region between the Hull voltage curve and the π mode Hartree voltage line is the usual magnetron operating zone. However, in practice, the anode voltage of a magnetron is always set below the $\pi - 1$ mode line (n=3 in Figure 2.12) to avoid mode competition.

2.4.3 The Hartree/ Hull conditions for the S/X band magnetrons

In this section, the theory discussed above has been applied to the simulation models of an S band hole and slot magnetron and an X band strapped magnetron. Since in practice the main competing mode is the $\pi - 1$ mode, other higher order modes have minor effects on π mode oscillations; only π and $\pi - 1$ modes have been calculated and plotted in the following Hartree/Hull graphs, see Figure 2.13.

The anode and cathode dimensions, the static magnetic fields applied, the oscillation frequencies of π and $\pi - 1$ modes, which are described in Chapters 4 and 5 separately and their corresponding Hartree/Hull voltages of the two magnetrons are presented in the table 2-A.

Table 2-A: Hartree/Hull condition for e2v MG5193 (S Band) and MG5241 (X Band) magnetrons

Magnetrons	S Band	X Band
B_0(T)	0.16	0.405
r_a(mm)	17	2.82
r_c(mm)	9.25	1.9
V_{Hull}(kV)	80.49	8.54
$V_{Hartree(\pi)}$(kV)	42.89	4.84
$V_{Hartree(\pi-1)}$(kV)	52.58	5.66
f_π(GHz)	2.99	9.50
$f_{\pi-1}$(GHz)	3.25	10.42

Magnetrons can only operate between the Hull parabola and the straight Hartree lines corresponding to different modes. The cutoff voltages and magnetic fields of different modes are the tangential points in the diagrams, marked by '*'. π mode has lower cutoff voltage and magnetic field than π-1 mode. With the same magnetic field the π mode oscillation requires a lower threshold voltage than π-1 mode. In real magnetron operation, the π-1 mode always competes with the π mode, potentially spoiling the magnetron's operation. Simulations in Chapters 4-5 will demonstrate that when the input voltages is above the Hartree voltage of π-1 mode, the system always skips π mode oscillations and moves into π-1 mode. Mode competition is a complicated and

challenging problem, it is related to many factors. A detailed discussion will be carried out in the following section.

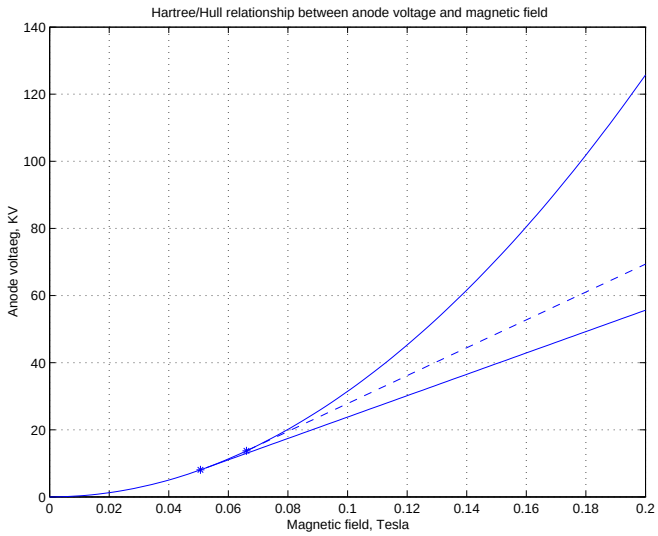

(a)

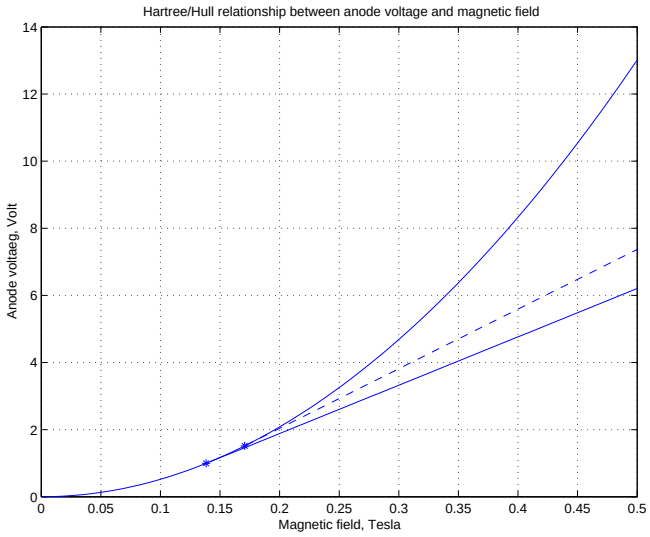

(b)

Figure 2.13: Operating voltage and magnetic field for different modes in S/X band magnetrons (Solid line represents π mode, mode number n=6 for S band, n=9 for X band; dashed line represents π-1 mode, mode number n=5 for S band, n=8 for X band). (a). e2v type S band MG5193 (b). e2v type X band MG5241

2.4.4 Interaction between the RF Field and the electron cloud

The mechanism of interaction between electrons and the RF field in a resonant cavity magnetron is similar to that in a cylindrical diode magnetron. Usually the operating mode in a magnetron is the π mode. In this section the interaction mechanism will be explained whwn the system is oscillating in the π mode.

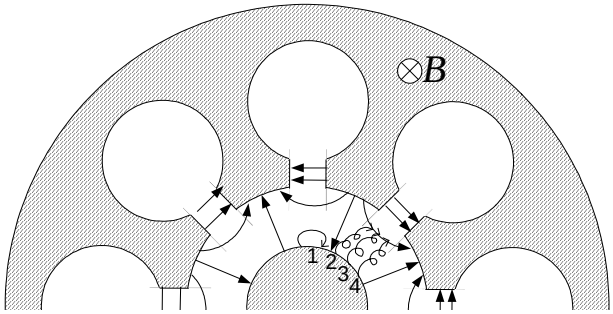

Figure 2.14: Electron trajectories when the system is oscillating in the π mode.

The RF field distribution of π mode is illustrated in Figure 2.14. There are four typical initial positions of electrons inside the cavity, labeled '1', '2', '3', and '4' in the diagram. The RF field affects these electrons differently. Electron '1' is in the accelerating RF field, so it will be speeded up, and the curvature of its trajectory will be increased. Under the combination effects of static electric field and magnetic field, electron '1' will strike back the cathode quickly and thus be removed from the interaction region. Electron '1' won't contribute energy to the RF field; on the contrary, it will consume a small amount of RF energy. Electron '3' is in the decelerating RF field. Its angular velocity will be reduced, resulting in the reduction of its curvature. Such electrons will move towards the anode. If the frequency of the RF field is appropriate, this electron will always be in the decelerating RF field when it passes through the successive anode segments. This electron will keep giving out energy to the RF field until it finally strikes the anode. Electrons '2' and '4' exchange little energy with the RF field. The effect of the RF field is to tune the velocity of their guiding centers. For electron '2', this velocity is increased, thus its guiding center will catch up that of electron '3'; but for electron '4',

its guiding center velocity is reduced, thus it will fall back towards electron '3'. The final result is that electron '2' and '4' move into the decelerating region, and bunch together with electron '3' forming so-called spokes. This kind of phenomenon is called the phase focusing action of the RF field. The four different electron trajectories are also shown in Figure 2.14. Electrons giving up energy to the RF field are called favorable electrons. Electrons absorbing energy from the RF field are called unfavorable electrons. Once oscillations start inside the cavity, unfavorable electrons tend to be removed from the interaction region rather quickly; the favorable electrons, which are in the majority, tend to bunch and move towards the anode while rotating around the cathode at an angular frequency Ω, Eq 2.33.

When the oscillations are stabilized, the electron cloud will be shaped into several spoke-like ridges rotating around the cathode. The number of spokes is determined by the RF mode. For the π mode, in an eight-cavity magnetron, the number of spokes is 4. Figure 2.15 shows electron spokes in an eight-cavity magnetron. This electron cloud rotates around the cathode with an angular velocity Ω, thus keeping it in step with the phase velocity of the RF field and continuously giving up energy to the RF field. Electrons at the end of the spokes land on the anode with velocities well below the DC value of $v = \sqrt{eV_a/2m}$

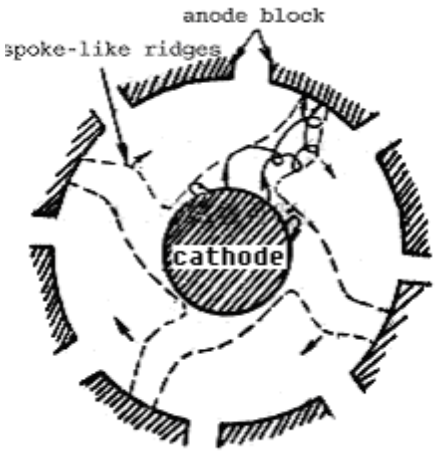

Figure 2.15: Electron spokes in an eight-cavity magnetron when the system is operating in the π mode [2]

2.5 Frequency Stability and Mode Separation

2.5.1 Frequency jumping

For different modes, the charge density on the anode segment is different, which results in the different effective capacitance and inductance, thus the different resonating frequency. Usually the π mode has the lowest resonating frequency and the highest power efficiency, largely because capacitance is maximum in that mode. The π mode is always selected as the operating mode in a magnetron. Unfortunately the frequency difference between π and other modes is not as great as would be desired, therefore frequency jumping from one mode to another can happen. This is undesirable in practice because efficiencies of different modes vary considerably. Low efficiency means low power output and severe heating of the anode and the cathode, and the life shortening of the latter.

Frequency jumping can also happen when the magnetron is operating in a doublet mode. The frequency may jump from that of one component of the doublet to that of the other more easily than it jumps from one mode to another, since the two components of a doublet normally have nearly the same frequencies. Because the two components are coupled to the output to a different extent, slight changes in the output load can cause a jump.

2.5.2 Strapping

In order to improve the mode stability, several methods of mode separation have been developed. One of them is the use of strapping. Alternate anode segments are connected together to help make the phase difference between them to be zero or 2π, thus enforcing the anode to work in the π mode. There are two main forms of strapping, ring strapping and echelon strapping. Figure 2.16(a) shows echelon strapping of an S band magnetron and ring strapping of an X band magnetron is shown in Figure 2.16(b). These two magnetrons will be investigated in Chapter 4 and Chapter 5 respectively.

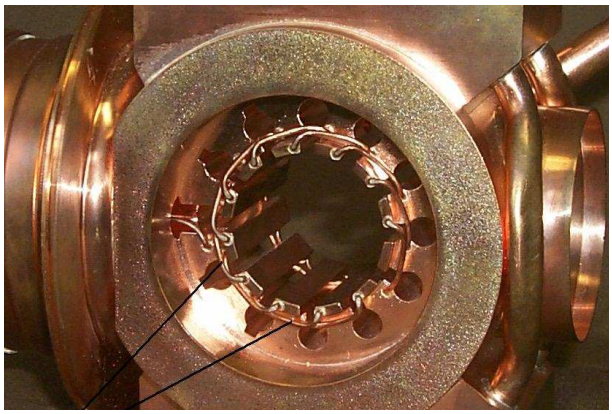

(a)

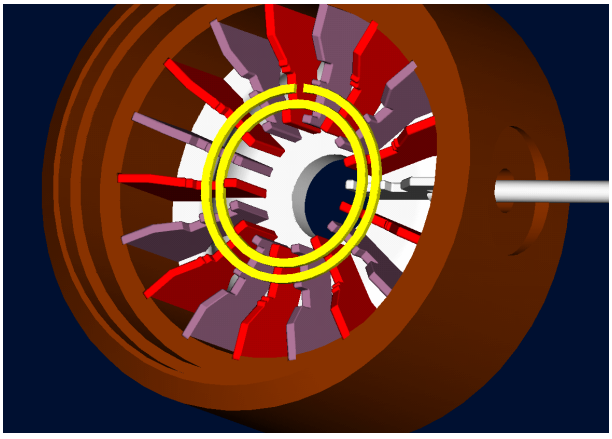

(b)

Figure 2.16: The strapping system. (a)Wire strapping system of an S band magnetron. (b)Ring strapping system of an X band magnetron.

According to the circuit theory, strapping affects the capacitance and inductance of the equivalent circuit, which determines the resonating frequency of the system. When operating in π mode, all the segments connected to one set of straps are at the same potential. There will be no current flowing along the straps. But since the two sets of straps are at different potentials, there will be effective capacitance in parallel with the resonator capacitance, which increases the wavelength. When operating in non-π modes, the two ends of a strap are at different potentials. There will be net current flowing along the straps. The magnitude of the current depends on the potential difference between the ends. The straps therefore act as inductive path, connected in parallel with the effective resonator inductance, the wavelength is therefore reduced. The effect of strapping is

therefore that the frequencies of the non-π modes are increased and that of the π mode is decreased. So, by tuning the strapping system, the π mode and non-π modes can be separated appreciably. Also the Q factors of different modes can be changed by adjusting the straps so that the π mode can dominate the oscillation and other modes are suppressed.

Since it is impossible to make the straps of zero impedance, the possibility for operation in a non-π mode still exists since the strap impedance may cause potential difference between two connected segments. 'Strap breaks' have been introduced to further suppress the non-π modes oscillations. It is found that by introducing some asymmetry into the strapping system, such as removing one or two straps in the case of echelon strapping, Figure 2.16(a), or introducing one or more breaks in the ring straps, Figure 2.16(b), the loaded Q of the lightly coupled component of the doublet can be adjusted to a value nearly equal to that of the heavily coupled one. This makes the non-π modes oscillations less likely. This phenomenon can be explained in another way. When operating in non-π modes, current flows in the straps. By introducing strap breaks, the current flow is stopped, therefore the non-π modes oscillations are suppressed.

2.5.3 Rising sun anode

When the operating frequency is further increased, the dimensions of a strapped magnetron are correspondingly reduced. This makes it very difficult to construct straps. Also small spacing results in a large copper loss and reduced magnetron efficiency. The rising sun anode has been developed to overcome such difficulties. Figure 2.17 shows the geometry of a rising sun anode, which alternately has large and small cavities.

A rising sun anode can be considered as having two resonating systems, one consisting of small cavities and the other of large cavities. The two resonating systems have different resonating frequencies corresponding to all the possible modes as in the equal size cavity magnetron. Naturally coupling exists between the two resonant systems. The

resonant frequency of a rising sun anode is between those of the small and large cavities. By adjusting the ratio of the frequencies of the small and large cavities, the optimum frequency separation between π mode and other modes can be obtained. Another advantage of rising sun anode is that it is no longer necessary for the anode length to be small compared with the wavelength in order to avoid instability. This permits the use of a relatively long anode, enabling higher power generation.

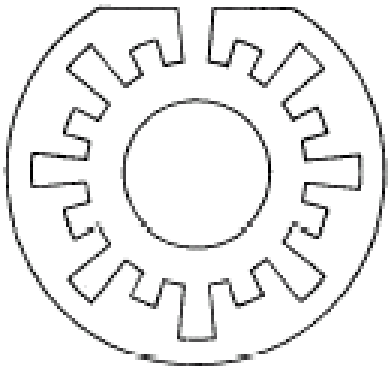

Figure 2.17: Geometry of a rising sun anode [4]

2.5.4 Other factors affecting frequency stability

Besides strapping, there are other methods for mode separation. In Chapter 4, a mechanical tuning mechanism is introduced in an S band magnetron to detune the π-1 mode and change its Q factor in order to encourage π mode oscillations. Ceramic resonators are used in some tubes to absorb π-1 oscillations. Other factors affecting the mode jump include cathode to anode ratio, the regulation of the modulator and the output coupling circuit, etc. By varying the cathode to anode ratio, the operating conditions of Hartree/Hull curves will be changed. The rate of rise of the anode voltage (RRV) is also critical to the start-up of oscillation. A rise which is too steep can cause the magnetron to jump into a non-π modes oscillation. Besides the strapping, it is observed in Chapter 5 that the Q factors of π and π-1 modes can also be tuned by modifying the output coupling circuit, thus suppressing π-1 mode oscillations. Detailed discussion of these items is included in the following chapters.

References

[1] R.S.H.Boulding, Ed., *The Resonant Cavity Magnetron.* The Whitepriars Press Ltd., 1952.

[2] G.B.Collins, Ed., *Microwave Magnetrons.* Massachusetts Institute of Technology, Radiation Laboratory Series, 1948.

[3] P.A.Lindsay, M.Esterson, and X. Chen, "The magnetron 'threshold volatge'revisited," *Phys. Plasmas*, vol. 4, no. 2, pp. 463–468, February 1997.

[4] T.A.Treado, W. Doggett, and G.E.Thomas, "Operating modes of relativistic rising-sun and A6 magnetrons," *Plasma Science, IEEE Transactions*, vol. 16, no. 2, pp. 237–248, April 1988.

Chapter 3

The MAGIC Code and Its Associated Algorithms

3.1 Introduction

In this report, all the simulation work is carried out using a code called MAGIC. The MAGIC code is a Finite-Difference, Time-Domain (FDTD) and Particle-In-Cell (PIC) code for simulating plasma physics processes, i.e., those processes that involve interactions between space charge and electromagnetic fields. Beginning from a specified initial state, the code simulates a physical process as it evolves in time. The full set of Maxwells time-dependent equations is solved by FD-TD algorithm to obtain electromagnetic fields. Similarly, the complete Lorentz force equation is solved to obtain relativistic particle trajectories and the continuity equation is solved to provide current and charge densities for Maxwell's equations. This approach, commonly referred to as the electromagnetic Particle-In-Cell (PIC) technique, provides self-consistent solutions of the interaction process between charged particles and electromagnetic fields [1]. Brief introduction to FD-TD method and PIC algorithm will be given below.

The MAGIC algorithm has been developed in three typical curvilinear coordinate

systems, i.e. Cartesian, Cylindrical and Spherical. The choice of the coordinates usually depends on the geometry of the boundary conditions. In modelling magnetron, a cylindrical coordinate system is the best, since it conforms to the geometry of the cathode and the anode.

3.2 Finite Difference Time Domain Technique

In 1966 Yee [2] introduced FDTD method to solve electromagnetic problems. This method uses simple central difference approximations to evaluate the space and time derivatives in Maxwells time dependant curl equations. The region being modeled is represented by two interleaved grids of discrete points as shown in Figure 3.1. In this diagram, each magnetic field vector component is surrounded by four electric field components, vice versa.

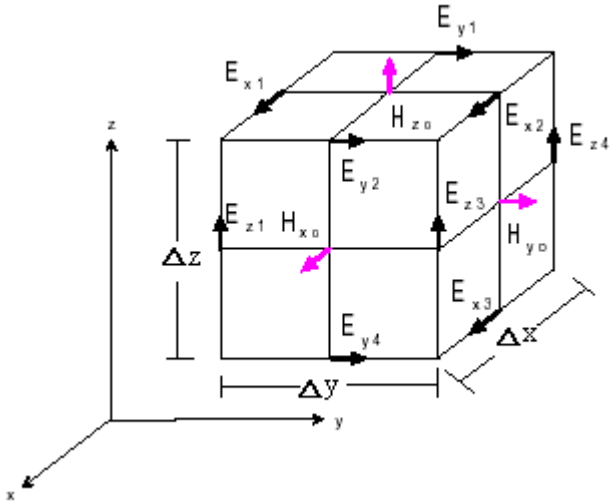

Figure 3.1: Yee's cell, for electric and magnetic field vectors

3.2.1 FDTD algorithm

The Maxwell equations are given by:

$$\nabla \cdot D = \rho \tag{3.1}$$

$$\nabla \cdot B = 0 \tag{3.2}$$

$$\nabla \times E = -\mu \frac{\partial H}{\partial t} \tag{3.3}$$

$$\nabla \times H = \epsilon \frac{\partial E}{\partial t} + J_s \tag{3.4}$$

$$J_s = \sigma E \tag{3.5}$$

Where:

$D = eE$:	Electric flux density
$B = \mu H$:	Magnetic flux density
E:	Electric vector field
H:	Magnetic vector field
μ:	Magnetic permeability
ϵ:	Electric permittivity
J_s:	Electric conduction current density
σ:	Electric conductivity

The leap-frog scheme (see Figure 3.2) is used to update the E and H fields alternately in the time domain. This scheme uses the values of the E field at time t to find the values of H field at time $t+\Delta t$ and then uses the same method to find the values of E at $t+2\Delta t$, thus allowing an electromagnetic wave to march forward over the space grid.

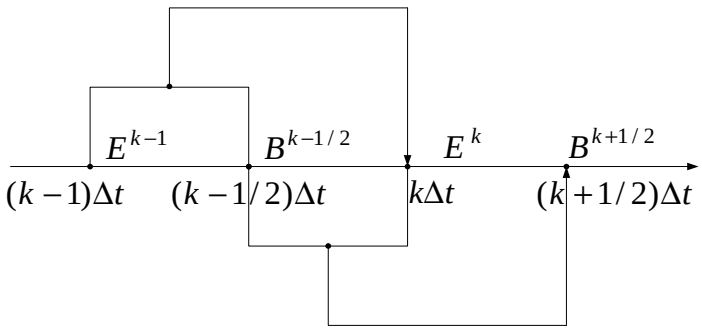

Figure 3.2: The 'leap-frog' time marching scheme

The first order partial derivative, central difference approximation used in FDTD, is given by a Taylor series expansion.

$$\frac{\partial F(x)}{\partial x} = \frac{F(x + (\Delta x/2)) - F(x - (\Delta x/2))}{\Delta x} + O((\Delta x)^2) \tag{3.6}$$

Following Yee's notation, a grid point in the region under investigation can be expressed as

$$(i, j, k) = (i\Delta x, j\Delta y, k\Delta z) \tag{3.7}$$

Thus, any function of space and time can be expressed as

$$A_m^n(i, j, k) = A_m(i\Delta x, j\Delta y, k\Delta z, n\Delta t) = A_m(x, y, z, t) \tag{3.8}$$

Where

A:	Vector electric E or magnetic field H
m:	Vector field component (x, y, z)
Δt:	Temporal increment
Δx:	$\vec{x}$ spatial increment
Δy:	$\vec{y}$ spatial increment
Δz:	$\vec{z}$ spatial increment
i,j,k :	Cartesian spatial grid coordinates
n:	time step

The 2nd and higher order derivatives of the series, which are usually not computed, are treated as a rounded up error of the order $O((\Delta x)^2)$, as indicated in equation 3.6. Applying the above expansion to Maxwell's curl equations, the electric and magnetic

vector field components can be obtained in following equations 3.9 and 3.10.

$$E_z|_{i,j,k}^{n+1} = \left\{\frac{1-\frac{\sigma_{i,j,k}\Delta t}{2\epsilon_{i,j,k}}}{1+\frac{\sigma_{i,j,k}\Delta t}{2\epsilon_{i,j,k}}}\right\}E_z|_{i,j,k}^{n} + \left\{\frac{\frac{\Delta t}{\epsilon_{i,j,k}}}{1+\frac{\sigma_{i,j,k}\Delta t}{2\epsilon_{i,j,k}}}\right\}\left\{\frac{H_y|_{i+\frac{1}{2},j,k}^{n+\frac{1}{2}} - H_y|_{i-\frac{1}{2},j,k}^{n+\frac{1}{2}}}{\Delta x} - \frac{H_x|_{i,j+\frac{1}{2},k}^{n+\frac{1}{2}} - H_x|_{i,j-\frac{1}{2},k}^{n+\frac{1}{2}}}{\Delta y}\right\} \tag{3.9}$$

$$H_y|_{i,j,k}^{n+\frac{1}{2}} = \left\{\frac{1-\frac{\rho_{i,j,k}\Delta t}{2\mu_{i,j,k}}}{1+\frac{\rho_{i,j,k}\Delta t}{2\mu_{i,j,k}}}\right\}H_y|_{i,j,k}^{n-\frac{1}{2}} + \left\{\frac{\frac{\Delta t}{\mu_{i,j,k}}}{1+\frac{\rho_{i,j,k}\Delta t}{2\mu_{i,j,k}}}\right\}\left\{\frac{E_z|_{i+\frac{1}{2},j,k}^{n} - E_z|_{i-\frac{1}{2},j,k}^{n}}{\Delta x} - \frac{E_x|_{i,j,k+\frac{1}{2}}^{n} - E_x|_{i,j,k-\frac{1}{2}}^{n}}{\Delta z}\right\} \tag{3.10}$$

The equations for other field components, E_x, E_y, H_x and H_z can be obtained using the same method.

3.2.2 Numerical stability

The FDTD algorithms for Maxwell's curl equations require that the time increment Δt have a specific bound relative to the lattice increments Δx, Δy, Δz. This bound is necessary to avoid numerical instability, which can cause spurious results increasing without limit as the time marches on. The bound on the time interval is given below

$$\Delta t \leq \frac{1}{c\sqrt{\frac{1}{(\Delta x)^2}+\frac{1}{(\Delta y)^2}+\frac{1}{(\Delta z)^2}}} \tag{3.11}$$

When cubic cells are used ($\Delta x = \Delta y = \Delta z = \Delta$), equation 3.11 can be simplified as

$$\Delta t \leq \frac{\Delta}{c\sqrt{3}} \tag{3.12}$$

where c is the velocity of light. The above two equations state that the maximum allowable time step is determined by the smallest cell size, so that electromagnetic wave

cannot traverse across a grid in one time step.

The above discussion focused on the numerical stability of the basic Yee algorithm in Cartesian coordinates. However, the stability of the entire FD-TD procedure for Maxwell's equations depends upon more than the stability of the Yee algorithm. In fact, a generalised stability problem arises due to interactions between the Yee algorithm and augmenting algorithms used to model: boundary conditions; variable and unstructured meshing; lossy, dispersive, nonlinear, or active materials.

3.2.3 Uncertainty analysis

The numerical algorithm for Maxwell's equations defined by the FDTD method can cause numerical dispersion of the simulated wave modes in the computational lattice. That is, the phase velocity of the simulated wave in the FDTD grid can differ from the vacuum speed of light, varying with the modal wavelength, the direction of propagation in the grid, and the grid discretization. So a proper grid discretization, usually smaller than one tenth of the wavelength, is used to minimize this error.

Staircase within rectilinear FDTD grids related to material boundary can also cause uncertainty. The well-known contour path modelling, or fuzzy technique, deriving effective permittivities by looking at electric flux field values represents a simple alternative method compared to sophisticated gridding to avoid staircase effects without additional computational cost during the time-stepping algorithm.

3.2.4 Absorbing boundary condition

In order to model open region problems, an absorbing boundary condition (ABC) is often used to truncate the computational domain, since the tangential components of the electric field along the outer boundary of the computational domain cannot be updated using the Yee algorithm. Most of the popular ABC's can be grouped into those that are

derived from differential equations or those that employ a material absorber.

The absorbing boundary condition has been introduced by Taylor et al [3], who use a simple extrapolation method. A partial differential equation that permits wave propagation only in certain directions is called a one-way equation. When applied at the outer boundary of an FDTD grid, a one-way wave equation numerically absorbs impinging scattered waves. Engquist and Majda derived a theory of the one-way wave equation suitable for ABCs in Cartesian FDTD grids [4]. Based on Engquist-Majda's formulation, Mur developed a second order ABCs [5], which annihilates the normal incident wave quite accurately. However for oblique incident waves, large reflections can occur. Taflove introduced losses in the region that surrounds the structure being modeled, which absorbs both the outgoing waves and the waves that are reflected by the boundaries of the mesh. The use of material ABC's made a significant advance in 1994 with the work of Berenger [6]. Berenger's ABC, termed the perfectly matched layer (PML) absorbing boundary condition, employed a 'split-field' artifice to ensure that the phase velocity tangential to the PML region was the same as in free space for all frequencies and for all angles of incidence.

3.3 Particle In Cell (PIC) Technique

3.3.1 The Computational cycle

The general computational cycle for interaction between electrons and electromagnetic fields is demonstrated in Figure 3.3. This cycle starts with some appropriate initial conditions on the particle positions and velocities. The particle quantities are known at the particle and may take on all values in phase space. The field quantities will only be obtained on the spatial grids, that is, discrete points. In order to calculate the field quantities on the grids, the charge and current densities on the grids must be known first. This process of assigning particle charge and current on the grid is a kind

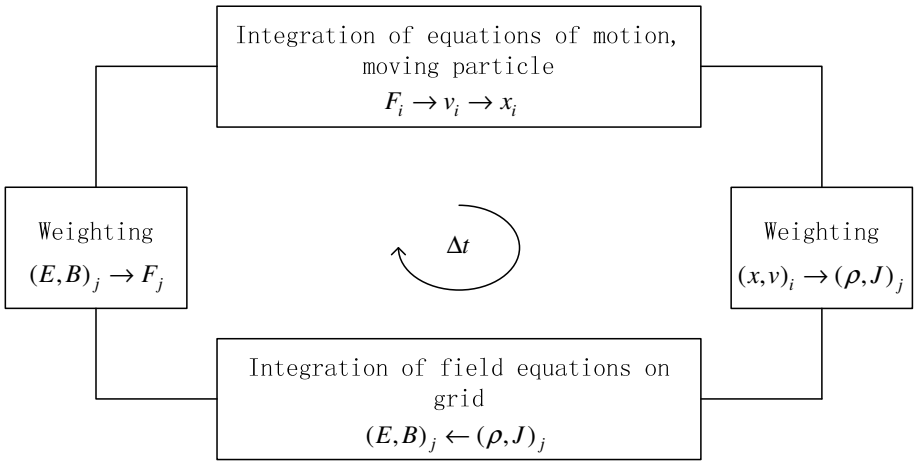

Figure 3.3: A typical cycle in PIC processing [7]

of 'weighting', which depends on the particle position. Once the charge and current densities are established on the grid, various kinds of numerical methods can be used to obtain the electric and magnetic field components. With the fields known on the grid, the electromagnetic forces acting on particles can be obtained through interpolating the grid fields and the particle position. Thus the electron can be marched forward. This process includes another weighting of the field components and the particle [7–9].

3.3.2 Integration of the equations of motion

The Leap-frog method is used to solve the particle motion equations because of its simplicity and accuracy. A first-order example is illustrated here. The two first-order differential equations to be integrated separately for each particle are

$$m\frac{\vec{v}}{dt} = \vec{F} \tag{3.13}$$

$$\frac{d\vec{x}}{dt} = \vec{v} \tag{3.14}$$

Where

$\vec{F}$: the electromagnetic force acting on the particle
m : particle mass
$\vec{v}$: particle velocity
$\vec{x}$: particle position

These equations are replaced by finite difference equations

$$m\frac{\vec{v}_{new}-\vec{v}_{old}}{\Delta t}=\vec{F}_{old} \tag{3.15}$$

$$\frac{\vec{x}_{new}-\vec{x}_{old}}{\Delta t}=\vec{v}_{new} \tag{3.16}$$

The flow in time and notation are shown in Figure 3.4. The program is time centering and will advance the velocity and position alternately. That is, $\vec{v}$ and $\vec{x}$ cannot be known at the same time. That is why this method is called leap-frog method.

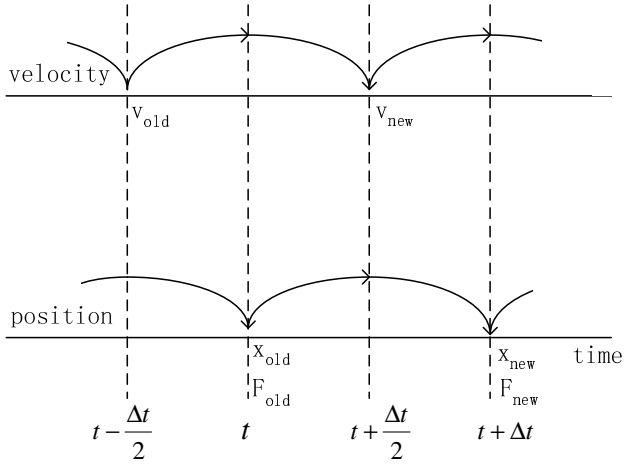

Figure 3.4: Sketch of leap-frog integration method showing time centering of force $\vec{F}$ while advancing $\vec{v}$, and of $\vec{v}$ while advancing $\vec{x}$ [7]

Two issues must be addressed here. First, the initial conditions for particle velocities and positions must be modified to fit in the flow. Using the force $\vec{F}$ at t=0, velocity $\vec{v}(t=0)$ is pushed back to $\vec{v}(t=-\frac{\Delta t}{2})$. Second, the energies calculated from $\vec{v}$(kinetic) and $\vec{x}$(potential, or field) must be adjusted to appear at the same time.

3.3.3 Particle and force weighting

As described in Figure 3.3, the computing cycle of PIC performs two weighting calculations. One is the charge and current weighting, and the other is the field or force weighting. In order to calculate the force on the grid points, it is necessary to calculate the charge and current density on the discrete grids from the particle. This process is performed by interpolating the particle charge between neighbouring grids. A zero order example is shown in Figure 3.5.

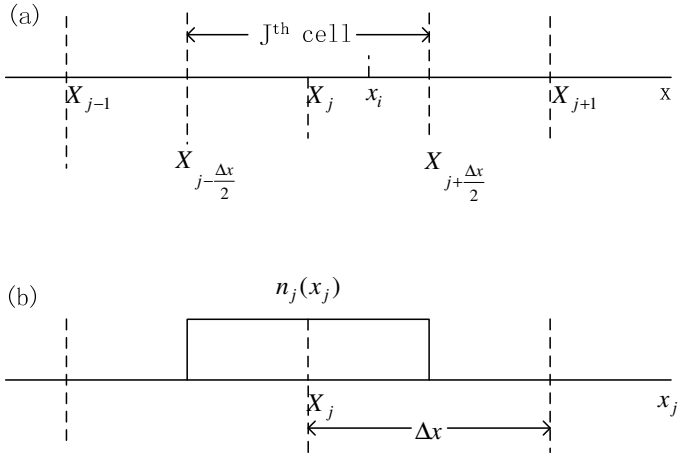

Figure 3.5: The scheme for the zero order charge and current weighting [7]

The grid charge density $n(j)$ at grid point j is obtained by assigning all the particles $N(j)$ within the j^{th} cell (from $j - \Delta x/2$ to $j + \Delta x/2$), that is $n(j) = \frac{N(j)}{\Delta x}$, as shown in Figure 3.5. This weighting is called nearest-grid-point weighting or NGP. When particles move in or out of the j^{th} cell, the grid density will jump up or down, making the observed particles to have a finite size rather than a point size. One effect of this jumping is that it introduces associated density and field random jumps or 'noise', both in space and time. This noise may become intolerable in many plasma physics problems. Higher order weighting can avoid this problem.

The field or force weighting can be conducted in the same manner. The zero order of the NGP force comes from the field at the nearest grid point, that is $E(x_i) = E(x_j)$. Where x_i is the position of the particle, x_j is the nearest grid point to x_i. Discussion for

higher order weighting can be found in [7, 9].

3.4 Emission Models in MAGIC Code

The MAGIC code provides several emission models to simulate different emission processes, such as the thermionic emission, the photoelectric emission, the space-charge-limited emission, the beam emission, the secondary emission or the high field emission. The emission models used in our modelling work are the space-charge-limited emission, the beam emission and the secondary emission. They will be described briefly below. Detailed explanation of the emission models can be found in the MAGIC manual book [1].

3.4.1 The space-charge-limited emission

In MAGIC, the space-charge-limited emission is given the name 'explosive emission'. In the computer model, the physical details of the explosive emission, which results from the plasma formation on a material surface, have been ignored. Instead, the computer model relies on a phenomenological description. The particle emission itself is based upon Child's law, specifically, the normal electric field vanishing at the emitting surface.

In the phenomenological treatment of plasma formation, breakdown can occur only if the normally directed field at the half-cell, E_c, exceeds some specified breakdown field threshold, $E_c > E_{threshold}$. If the field at a particular cell exceeds the threshold, then that cell is said to 'break down'. A single, non-emitting cell between two emitting cells is also allowed to break down, even if the threshold is not exceeded. Once initiated by breakdown, plasma formation in a cell is assumed irreversible. Thus, a cell that has broken down may 'emit' charged particles due to the influence of the ambient electric field. The calculation of the charge that would be drawn away from a surface is based upon application of Gauss's law to the half-cell, allowing for a small residual field at the surface, $dQ/dA = \varepsilon_0(E_c - E_r) - \rho$, where dQ/dA is the emitted charge, E_r is the residual

field at the surface, ρ is the existing charge density at the surface.

3.4.2 The beam emission

With the beam emission model, the emission from a surface has the emission current density and the initial beam voltage, specified by the user. The initial kinetic energy and momentum for each particle are computed relativistically from the beam voltage. The beam emission model also provides options to vary the beam direction and distribution by either thermalizing the beam or giving it a specific direction (differen from the normal) to the surface. For example, the 'THERMALIZATION' option allows you to specify a fraction of the beam energy to be distributed randomly in the transverse coordinates. The energy in each coordinate is determined randomly, and the dominant (normal) component is re-normalized to preserve the exact specified beam voltage.

3.4.3 The secondary emission

With this emission model, secondary electrons are emitted from the surface of a conducting spatial object when it is hit by primary particles. Figure 3.6 illustrates the coordinate system. The polar angles of the primary particle and the secondary electron, θ_p, θ_s, are measured with respect to the surface normal.

The secondary emission yield depends upon the primary particle energy E_p and angle of incidence θ_p, and upon the material-dependent parameters, the peak yield δ_{peak} and the primary energy at peak yield E_{peak}. In MAGIC, the secondary emission coefficient, δ, is assumed to be a product of two functions, one in the primary polar angle and one in primary energy.

$$\delta(E_p, \theta_p) = \frac{\delta_0(E_p)}{cos(\theta_p)} \tag{3.17}$$

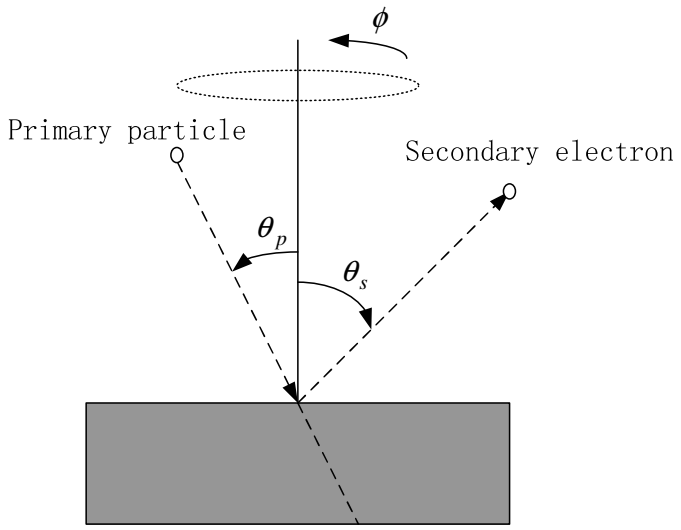

Figure 3.6: Coordinate system illustrating primary particle and secondary electron

$$\delta_0(E_p) = \delta_{peak} \frac{E_p}{E_{peak}} exp(-2\sqrt{\frac{E_p}{E_{peak}}}) \tag{3.18}$$

Here, δ_0 is the secondary emission coefficient at normal incidence for the primary particle. An artificial cutoff in the polar angle dependence (at 85 degrees) is employed to prevent the coefficient from going to infinity for grazing angles. On default, the secondary energy distribution is peaked at 7.5 eV with a full-width at half-maximum of 10 eV. The angular distribution is homogeneous, having no preferred direction.

References

[1] L.Ludeking, Ed., *Manual of MAGIC Tool Suite*. Mission Research Corporation, 2002.

[2] K.S.Yee, "Numerical solution of initial boundary value problems involving maxwell's equations in isotropic media," *IEEE Trans on Antennas and Propagation*, vol. 14, no. 4, pp. 302–307, 1966.

[3] C.D.Taylor, D.H.Lam, and T.H.Shumpert, "Electromagnetic pulse scattering in time-varying inhomogeneous media," *IEEE Trans on Antennas and Propagation*, vol. 14,

no. 4, pp. 302–307, 1966.

[4] B.Engquist and A.Majda, "Absorbing boundary conditions for the numerical simulaiton of waves," *Math. Comp*, vol. 31, pp. 629–651, 1977.

[5] G.Mur, "Absorbing boundary conditions for the Finite-Difference approximation of the Time-Domain electromagnetic-field equations," *IEEE Trans. Electromagnetic Compatibility*, vol. 23, pp. 377–382, 1981.

[6] J.P.Berenger, "A perfectly matched layer for the absorption of electromagnetic waves," *Journal of Computational physics*, vol. 114, pp. 185–200, 1994.

[7] C.K.Birdshall and A.B.Langdon, Eds., *Plasma Physics Via Computer Simulation.* McGraw-Hill, New York, 1985.

[8] C.K.Birdshall, "Particle-in-cell charged-particle simulations, plus monte carlo collisions with neutral atoms," *IEEE Transactions on Plasma Science*, vol. 19, no. 2, pp. 65–85, April 1991.

[9] R.W.Hockney and J.W.Eastwood, Eds., *Computer Simulation Using Particles.* Adam Hilger, Bristol, 1988.

Chapter 4

Modelling of an S band Magnetron

An S band 'slot and hole' magnetron (e2v technologies type MG5193) has been modeled using the 3D version of the MAGIC code. The anode structure of the S band magnetron (MG5193) is illustrated in Figure 4.1. The underlying symmetries are two perpendicular polar systems, the output system and the anode system. For the convenience of respectively computer modelling, these two parts will be investigated and analysed separately in sections 4.1 and 4.2.

Figure 4.1: Image of an S band magnetron (e2v type MG5193)

4.1 Modelling of The Output System

4.1.1 Introduction

Simulation of the output system of the S band magnetron has been carried out because when the glass dome was replaced by a ceramic one the two metal rods forming the output coupling loop would always melt in operation and thus destroy the magnetron. Here, the dome is a vacuum tight RF window, see Figure 4.1. The computer model of the output system is shown in Figure 4.2, where the melting points are marked in red. The two coaxial coupling rods are connected by a dipole antenna forming a double loop. The output port of the system is a rectangular waveguide, which is connected to the circular waveguide through a kind of 'water-fall' transition. Figure 4.3 shows a 3D picture of transition. The RF power generated in the anode-cathode cavity reaches the output system through two coaxial line ports, which feed the dipole antenna. In the circular part of the output system the RF power travels as a TE_{11} wave and is then transformed to a TE_{10} wave as it enters the rectangular waveguide.

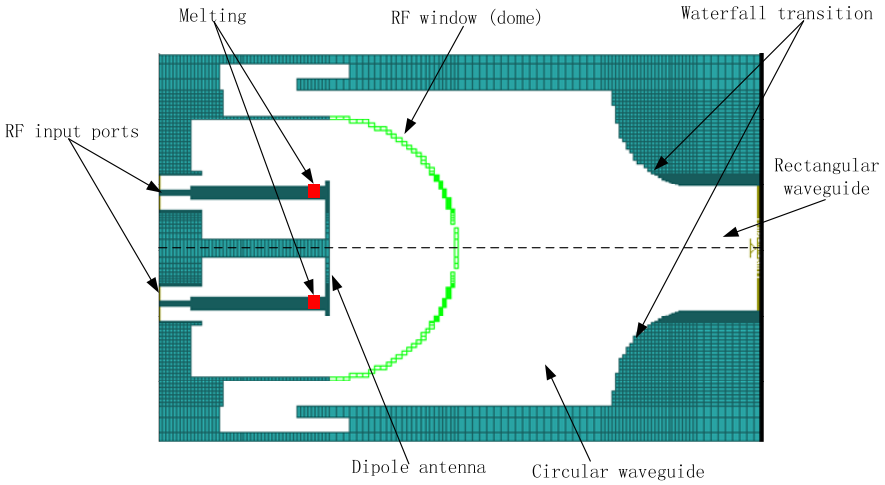

Figure 4.2: The geometry of the output of the S band MG5193 magnetron

In order to explain the melting phenomenon, various possible reasons have been looked at. Computer modelling has been conducted to check the resonance spectrum, input and output power, current and voltage distribution. Also, an investigation of the

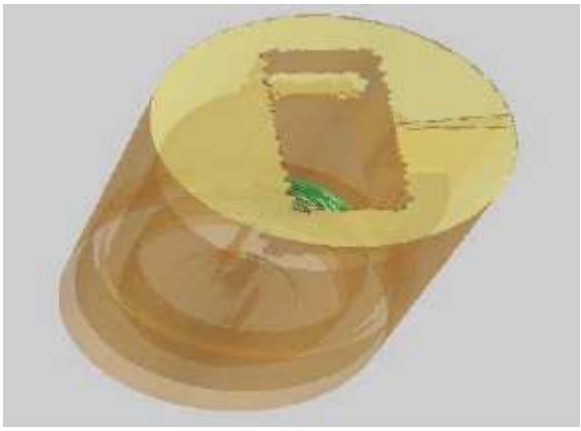

Figure 4.3: Computer model of the rectangular output of the S-band MG5193 magnetron

possible multipactor effect between the input coupling rods has been carried out.

4.1.2 Cutoff frequency and possible modes in the output system

The cutoff frequencies of various modes in the circular wave-guide and the rectangular wave-guide of the output system have been calculated in order to check all possible modes that could be supported.

Polar coordinates have been selected, with the axis of the output waveguide in the z direction. For the TM ($H_z = 0$) modes inside the circular waveguide, the boundary conditions require E_z and E_ϕ to be zero at the outer wall (r=a), resulting in $J_n(k_c a) = 0$. $J_n(x)$ is a Bessel function of the first kind, 'n' denotes angular variation.

$$k_c a = \omega_c \sqrt{\mu\epsilon} a = \frac{2\pi a}{\lambda_c} = p_{nl} \tag{4.1}$$

For a given 'n', the cutoff frequency of a TM mode is given by

$$f_c = \frac{p_{nl}}{2\pi a \sqrt{\mu\epsilon}} \tag{4.2}$$

where 'l' indicates the root number and refers to radial variations. The cutoff frequency of the TE($E_z = 0$) mode in a circular waveguide can be calculated in the same way. In

this case the boundary conditions at r=a require $E_\phi = 0$, so that

$$k_c a = \omega_c \sqrt{\mu\epsilon} a = \frac{2\pi a}{\lambda_c} = p_{nl}^{'} \tag{4.3}$$

where $J_n^{'}(p_{nl}^{'}) = 0$. $J_n^{'}(x)$ is the first derivative of Bessel function, again 'n' denotes angular and 'l' denotes radial variation. For given 'n' and 'l', the cutoff frequency of a TE mode is given by

$$f_c = \frac{p_{nl}^{'}}{2\pi a \sqrt{\mu\epsilon}} \tag{4.4}$$

For the circular waveguide the radius of the waveguide is a=35mm between the input ports and the dipole antenna. The possible modes and their corresponding cutoff frequencies are shown in Figure 4.4.

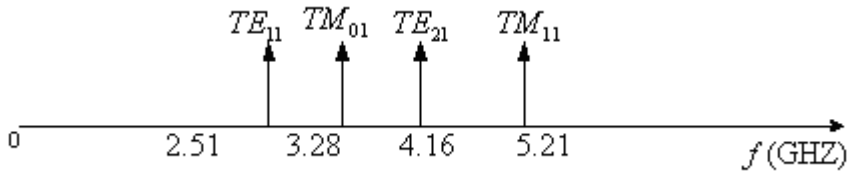

Figure 4.4: The cutoff frequencies of the circular wave-guide (a=35mm)

The radius of the middle section (beyond the dipole antenna) of the circular waveguide is a=42.9mm. Its possible modes and corresponding cutoff frequencies are shown in Figure 4.5.

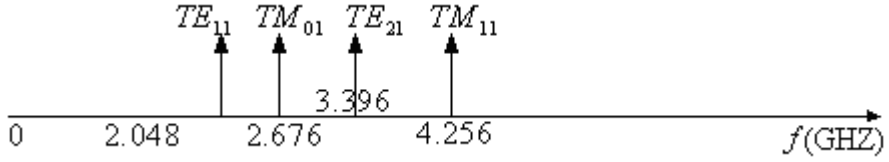

Figure 4.5: The cutoff frequencies of the circular wave-guide (a=42.9mm)

Since the operating frequency is 2.998GHz, the only possible mode in the small radius section of the waveguide is the TE_{11} mode. But in the middle section, two possible modes may be present, TE_{11} and TM_{01}.

In the rectangular part of the waveguide, the cutoff frequencies are the same for TE

and TM modes, except that for a TM wave neither 'm' nor 'n' (Eq 4.5) can be zero. So, there are no TM_{01} or TM_{10} modes.

$$f_c = \frac{1}{2\pi\sqrt{\mu\epsilon}}\sqrt{\frac{m\pi}{a}^2 + \frac{n\pi}{b}^2} \tag{4.5}$$

where 'm' and 'n' are integers. The dimensions of the rectangular waveguide are a=34mm, b=72mm. Calculations shows that only the TE_{10} mode can propagate, its cutoff frequency being 2.08Ghz, see Figure 4.6.

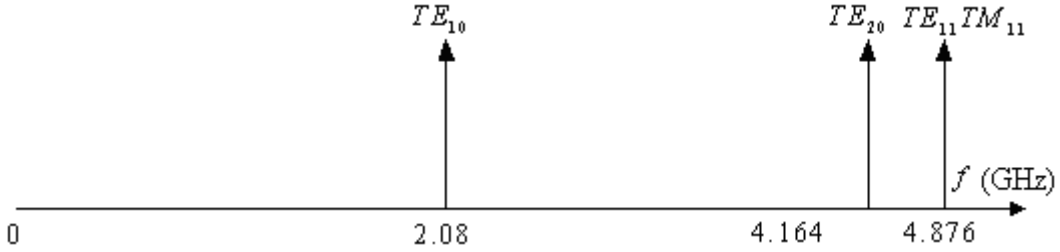

Figure 4.6: Cutoff frequencies of the rectangular wave-guide

When the system is operating at 2.998GHz, besides the operating mode TE_{11}, TM_{01} may also be excited in the circular waveguide. But in the rectangular section, only the TE_{10} mode is possible. The TE_{11} mode in a circular waveguide has the same field distribution as the TE_{10} mode in a rectangular waveguide. Thus, the rectangular output can transmit RF power in the TE_{10} mode. The field distribution of the mode is discussed in next section.

4.1.3 Modelling of the output system

The resonance spectrum and current distribution on the input rods and the antenna have been investigated through computer modelling. The results are presented here in the form of tables and diagrams. All the simulation has been completed using the MAGIC code, which has been introduced in Chapter 3.

4.1.3.1 Current distribution on the input rods and the dipole

As introduced at the beginning of this chapter, when the glass dome is replaced by a ceramic one, the two coupling rods always melt during operation. Therefore the objective of the investigation of the output system was to find the reason for the melting. The current and voltage distribution along the two coupling rods and the dipole antenna have been measured to see if RF overheating causes the melting. The power level of this magnetron is 4MW, pulsed. The input voltage and current on each input port are respectively 20kV and 100Amps (peak values).

Figure 4.7(a) shows the current distribution on the coupling rod with both glass dome and the ceramic dome. It drops sharply where the dimension of the rod changes. This is due to the discontinuity of the impedances at that point. The current distribution along the dipole is shown in Figure 4.7(b); it shows that the current decreases from the center of the dipole towards the two ends. The currents in these diagrams are all peak values.

Figures 4.7(a) and 4.7(b) present the current distributions on the rod and the radiating dipole with ceramic and glass domes respectively. It indicates that with the ceramic dome, the dipole current is higher than with the glass dome, but the current distribution on the rod is flatter. It is obvious that for both glass and ceramic domes the highest current is in the feeding coax lines near the input port, which are thinner in dimension than the rods and the bar. Considering the 'melting problem' addressed at the beginning of this chapter, conclusion can be reached that RF overheating cannot be the reason for the melting of the metal rod, because if it is the current that causes the melting, the two coaxial lines should melt first.

4.1.3.2 Effect of the dome

The effects of the dome have been investigated. Simulations have been carried out with the glass dome, the ceramic dome and without the dome. It is found that when the dome

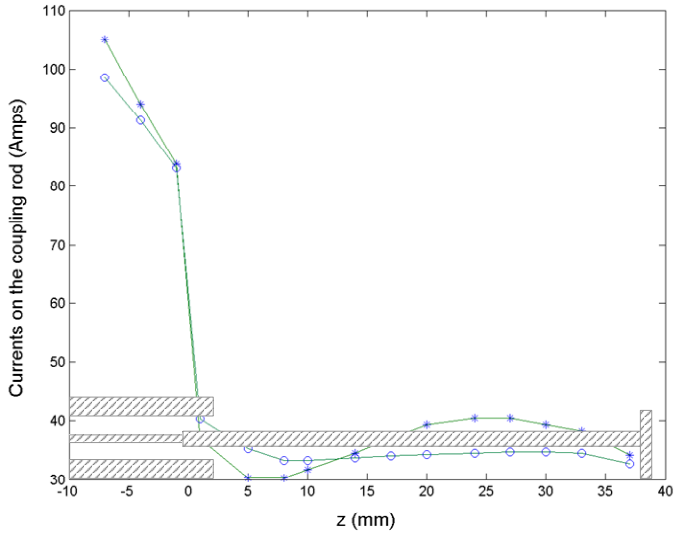

(a)

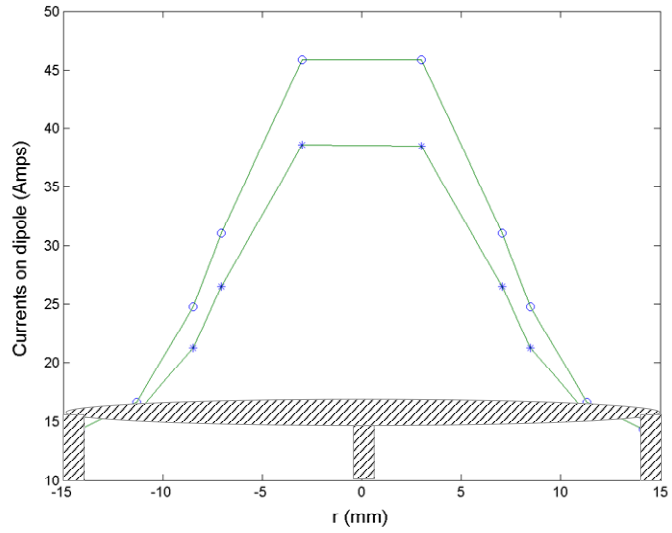

(b)

Figure 4.7: (a)Current distribution along the coupling rod. (b) Current distribution along the radiating dipole. ('$*$': glass dome; '$\circ$': ceramic dome)

is removed, the reflection is getting bigger. Also from the simulation it is observed that the ceramic dome has smaller reflection than the glass dome. The results are shown in Figures 4.8 to 4.10.

In these diagrams, instant power is obtained by integrating Poynting vector at the input port. The positive values represent the transmitted power; the negative values represent the reflected power. The rate of reflection is obtained by dividing the reflected

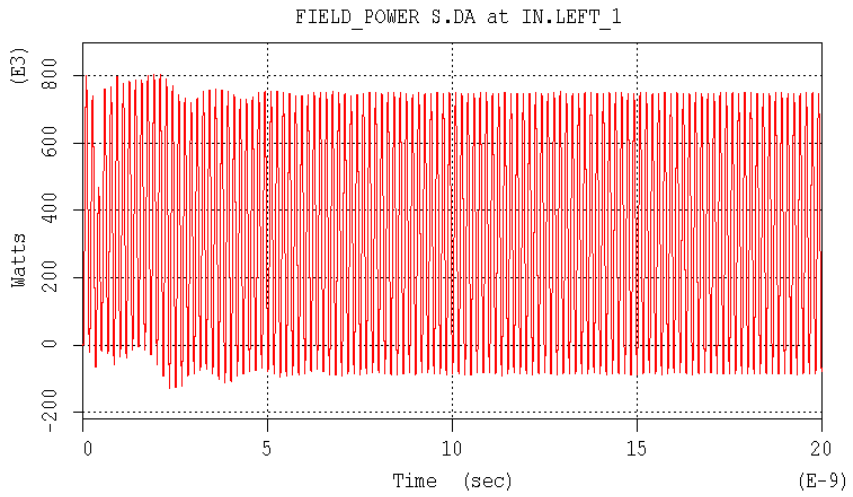

Figure 4.8: Transmitted and reflected power at the input port with a glass dome (Power reflection: 11.5%)

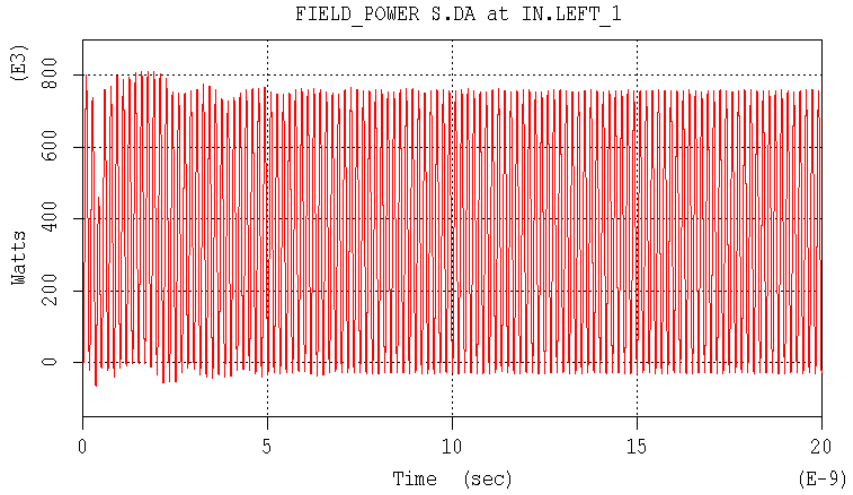

Figure 4.9: Transmitted and reflected power at the input port with a ceramic dome (Power reflection: 4.0%)

by the transmitted power. The magnitudes in these diagrams have no absolute meaning, therefore they should not be compared with each other. Table 4-A compares the reflections with and without the domes. The reason of the reflection increase when without the dome is that the dome acts as a kind of impedance match to the connecting waveguide. When the dome is removed, the impedance matching of the waveguide system deteriorates, therefore the reflection increases.

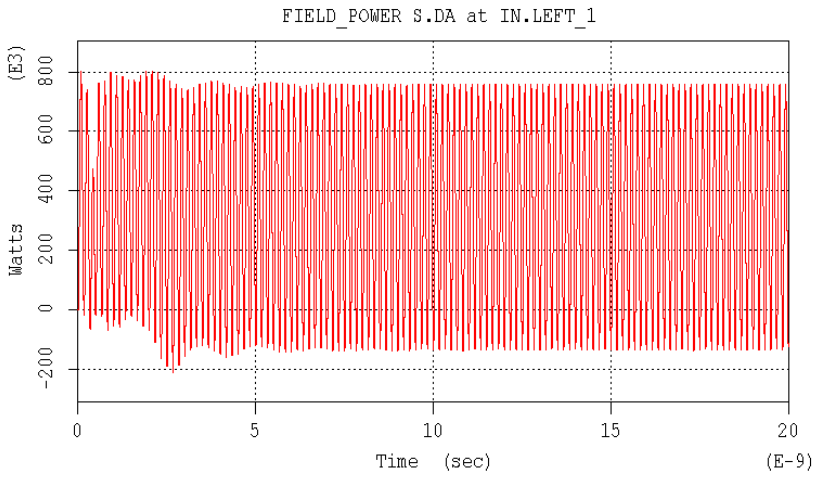

Figure 4.10: Transmitted and reflected power at the input port without a dome (Power reflection: 17.8%)

Table 4-A: Comparisons of the power reflections with and without domes

Dome type	Ceramic dome $\epsilon_r = 9$	Glass dome $\epsilon_r = 4$	Without dome $\epsilon_r = 1$
Power reflection	4.0%	11.5%	17.8%

4.1.4 Preliminary study on possible multipactor effects inside the output system

It is concluded from the previous section that the reason for the melting of the two coupling metal rods when the glass dome is replaced by a ceramic one cannot be due to the RF current, which is only of the order of 40 Amps. It seems that if the RF current in the coupling loop was the reason for the loop melting the small diameter input leads should melt first.

Other possible explanations for the observed melting could be a spurious resonance due to the ceramic window, anomalous field distributions around the loop with higher order modes, multipactor effects and plasma discharge, possibly affected by any stray magnetic field in the region of the loop. The present hypothesis is that the localised multipactor causes some gas evolution and a gas discharge is sustained by the RF power generated by the magnetron and this melts the surface of the rods. The computer modelling has therefore been concentrated on investigating the possibility of multipactor

in the output system.

The Multipactor discharge is a resonant vacuum discharge frequently observed in microwave systems, such as RF windows, accelerator structures, microwave tubes and other devices. The underlying mechanism is an avalanche caused by secondary electron emission. Primary electrons accelerated by RF fields upon impact on a surface, release a large number of secondary electrons, which may in turn be accelerated by the RF fields and impact again, releasing even more electrons, and so on. The discharge can take place on a single surface or between two surfaces [1–4]. Multipactor is usually undesirable. It can dissipate substantial amounts of energy or detune a microwave signal. The discharge also heats the surface, possibly increasing noise level and causing damage by destroying vacuum.

What concerned us most is how the multipactor may develop on the metal rods of the output system of the S band magnetron and the electro-magnetic conditions which accompany it. Figures 4.11(a) to 4.11(b) show vector plots of the electric field excited inside the output system when a 3GHz RF signal is applied through the input ports. Figure 4.11(b) is half RF period later than Figure 4.11(a).

The multipactor possibilities between different metal rods and surfaces can be analyzed by calculating the electron transit time in the first instance. Because the electric field distribution between the metal rods is not uniform, strict analytical calculation of the electron transit time in this area is not feasible. A simple calculation has been carried out to estimate the electron transit distance within half RF period. The RF voltage oscillation between the central support rod and the coupling rod is shown in Figure 4.12, with peak value of 4.7kV.

The distance between the two rods is 10.98mm. Assuming the electric field between the central support rod and the coupling rod is uniformly distributed. We obtain $E_{max} = 4.7kV/10.98mm = 428kV/m$. Within one half of the RF period, the distance the electron

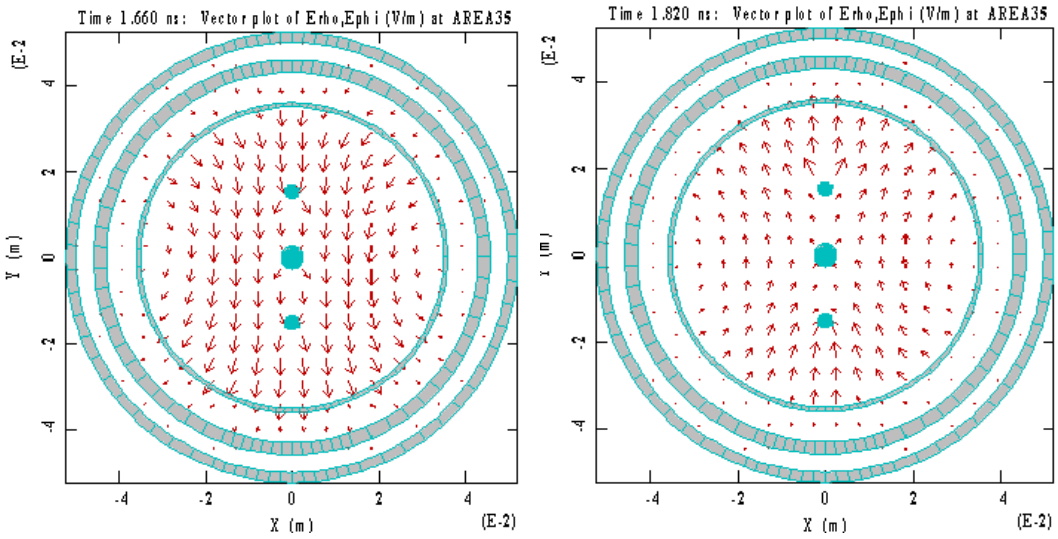

Figure 4.11: A cross section of the electric vector field just below the dipole antenna where the melting points are situated. (a) t=1.660ns (b) t=1.820ns

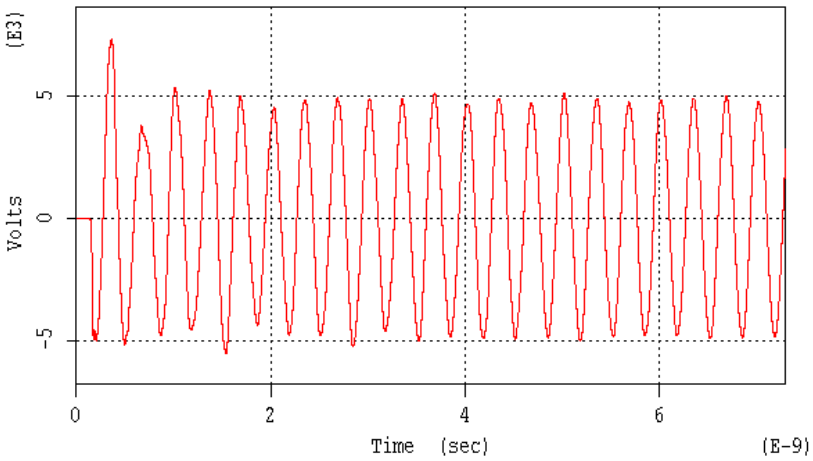

Figure 4.12: Voltage oscillation between the central support rod and one of the coupling rods. The applied signal operates at 2.998GHz with peak power of 4MW.

can travel is calculated using Eq. 4.6.

$$s = v_0 t + \frac{1}{2} a t^2 \tag{4.6}$$

where v_0 is the initial velocity, t equals to half RF period and a is the acceleration caused by the electric field.

In computer modelling, secondary electrons are released from the coupling rod with initial energy 0.5eV. Therefore the initial velocity can be obtained, $v_0 = 4.2e5m/s$. With operating frequency 2.998GHz, the half RF period is $t = 1/(2f) = 0.167ns$. For a crude estimation, considering only the effect of the electric field, the acceleration speed of the electron is $a = eE/m = 7.5e16m/s^2$, where e is the electron charge and m its mass. The approximate distance an electron can travel within half RF period is therefore $s \approx 1mm$.

Due to the complexity of the electromagnetic field distribution, computer modelling seems to be the only feasible approach to identify the areas where multipactor might take place and to discover the required electro-magnetic field conditions.

In the output system, all the surfaces of the metal rods and the waveguides are set to be able to emit secondary electrons when struck by primary electrons. A typical value for the secondary emission coefficient of copper has been used for the metal rods and the waveguides, its maximum value is 1.3 with a primary energy of 500 eV.

Simulations with different levels of RF input power and different emission phases of the primary electrons have been conducted. Simulations have shown that the primary electrons released from the melting regions seem to knock off a large number of secondary electrons at the point where the central support rod joins the dipole; also the secondary electrons then back bombard the melted region. Simulations have also shown that the yield of the secondary electrons is more sensitive to the phases of the RF field than to the power level of the RF field. The phase of 0.5π seems to be a favorite one, which generates the largest number of secondary electrons which then keep bombarding the coupling rods. This process is shown in Figure 4.13, where red dots represent primary electrons and purple dots the secondaries. The dome is ceramic, with $\epsilon_r = 9$.

In order to compare the effect of different domes, simulation with a glass dome has been carried out with the same conditions as those for the 'ceramic' simulation. Figure 4.14 shows the electron bombardment when a glass dome is present. Comparing Figure 4.13(f) with Figure 4.14(f), it seems that the secondary electron cloud is more

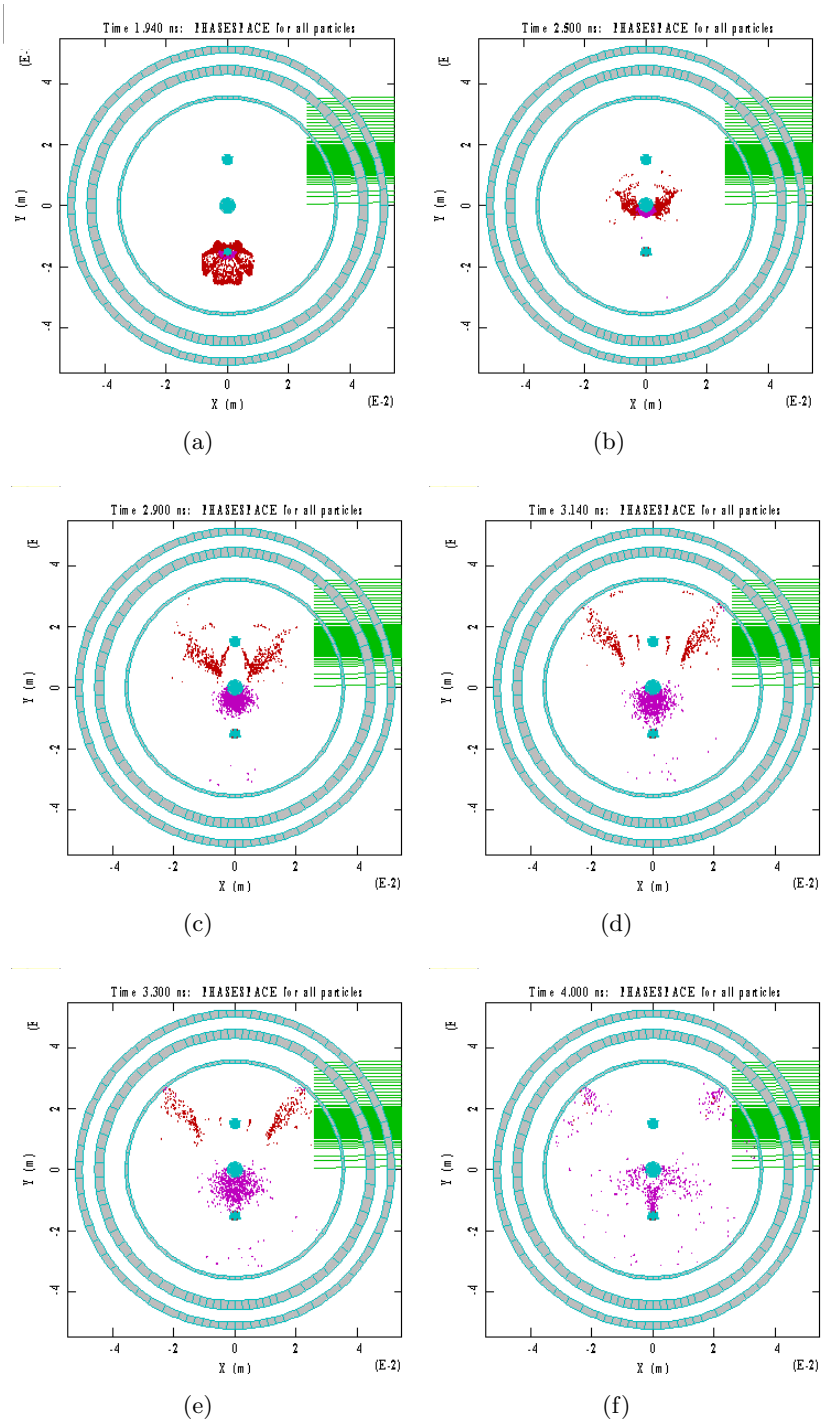

Figure 4.13: Snap shots of electron clouds (RF power: 4MW; Phase of RF field while primary electrons are released: 0.5π; Ceramic dome: $\epsilon_r = 9$; Red colour represents primary electrons; Purple colour represents secondary electrons.) (a) t= 1.940ns (b) t=2.500ns (c) t=2.900ns (d) t= 3.140ns (e) t=3.300ns (f) t=4.000ns

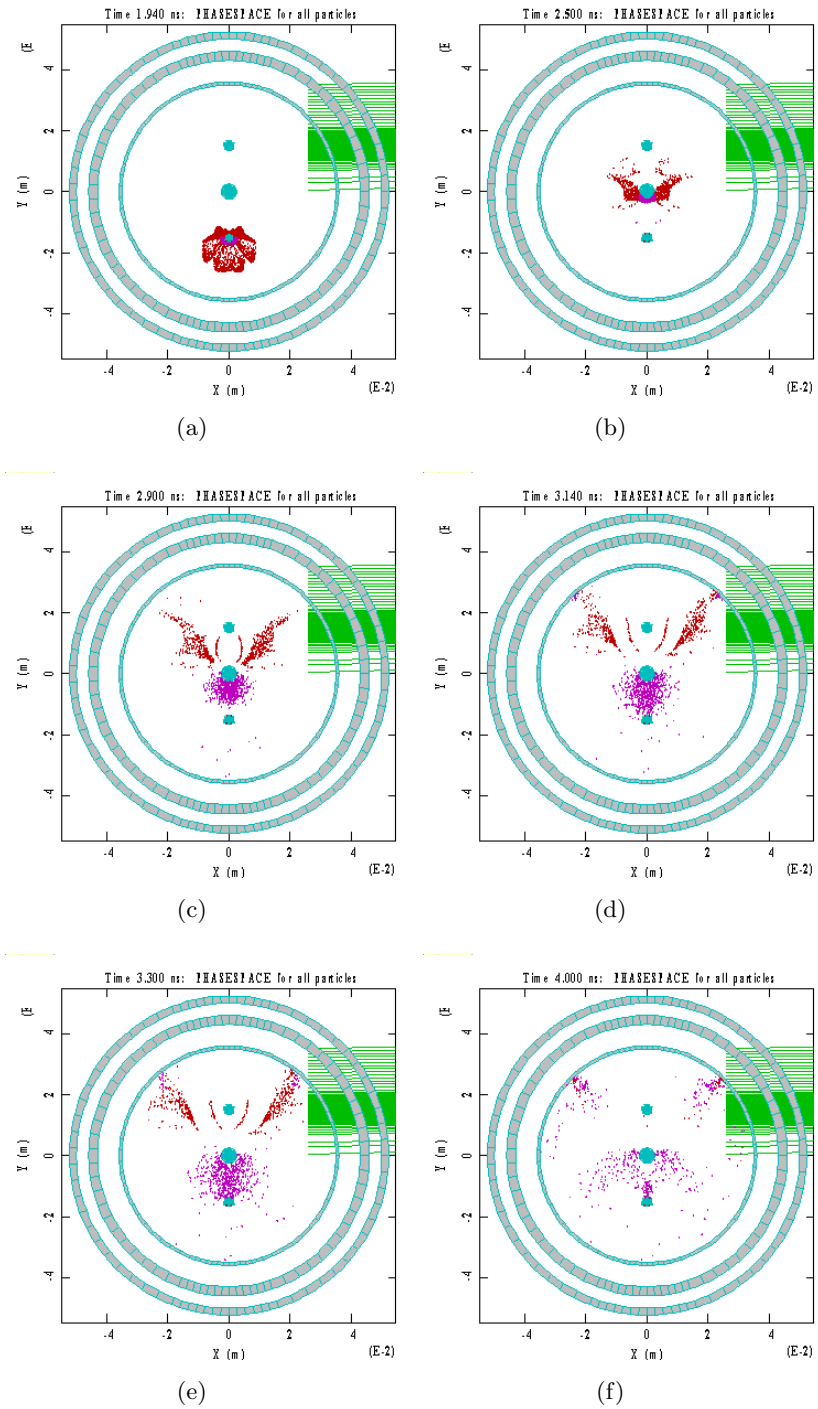

(a) (b) (c) (d) (e) (f)

Figure 4.14: Snap shots of electron clouds (RF power: 4MW; Phase of RF field while primary electrons are released: 0.5π; Glass dome: $\epsilon_r = 4$; Red colour represents primary electrons; Purple colour represents secondary electrons.) (a) t= 1.940ns (b) t=2.500ns (c) t=2.900ns (d) t= 3.140ns (e) t=3.300ns (f) t=4.000ns

condensed when the ceramic dome is used than in the case of the glass dome. If this form of electron bombardment is allowed to continue, it is quite likely to result in multipactor effect and thus the melting of the metal rods.

According to the analysis above, the most likely reason for the melting is multipacting inside the structure. The Multipactor effect is a complicated physical phenomenon. The simulation conducted here is only a preliminary study.

4.2 Cold Test Modelling of the Anode System

4.2.1 Introduction

The chosen magnetron (e2v type MG5193) is a wire echelon strapped, 'slot and hole' magnetron, as shown in figures 4.15(a) and 4.15(b). There are strap breaks on each end of the anode. Four end slots are introduced to compensate the field distortion caused by the strap breaks, as shown in figure 4.15(b). The theory of the strapping system has been discussed in Chapter 2. In this design, the inductance of the oscillator resides mainly in the circular hole, and the capacitance mainly between the parallel walls of the slot. DC voltage is applied through the coaxial input waveguide. RF power is coupled out by two coaxial wires through the two output ports on the circular wall of the anode, which are then connected to the matched output system, which has been investigated in the previous section.

For this S band magnetron, very condensed mesh has been used to simulate the hole and slot structure, and the wire stapping system, which results in a large number of cells (1,468,320 cells). With our current computer resources, the hot test modelling, which involves the interaction between the electron and the RF field, requires a prohibitively long simulation time. So only the cold test modelling has been carried out for this particular S band tube. In the cold test modelling, the oscillation spectrum, the pattern of specific modes and the Q values of various modes can be obtained. The cold test

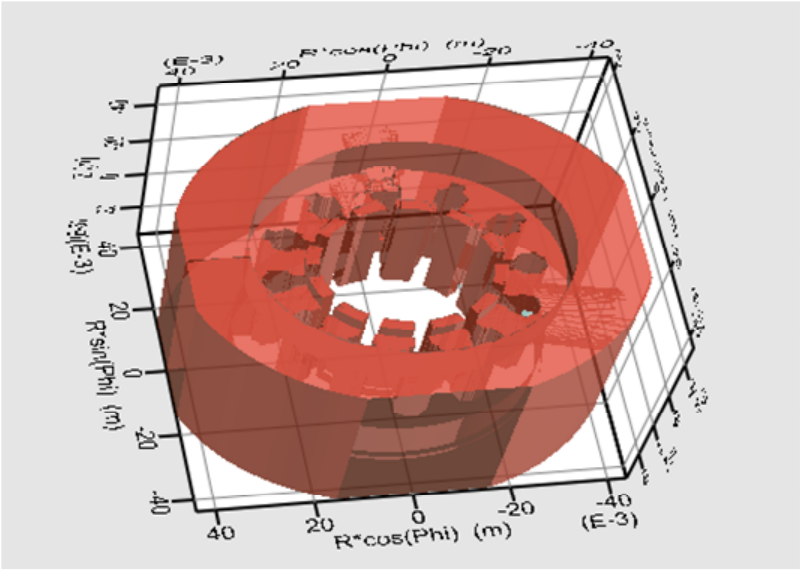

(a)

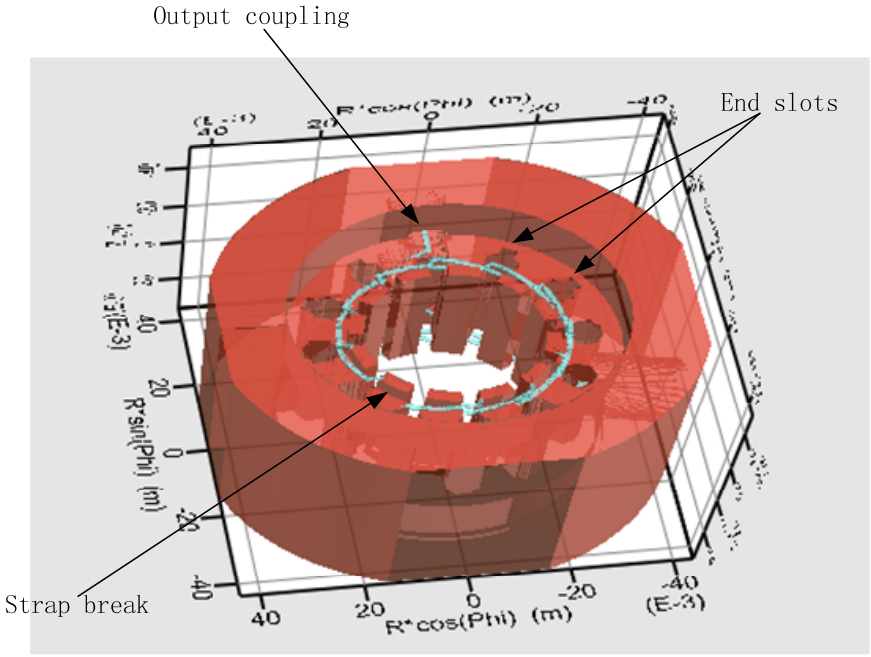

(b)

Figure 4.15: 3D geometry of the anode system of MG5193. (a). The bare anode with the wire strapping system removed. (b). The standard anode including strapping.

modelling is a very useful way to test the basic operation parameters of a magnetron and thus to validate the computer model.

4.2.2 Cold test modelling techniques

The simulation techniques used in the cold test modelling are the 'eigenmode solver' and the 'cold test response' methods. The eigenmode algorithm applies an operator to a given field pattern which grows eigenmodes in a defined frequency range [5]. In general the accuracy of the eigenmode simulations depends on the scanning windows being defined, the operator iteration times and the mesh size of the computer model. In this chapter, the eigenmode simulations are carried out with default iteration setup. It usually takes no more than one hour (depending on the geometry) for one run. So, eigenmode simulations are very quick for searching and predicting the existence of possible modes.

The cold test response technique excites the system with a broad band signal and then lets the signal ring down in a system with output coupling. The mode spectrum can be obtained after a fast Fourier transform (FFT) of the response signal. The resolution of the spectrum is inversely proportional to the simulated time window of the evolving signal. For this S band magnetron, a 40ns' time window requires more than 30hs CPU time, giving the spectrum resolution of 20MHz, which is accurate enough since the system operates around 3GHz and the frequency difference between π and $\pi - 1$ modes is more than 100MHz.

There is a 3% frequency shift between the simulation results of the two techniques. Basically three reasons account for this discrepancy. One is that the geometries are different in these two simulations. Eigenmode simulation requires an all-sealed geometry, while the cold test response simulation requires an open geometry for output coupling. The second reason is that in eigenmode simulation the scanning window, determined by the numerical algorithm of MAGIC, is always broader than the frequency difference between two neighboring modes. This may introduce inaccuracy. The third reason is that in eigenmode simulation, the iteration times also affect the mode accuracy.

It is realised that in order to obtain the right spectrum of MG5193 anode, the geometry of the bare anode model (i.e. without strapping and end slots) should be set up first

of all. With the bare anode model, efforts have been made to optimise the slot geometry. Then, complete computer model with straps has been set up. The computer model has been further improved by including the 'tuner' geometry. The effect of the 'tuner' is to introduce RF asymmetry and change the polarisations of all the degenerate modes, thus splitting and suppressing them. Cold test simulations have been carried out and have shown a close agreement with the experimental results.

4.2.3 Investigation of the bare anode

The function of the strapping system is to bring down and separate the oscillating modes. It is realised that in order to obtain the right spectrum for the MG5193 anode, the spectrum of the bare anode without the strapping and the end slots must be obtained first. Accordingly eigenmode simulations have been carried out while the straps and output coupling wires have been removed and the four end slots at the end of the cavity holes excluded. Figure 4.15(a) shows the 3D structure of the bare anode.

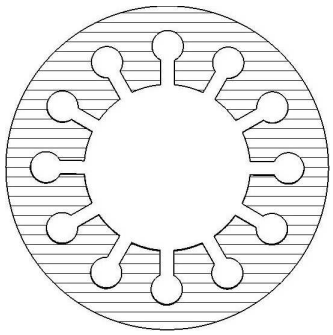

Figure 4.16: Cross section view of the bare anode of MG5193, the slots are parallel.

In the actual tube, the sides of the slots are parallel as shown in Figure 4.16; however in the computer model, due to the limitation of the polar coordinate system, they are slightly tapering, in order to avoid a staircase effect. Two different slot geometries have been investigated.

Firstly the simulations have been carried out with the width of the slot being equal to the real value in the middle length of the slot 4.17(a). The results are presented in

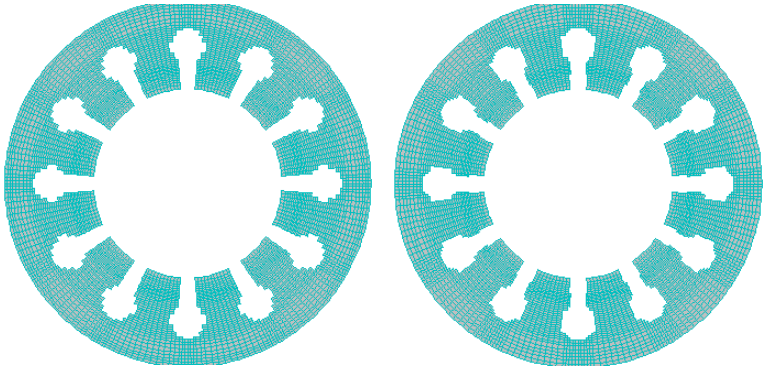

(a) (b)

Figure 4.17: Two different computer models of tapering anode slots. (a) Slot geometry 1: the width of the slot is equal to the real value in the middle length of the slot. (b) Slot geometry 2: the width of the slot is equal to the real dimension at their ends near the cathode.

Table 4-B as slot geometry 1. With this geometry, the computed oscillation frequencies of both π and $\pi - 1$ modes are lower than the measured results. Since the slots act as capacitors in the oscillation circuit, this approximation to the shape of the slots can introduce capacitance errors in the equivalent circuit, thus shift the resonating frequencies. In the second geometry being investigated the width of the slot is equal to their real dimension near the cathode, see Figure 4.17(b). The computer model of the second slot geometry consists of two tapering segments connected together, showing a small staircase between the two segments. With this modified geometry, the π and $\pi - 1$ mode frequencies obtained by simulation moved much closer to the expected values, as shown in Table 4-B, slot geometry 2. Figures 4.18(a) and 4.18(b) show the electric field distribution of the π and $\pi - 1$ modes, using slot geometry 2 and obtained with the help of MAGIC eigenmode solver. Investigations of different slot geometries demonstrate that the width of the slots near the cathode is more important in determining the equivalent capacitance in the resonant circuit.

Exciting the anode system with a broad band signal, the mode spectrum can be also obtained, see Figure 4.19. Compared with e2v measurements (see Table 4-C), the computed frequencies are close to the measured results; in addition to π and $\pi - 1$ modes,

Table 4-B: Frequency comparison between simulation results and experimental results of the bare anode with different computer slot geometries

Modes	MAGIC eigenmode solver (GHz)	e2v (GHz)
π	4.13 (Slot geometry 1) 4.19 (Slot geometry 2)	4.192
$\pi - 1$	4.11 (Slot geometry 1) 4.15 (Slot geometry 2)	4.141

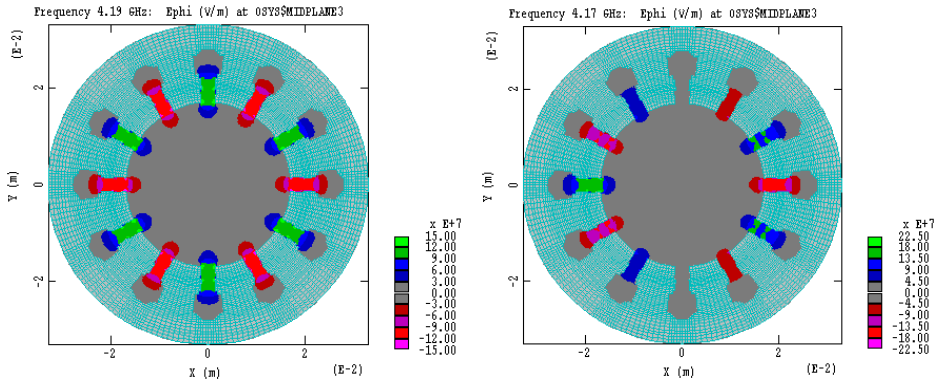

(a) (b)

Figure 4.18: The electric field distribution in π and $\pi - 1$ modes using slot geometry 2

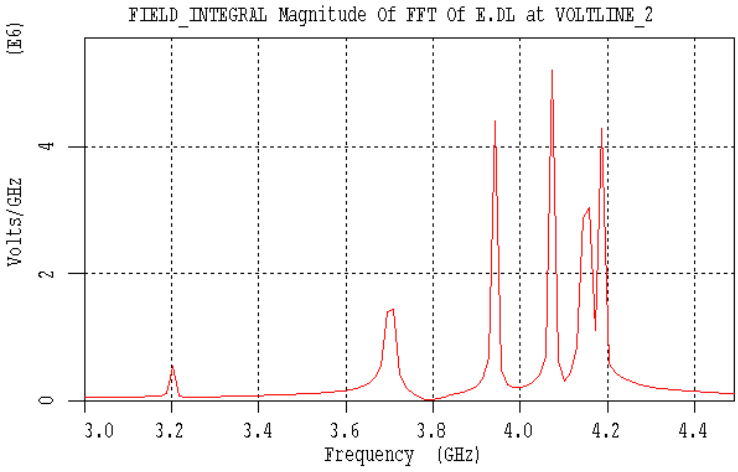

Figure 4.19: The oscillation spectrum of the bare anode with slot geometry 2.

the presence of other higher order modes can also be revealed.

Table 4-C: Comparison of the computed and measured spectrum of oscillations in a bare anode.

Modes	MAGIC (GHz)	e2v (GHz)
1	4.188 (π)	4.192 (π)
2	4.153 ($\pi-1$)	4.141 ($\pi-1$)
3	4.072	4.104 (possible $\pi-2$
4	3.942	4.015 (possible $\pi-3$)
5	3.703	3.891 (possible $\pi-4$)
6		3.855 (possible $\pi-5$)

4.2.4 Investigation of the standard anode

Putting back the wire strapping system and the four end slots, cold test simulations have been conducted and compared with the measurements. The geometry of the standard anode is shown in Figure 4.15(b).

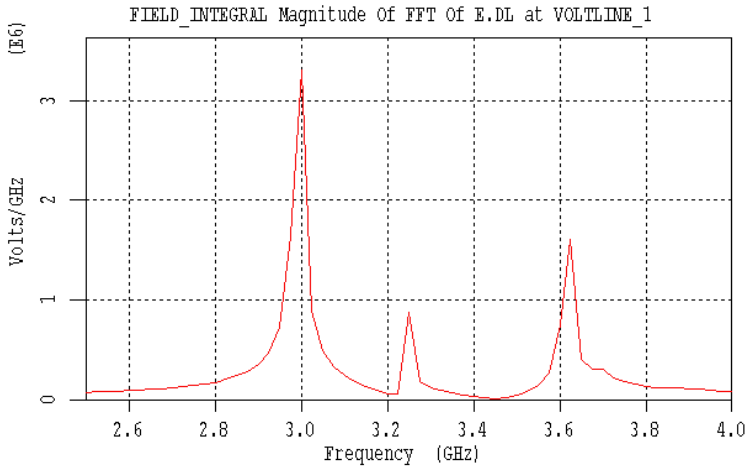

Figure 4.20: A computed oscillation spectrum of the standard anode including the wire strapping system and the end slots

Figure 4.20 shows the computed mode spectrum of a standard anode. The π mode oscillation is obtained at 2.998GHz and $\pi-1$ mode at 3.251GHz. Table 4-D compares the experimental and simulation results. The simulation results agree with the experimental results very well, except only one $\pi-1$ mode frequency as obtained from computer simulation. This is because the computer model doesn't include the 'tuner', which is used in the real magnetron to split the degenerate modes. The effects of the 'tuner' will be investigated in the next section.

Table 4-D: Oscillation spectrum comparison between simulation and experimental results (standard anode)

modes	MAGIC (GHz)	e2v (GHz)
π	2.998	3.000
$\pi-1$	3.251	3.150/3.250

4.2.5 Investigation of the 'tuner'

The 'tuner' is a segment of coaxial waveguide penetrating into the anode from the radial direction as shown in Figure 4.21. The adjacent two cavity holes are then connected together. As discussed in Chapter 2, magnetron can be analysed by an equivalent circuit theory. The principle of the 'tuner' is that it introduces variable capacitance into the anode system. The RF distortion produced by the tuner changes the polarisation of all the degenerate modes, thus splitting them. By pushing the tuner in and out, the capacitance of the circuit can be changed, resulting in the change of the resonating frequencies of the circuit. The main effect of the tuner is to split the polarisation of the $\pi-1$ modes, which are the strongest competing modes with the π mode. In experiments, by adjusting the tuner, the external Q factor of one of the $\pi-1$ modes is usually tuned to around 300 and the other to around 1000. This arrangement can cause the over coupling of the low Q $\pi-1$ mode to the output and at the same time suppress the oscillation start-up of the high Q $\pi-1$ mode, thus help π mode oscillations to dominate; this improves the operation efficiency and stability of the magnetron. In computer modelling, the frequency and polarization tuning function is realised by altering the 'tuner gap' as shown in Figure 4.21.

Table 4-E: Comparison of simulation and experimental spectra (MG5193)

Modes	MAGIC (GHz)	e2v (GHz)
1	2.986 (π)	3.000 (π)
2	3.132 ($\pi-1$, lower)	3.160 ($\pi-1$, lower)
3	3.266 ($\pi-1$, upper)	3.220 ($\pi-1$, upper)
4	3.318	3.347 (π')
5	3.350	
6	3.653	
7	3.785	

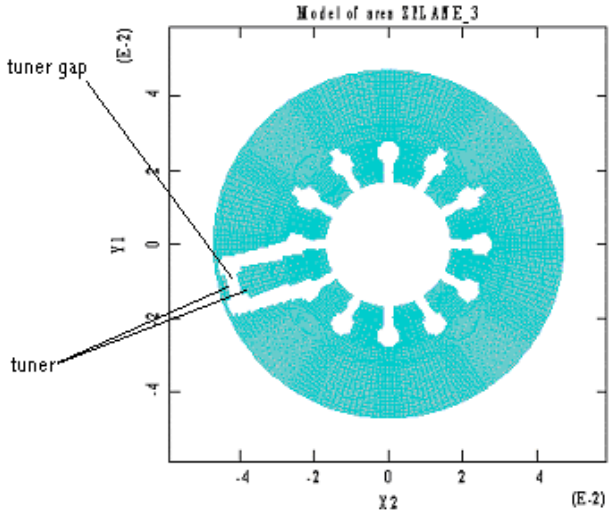

Figure 4.21: The geometry of the 'tuner'

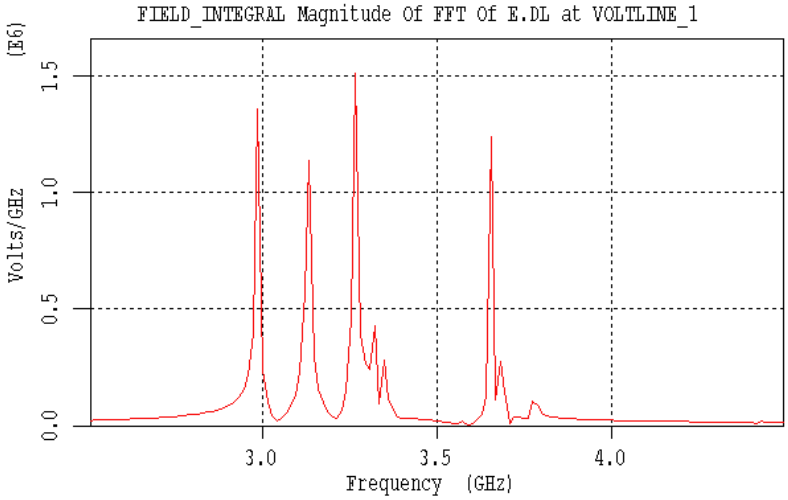

Figure 4.22: Spectrum of oscillations when the tuner is included

The cold test response simulation has been carried out. All the degenerate modes ($\pi - 1$ and other higher order modes) and their splitting have been observed. Changing the tuner gap, it is found that the different dimensions of the tuner gap can not only split and tune the degenerate modes but also change the π mode frequency substantially. Table 4-E compares the simulation results and the experimental results. Very good agreement with the experiments has been obtained after including the tuner inside the cavity. Figure 4.22 shows the cold test oscillation spectrum.

4.3 Summary

Various possible causes for the melting of the coupling rods inside the output system of the S-band magnetron have been studied by using MAGIC. The preliminary study has indicated that the melting is most likely caused by multipacting between the coupling rod and the central rod supporting the dipole.

The anode system of the magnetron has been analysed and simulated using MAGIC 3D code. The computer model has been built and validated. Cold test simulation results agree very well with the experimental results. It has been demonstrated that the 'tuner' plays an important role in the mode competition.

The modelling work in this chapter shows that careful approximation has to be made in order to get adequate accuracy and practical computation times. It also shows that MAGIC is a powerful software tool, which can model the fine details of magnetron geometry and operation, such as wire strapping, hole and slot structures and tuner. Therefore MAGIC has been proved to be a reliable tool to carry out further modelling work on an X band magnetron, as discussed in Chapter 5.

References

[1] R.A.Kishek and Y.Y.Lau., "Multipactor discharge on metals and dielectrics: Historical review and recent theories," *Phys. Plasma*, vol. 5, no. 5, p. 2120, 1998.

[2] Valfells, A. Verboncoeur, J.P, and Y.Y.Lau, "Space-charge effects on multipactor on a dielectric," *Plasma Science, IEEE Transactions*, vol. 28, no. 3, p. 529, 2000.

[3] L.-K. Ang, Y.Y.Lau, R.A.Kishek, and R.M.Gilgenbach, "Power deposited on a dielectric by multipactor," *Plasma Science, IEEE Transactions*, vol. 26, no. 3, pp. 290–295, June 1998.

[4] R.A.Kishek and Y.Y.Lau, "Multipactor discharge on a dielectric," in *Physics Review Letter*, vol. 80, 1998, p. 193.

[5] L.Ludeking, Ed., *Manual of MAGIC Tool Suite.* Mission Research Corporation, 2002.

Chapter 5

3D Modelling of an X band Magnetron

5.1 Introduction

As mentioned in chapter 4, with our current computer resources, the hot test modelling of the S band magnetron, which has a very complicated structure, proved to be unrealistic. Therefore a magnetron with a structure that more easily fits with the symmetry of the polar coordinate system has been chosen. An X band magnetron, which has eighteen vanes, sector shaped cavity and ring straps (e2v technologies type MG5241), has therefore been selected for our investigations (see Figure 5.1). Compared with the S band (MG5193) magnetron, the X band magnetron with its vanes and ring straps better fitted the polar coordinate system and required fewer cells for modelling. The total number of cells used for modelling the S band magnetron (MG5193) was 1,468,320, while the equivalent number of cells for the X band magnetron (MG5241) is only 586,950, 40% of the previous figure. This reduces the simulation time for the X band magnetron dramatically. A typical hot test simulation of EM run time 40ns, which is the time required for the X band magnetron model to settle down to stable oscillations, can be completed

in 40 hours on a 2.5GHz CPU computer.

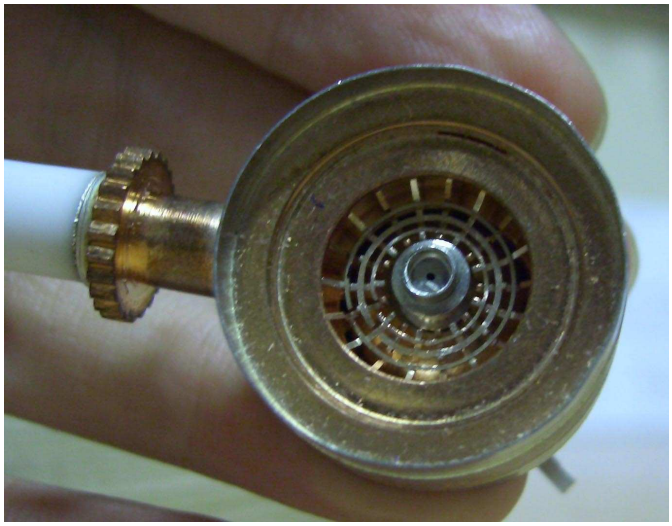

Figure 5.1: Image of an X band magnetron (e2v type MG5241)

In this Chapter, a complete set of modelling techniques and their use will be described as applied to the X band magnetron. First, different computer models have been evaluated to choose the most suitable one for further hot test modelling. Several different methods have been developed to measure the external Q value of the magnetron, to achieve consistent results. Based on the validated model of the X band magnetron, hot test simulations have been carried out with different cathode emission schemes and various input parameters. In general, the computed performance agrees well with the experimental performance, but there is an approximate 10% discrepancy between the computed and measured values for the overall efficiency. Several possible reasons for this discrepancy have been investigated, including the output coupling circuit, the end hats emission, the copper surface loss and the RRV (rate of rise of anode voltage). At this stage of the computer modelling work, cathode secondary emission has not been included.

The cathode secondary emission in magnetrons is a very complicated process. How it affects the magnetron operation is not fully understood. In the MAGIC modelling, numerical instability involving cathode secondary emission is always a problem. There-

fore in the thesis, the direct simulating of cathode secondary emission is not carried out. Instead, through investigation of the back bombardment energy distribution and simulating the effects of the secondary emission by primary emission with an equivalent energy distribution, an important effect of the secondary emission has been revealed. This work will be presented separately in Chapter 7.

5.2 Optimization of the Computer Model

The X band magnetron has a long established production history enabling a ready comparison of computed and measured results, so that the model can be meaningfully benchmarked. Table 5-A presents the dimensions of the tube and its typical performance. Ideally the magnetic field should be uniformly applied along the axial length of the magnetron. But in reality, due to the effects of the pole pieces, which are located outside the two ends of the cathode, the magnetic flux is non-uniform. In this section, the main objective is to optimise the computer model; for simplicity, a uniform rather than real magnetic field distribution is used in the computer modelling. The effects of the real magnetic field distribution on magnetron performance will be investigated separately in section 5.3. In Chapter 6, further investigations will be carried out on the important effects of the real magnetic field distribution on the cathode emission and back bombardment.

The vanes in this X-band magnetron are parallel in shape. However, this presents a problem since computer modelling is carried out in terms of polar coordinates, so strict adherence to the physical geometry would require a fine mesh structure leading to long computed runs. One important aspect was to fit the model to the symmetry imposed by the code, in order to maximise the computing efficiency. Three different vane models have been investigated: 'parallel' vanes (in practice step-like parallel due to the finite size of the cells used in computing), thin tapering vanes, the model and the real vanes having the same thickness half way down their length and thick tapering vanes, the model and

real vanes having the same thickness at the end facing the cathode. The thin tapering vane model had been given up because the very thin vane tips can alter the electric field near the vane tips and thus destroy accurate representation of the magnetrons interaction process.

Table 5-A: e2v type MG5241 magnetron: dimensions and typical performance

Cathode radius (mm)	1.90
Anode radius (mm)	2.82
Frequency bore radius (mm)	8.20
Width of vanes (mm)	0.40
Number of vanes	18
Pi mode frequency (GHz)	9.410±0.030
Q_{ext} of π mode	236
Unknown mode (GHz)	10.406
π-1 lower (GHz)	10.137
Q_{ext} of π-1 lower	220
π-1 upper (GHz)	11.063
Q_{ext} of π-1 upper	323
Maximum magnetic field (T)	0.418
Anode voltage (kV)	6.10
Anode current (A)	5.0
Output power (kW)	12.2
Overall efficiency	40.0%

5.2.1 The parallel vane model

The so called 'parallel' vane model is actually step like parallel due to the polar coordinate system and the finite size of the mesh. Both fine mesh (360 cells in azimuthal direction) and coarse mesh (180 cells in azimuthal direction) have been tried on order to examine the effect of the staircase. Figure 5.2.1 shows the cross section view of the 'parallel' vane model in both fine mesh and coarse mesh.

A broadband frequency response method has been used to obtain the system oscillation spectrum. With this technique, a broad-band signal, shown in Figure 5.3(a), is applied using a probe located near the output port. Several oscillation frequencies have been excited inside the magnetron. The oscillation spectrums for the two models are

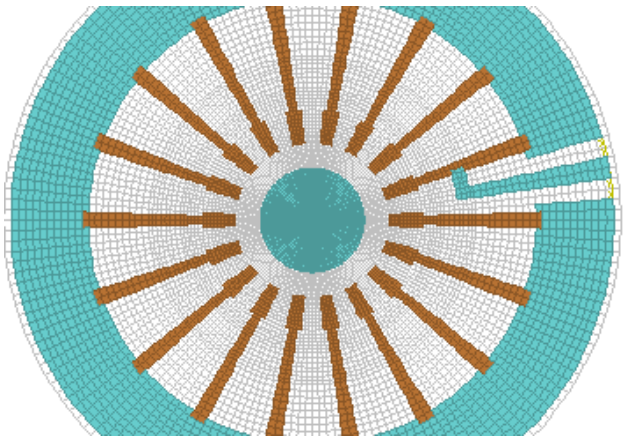

(a)

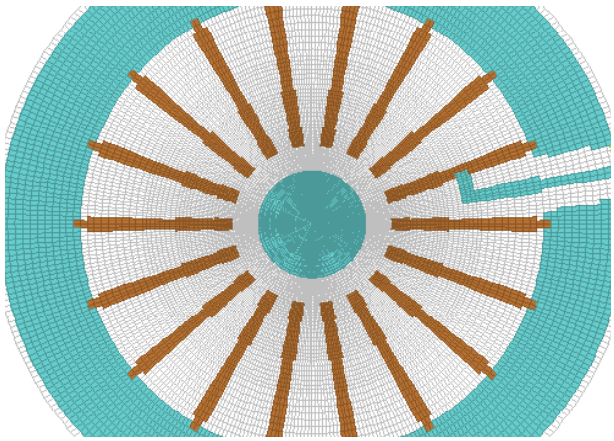

(b)

Figure 5.2: Cross section view of the parallel sided vane models with (a) Coarse mesh (180 cells in azimuthal direction) (b) Fine mesh (360 cells in azimuthal direction)

shown in Figure 5.3(b). In both cases four main oscillation peaks could be observed (see Table 5-A): one π mode frequency, two $\pi - 1$ frequencies and one unknown mode frequency.

The simulation results show that there are frequency peaks of higher order modes around 12GHz and 13GHz, but those frequencies have a minor effect on the magnetron operation since they are far away from the π mode. Different mesh densities cause a discrepancy in the spectra. In the fine mesh model the π mode is excited at 9.294GHz; in the coarse mesh model the π mode is excited at 9.360GHz, both are lower than the measured 9.410GHz. This is because in the computer model the space between

two adjacent vanes, which are step like parallel, is smaller than that of the real tube, correspondingly the anode capacitance is higher, thus the lower π mode frequency. In the fine mesh model, this space is even smaller than that of the coarse mesh model, which causes its even lower π mode frequency than that of the coarse mesh model.

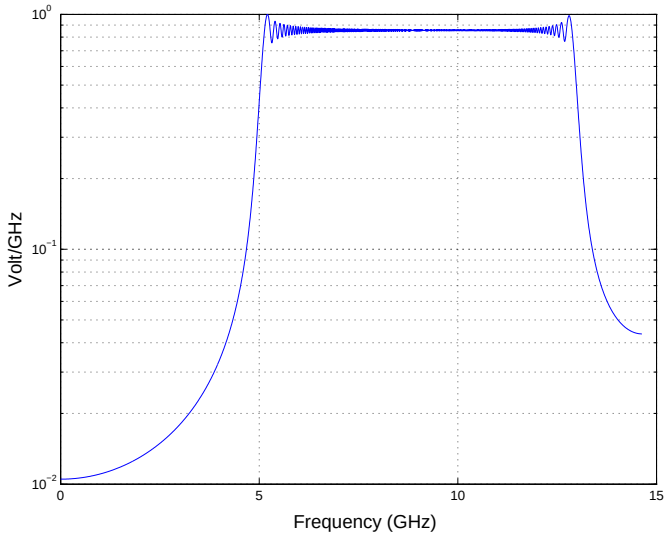

(a)

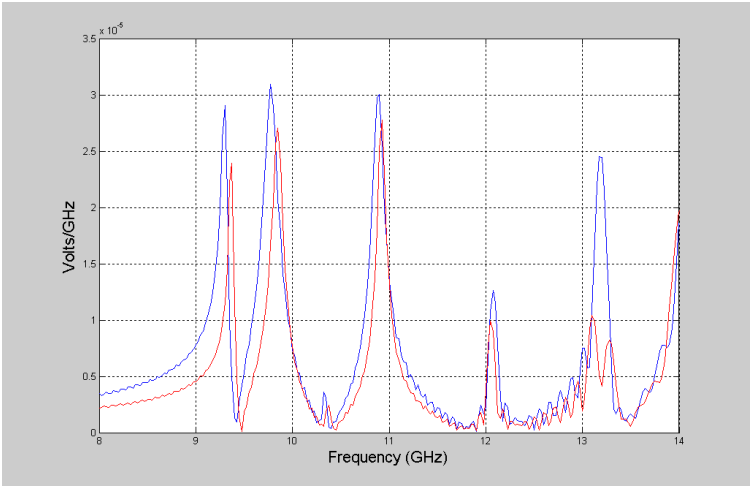

(b)

Figure 5.3: (a) Spectrum of the broad band signal. (b) Spectrum of the responding signal. Blue curve represents fine mesh model (oscillation peaks at: 9.294GHz, 9.776GHz, 10.325GHz and 10.889GHz); Red curve represents coarse mesh model (oscillation peaks at: 9.360GHz, 9.840GHz, 10.380GHz and 10.920GHz).

Hot test simulations have also been carried out with the two models respectively and

π mode oscillations around 9.28GHz have been observed. It is reasonable for the hot test π mode frequencies to be different from their cold test values, since in hot test the space charge inductance also affects the oscillation frequency. Table 5-B presents the results of the two hot test simulations and their operation conditions. Comparing with the experimental results, the simulated values of the anode current are low and the overall efficiencies are quite high, 58.2% and 54.1% for the fine mesh and coarse mesh models respectively, as against the experimental value of 45%. For the sake of simplicity copper surface losses have not been included in the simulation processes. Instead, the overall efficiency is calculated by including overall circuit efficiency of 85%, the figure being derived from measurements at e2v. Calculation of circuit efficiency η_{cold} is described in section 5.7 in terms of Q_0, Q_{ext} and Q_{load}. The hot test Q_{ext} are 145 for the fine mesh and 206 for the coarse mesh, both lower than the experimental 236.

Table 5-B: Hot test simulation results of the 'parallel' sided vane model

Cathode emission model: space-charge-limited		
Frequency bore radius: 8.2mm		
Effective anode voltage: 5.75kV		
Magnetic field: 0.405T		
Circuit efficiency: 85%		
Azimuthal mesh density (degree/cell)	360	180
π mode frequency (GHz)	9.287	9.284
Anode current (Amps)	3.3	4.1
System RF energy (Joule)	32.2	53.2
hot test $Q_{ext} = 2\pi f_0 \frac{W}{P_out}$	145	206
Output power (kW)	13.0	15.0
Overall efficiency	58.2%	54.1%

Generally speaking the fine mesh and coarse mesh models give consistent results. The overall efficiencies are 10% higher than the experimental results. Considering the Q_{ext} and the overall efficiency, the coarse mesh model is more close to the experimental results. This indicates that improving the mesh density of the computer model does not necessarily cause the calculated performance getting closer to the measured performance. The fine mesh structure can reduce the errors caused by staircase, but it may also cause more round-off errors. The azimuthal mesh density of the coarse mesh model (2degrees/cell)

is therefore quite sufficient. The computed π mode frequencies of both models are about 1% lower than the measured π mode frequency 9.410GHz. Since in computer modelling, the π mode frequency can be tuned easily by adjusting the frequency bore radius (back of the cavity) without affecting the magnetron performance significantly, therefore in this section, we do not bother to correct the frequency discrepancy, but concentrate on the test of the different vane models. A fine frequency tuning will be carried out in later work.

5.2.2 The thick tapering vane model

The geometry of the 'thick' tapering vane model, with its vane tips having the same thickness as the real model, is shown in Figure 5.4(a). Also in Figure 5.4(a) together with Figure 5.4(b), the transverse and axial cross-sections of the model are presented, showing the cathode and the anode together with the relevant parts of the input and output circuit. Because of the thick vane model, the space between two adjacent vanes is actually smaller than the real model, which will change the oscillation frequency. An increase in the diameter of the frequency bore had been made to compensate for this area loss between adjacent vanes thus tune the resonant frequency close to the measured value. When tuning the radius of the frequency bore to 8.68mm, π mode oscillations have been observed at 9.472GHz; $\pi - 1$ modes at 9.908GHz and 10.926GHz; unknown mode frequency at 10.350GHz. Figure 5.5 shows the oscillation spectrum obtained from the broad band frequency response. These results are very close to the experimental oscillation frequencies presented in Table 5-A, which are π mode at 9.410 ± 0.030GHz, $\pi - 1$ modes at 10.137GHz and 11.063GHz, unknown mode at 10.406GHz.

Hot test simulation with this model has been carried out and a very fine π mode oscillation has been obtained. In Figure 5.4(a) and 5.4(b), the snapshots of electron cloud of π mode oscillation are also shown. The important role of the cathode end hats in confining the electron cloud can now be seen quite clearly. Here the end hats are the two metal edges on the two ends of the cathode, see Figure 5.4(b). The operating

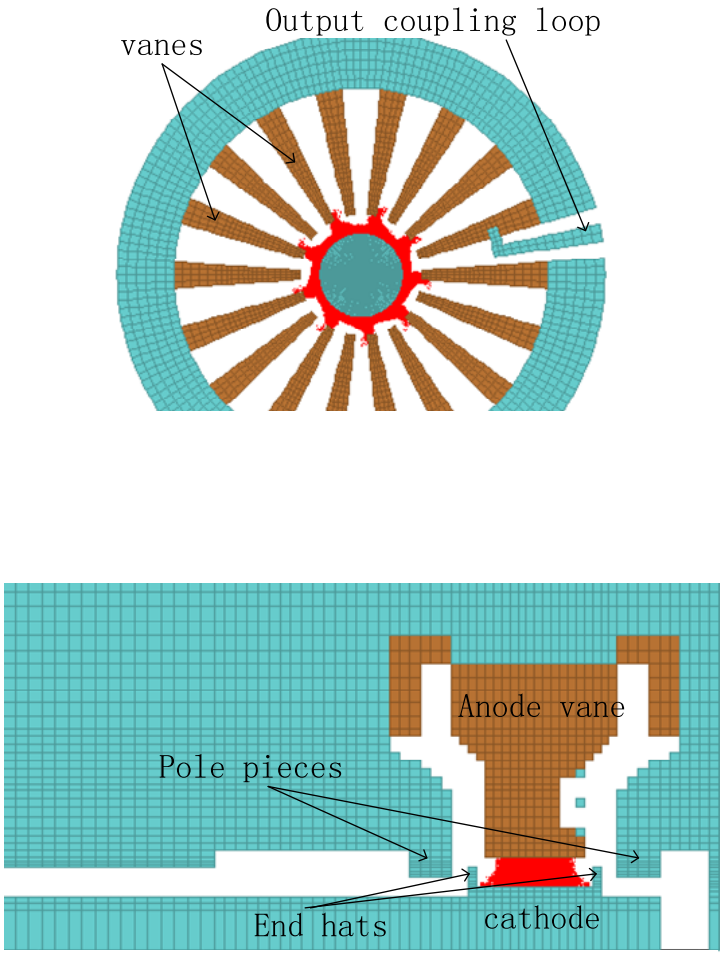

(b)

Figure 5.4: The geometry of the thick tapering vane model and the electron cloud of a π mode (a)Transverse cross section (b)Axial cross section

conditions of the magnetron and the computed performance are shown in Table 5-C. Comparing with the experimental results, this thick tapering vane model still yields a very high overall efficiency of 55.6%. In table 5-C, the Q_{ext} of the π mode has been calculated in two ways, one is from the cold test energy decay rate and the other is from the hot test simulation using the definition formula of external Q [1]. The two methods have given consistent results, which are close to the experimental value. In computer modelling, several methods have been developed to measure the Q_{ext}, which will be discussed in detail in the next section.

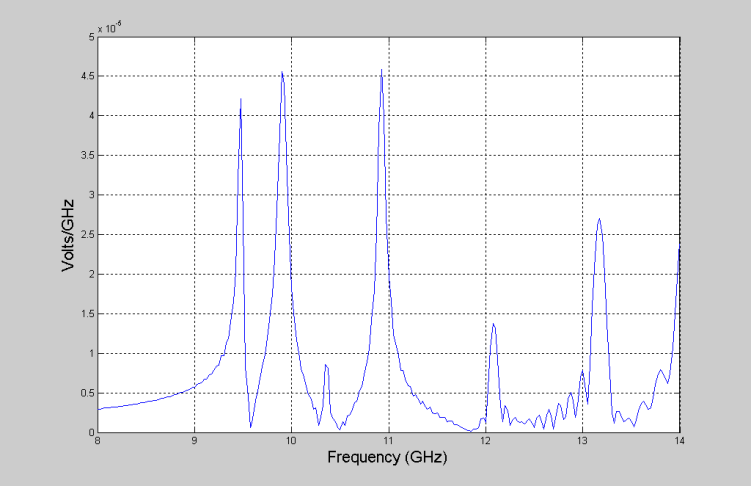

Figure 5.5: Oscillation spectrum of the 'thick' tapering vane model by broad band frequency response method (oscillation peaks at: 9.472GHz, 9.908GHz, 10.350GHz and 10.926GHz)

Table 5-C: Hot test simulation of the 'thick' tapering vane model

Cathode emission model	space-charge-limited
Frequency bore radius (mm)	8.68
Effective anode voltage (kV)	5.75
Magnetic field (T)	0.405
Circuit efficiency	85%
Azimuthal mesh density (degree/cell)	180
Cold test Q_{ext}	260
Oscillation frequency (GHz)	9.461
Vane voltage (kV)	5.2
Anode current (A)	3.8
hot test $Q_{ext} = 2\pi f_0 \frac{W}{P_{out}}$	244
Output power (kW)	14.3
overall efficiency	55.6%

The transient state of the magnetron before it starts oscillating in the π mode (thick vane model) is shown in Figures 5.6 and 5.7. Figure 5.6(a) shows the anode voltage evolution. It can be seen that once the oscillations start, the effective anode voltage will drop a bit because of the change in magnetron impedance. Therefore in the diagram, the effective anode voltage is 5.75kV when the system is in stable π mode oscillation, which is a little bit lower than the applied voltage of 5.8kV. Figure 5.6(b) shows the anode current evolution, which starts building up after 6ns. Figure 5.7(a) shows the RF voltage between

two adjacent anode vanes. After 6ns, oscillations settle down smoothly into the π mode. Figure 5.7(b) shows the FFT of the RF voltage between the adjacent vanes, where the spectrum is a very clean π mode. The evolution of the output power (Figure 5.6(c)) and the total system energy stored in the magnetron (Figure 5.7(c)) present similar behavior, consistent with the evolution process of the vane voltage oscillations and the anode current.

In the above investigations, the space-charge-limited emission model has been applied to the cathode emission for both the parallel vane model and the thick tapering vane model. The magnetic field being used is a uniformly distributed field of 0.405T along the axis of the magnetron. At the beginning of our modelling work, the MAGIC code could not allow for the real magnetic field distribution. After Aug. 2003, MAGIC has been updated to include the real magnetic field distribution, which makes the computer modelling much closer to real life magnetron operation. In this section, since the objective of preliminary modelling is to optimise the computer model, only one set of results is presented for each vane model. Therefore they do not represent a complete range of performance of the magnetron, but it is hoped enough information has been provided for our initial objective.

Concerning the above investigations, the *parallel* vane model and the 'thick' tapering vane model produced consistent results, but they both exhibit higher overall efficiency. This discrepancy in efficiency will be investigated in detail in the following sections. The thick tapering vane model has been chosen for further modelling because it best represents the conditions near the vane tip, where the important interaction process takes place. The slight change in the cavity outer radius of this model has little effect on the whole performance. It also avoids the 'stair-case' on the vane structure. Its oscillation spectrum and external Q value of the π mode agree very well with experimental results.

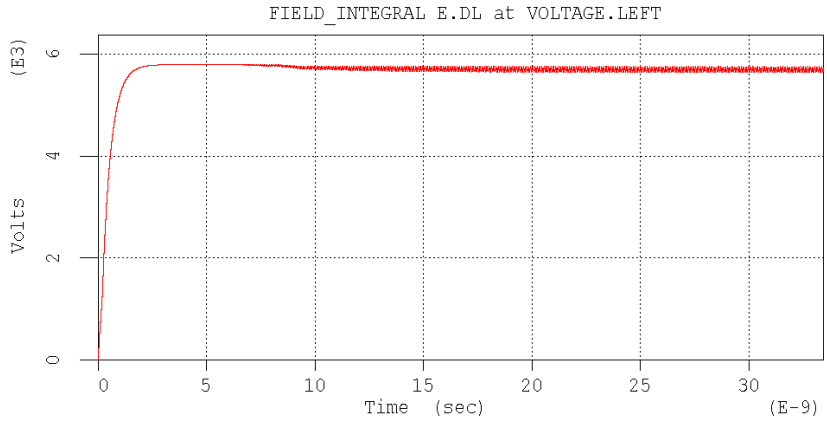

(a)

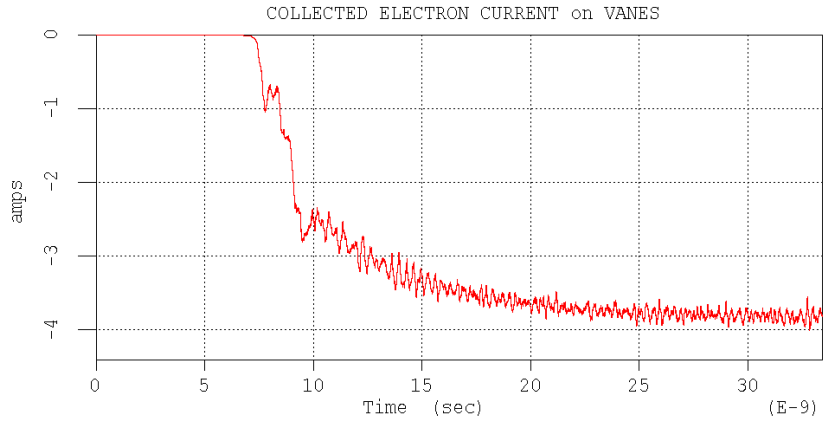

(b)

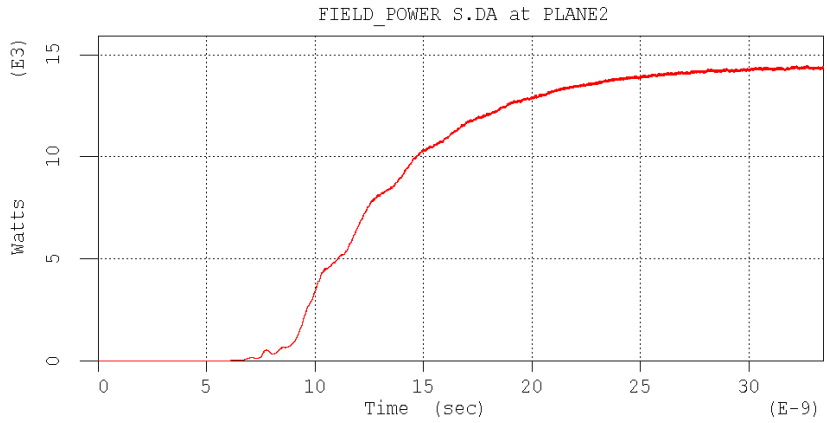

(c)

Figure 5.6: Magnetron transient evolution. (a) The anode DC voltage. (b) The anode current. (c) The output power.

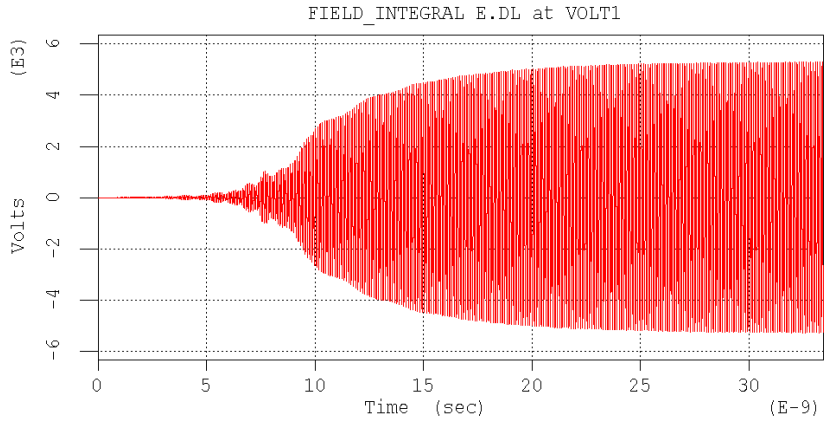

(a)

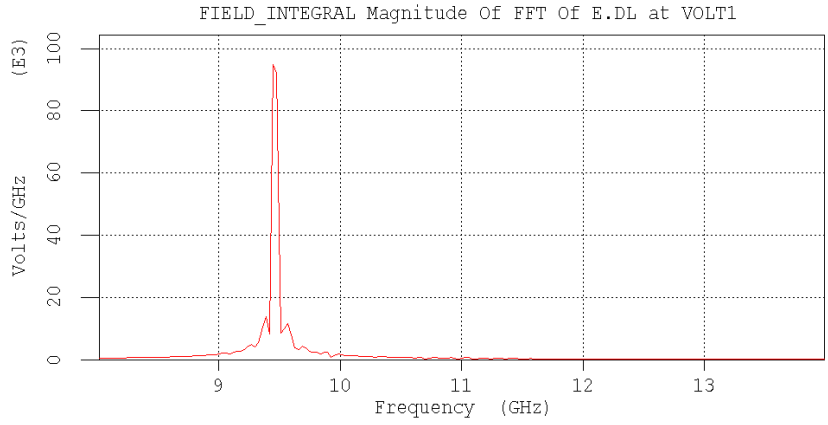

(b)

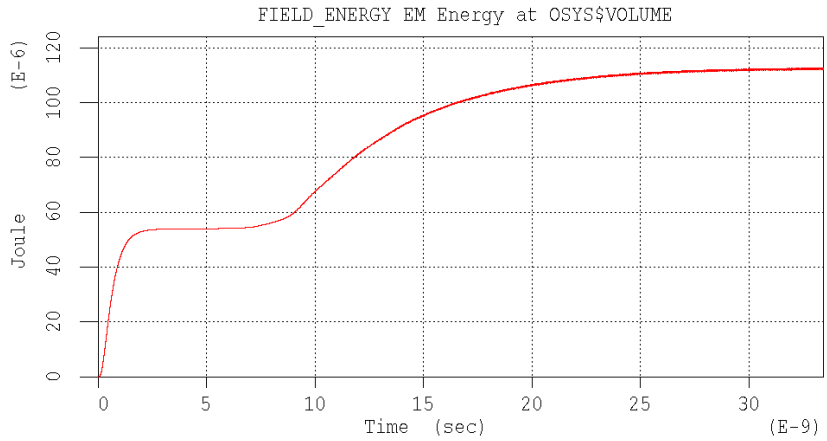

(c)

Figure 5.7: Magnetron transient evolution. (d) The voltage oscillation between adjacent anode vanes. (e) The FFT of the vane voltage oscillation. (f) The total system stored energy evolution. Before 14ns, the energy is only DC energy, which is 54.12e-6J; after 14ns, the total energy, including the DC energy and RF energy, is 106.06e-6J.

5.2.3 Measurement of the external Q value

Two different methods have been developed to measure the magnetron Q_{ext} in computer modelling. First it is calculated from the system's energy decay. With this method, an eigenmode simulation needs to be completed first to obtain the π mode field distribution inside the cavity. By presetting this field distribution inside the cavity and letting the field ring down, the Q_{ext} can be obtained from the system's energy decay rate. Usually when excited in the π mode, the system energy will drop quickly below the half value of the original energy within 10ns. A cold test simulation of 10ns in EM time can be finished in 2 or 3 hours with a 2.5GHz CPU computer. Therefore this method is very quick. Figures 5.8(a) and 5.8(b) show the Ephi distribution of the π mode in the cross and axial sections of the anode, obtained from the eigenmode solver of MAGIC. Figure 5.9(a) illustrates the system energy evolution while excited in the π mode. Here, for the convenience of calculations, the total stored energy is normalized to 1 Joule. Figure 5.9(b) illustrates an instant external Q value of 260.

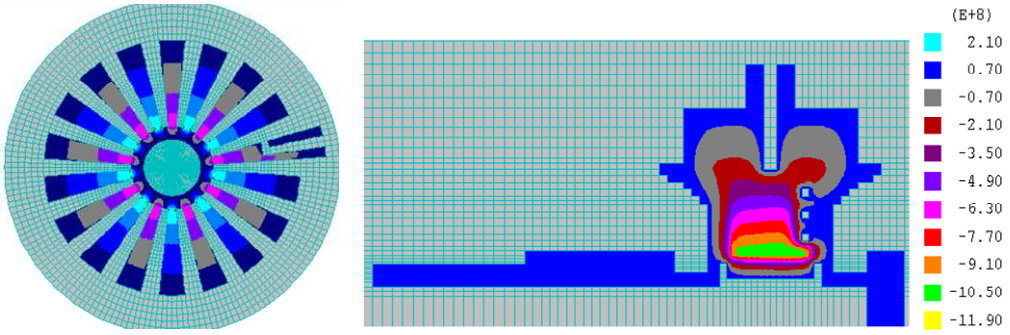

(a) (b)

Figure 5.8: Ephi distribution of π mode in (a) The transverse section of the anode. (b) The axial cross section of the anode

The second method is to use the results obtained from the hot test simulation. The definition of the Q_{ext} is $2\pi f_0 W/P_{out}$ [1]. Where f_0 is the π mode frequency, W is the system stored RF energy, P_{out} is the output power. All these parameters can be obtained from the hot test simulation. In computer modelling, the total system stored energy can be calculated. Before oscillations start, the system's stored energy is mainly the DC

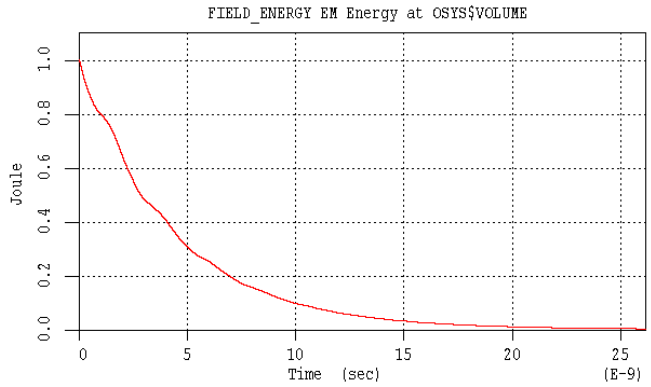

(a)

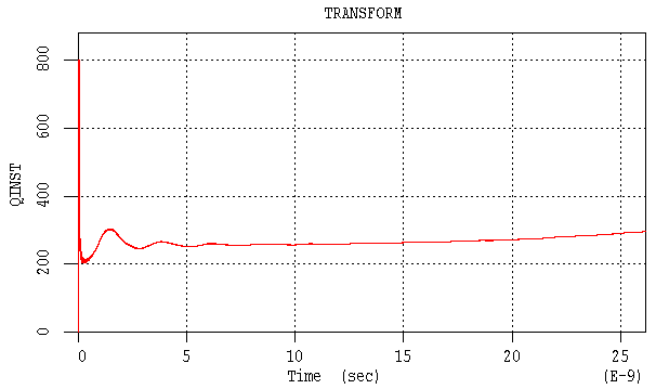

(b)

Figure 5.9: Measure the external Q value from system energy decay rate. (a) The system energy evolution while excited in π mode distribution. (b) The instant external Q of 260.

energy; when the system starts oscillating in the π mode, the stored energy is the sum of both DC and RF energy, as shown in Figure 5.7(c). It can be obtained from this figure that before the oscillations start the DC energy is $54.0e-6J$; while the system is in stable π oscillations, the total energy is $112.6e-6J$. Therefore, the system's stored RF energy while in stable oscillations can be obtained by subtracting the DC energy from the total energy, which is $W_{RF} = 58.6e-6J$. The final output power is 14.3kW and the oscillation frequency of the π mode is 9.461GHz. The Q_{ext} can then be calculated; it is 244 and very close to the cold test measurement. Therefore since the two methods of Q measurement give very close results, the thick tapering vane model has been validated again as the optimum model for further hot test investigations of the X band magnetron.

5.3 Real Magnetic Field Distribution

At the early stage of our modelling work, all calculations were carried out assuming a uniform magnetic field. Later in August 2003, MAGIC was updated to allow for a 3D magnetic field distribution. This enabled the comparison between a uniform and a real magnetic field. Before the discussion of the simulation results, explanation will be given of the difference between the uniform magnetic field and the real magnetic field as obtained from e2v measurements. Figures 5.10 and 5.11 show the two components B_r and B_z of the actual static magnetic field as they vary in the radial and axial directions. The coordinate origin is located on the axis and in the center of the anode block. The magnetic field distribution is symmetric in azimuthal direction, that is, no B_θ component is present. Also the magnetic field distribution is symmetric in the axial or z direction. Thus the magnetic field distribution is 2D in nature. Figures 5.10 and 5.11 represent the magnetic field distribution in one half of the longitudinal cross section of the anode. A spike occurs in both B_r and B_z near the polepieces, which are just outside the interaction space and near the two end hats, see Figure 5.4(b). The anode structure has been described at the beginning of the cold test modelling. Within the interaction space, which is between the anode vanes and the cathode, B_z varies from 0.405T to 0.418T; the B_r component is nearly zero in the centeral region of the cathode, but it has non-negligible values near the end hats. Figure 5.12 illustrates the B_z variation between the cathode and anode in the centeral cross section; the maximum value of B_z in the z=0 plane is given by $B_{max} = 0.418T$. In the following work, the use of the real magnetic field distribution will be indicated by the value of 'B_{max}'.

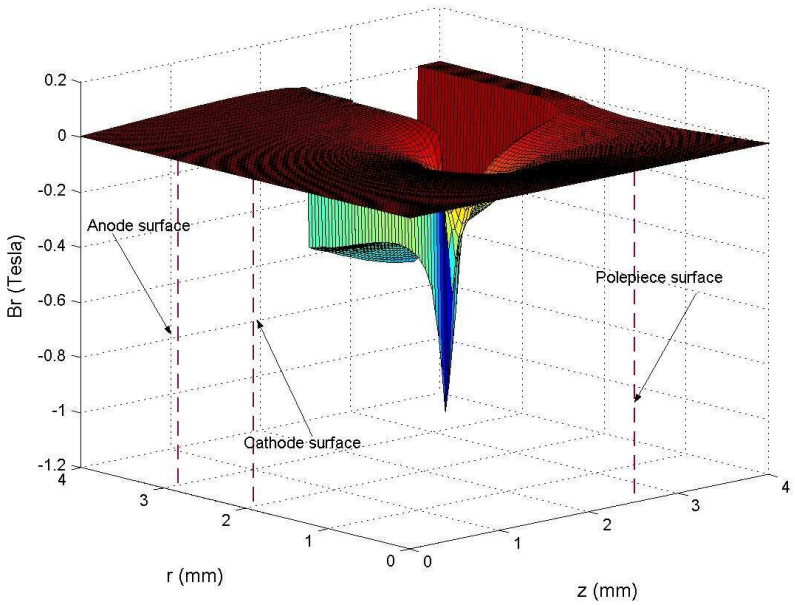

Figure 5.10: The radial magnetic field component distribution used in MG5241P (e2v measurem

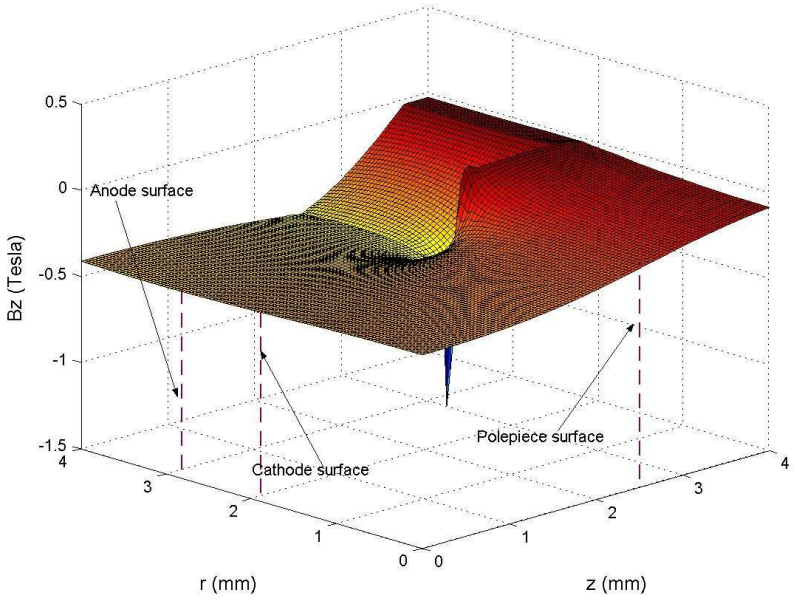

Figure 5.11: The axial magnetic field component distribution used in MG5241P (e2v measurement)

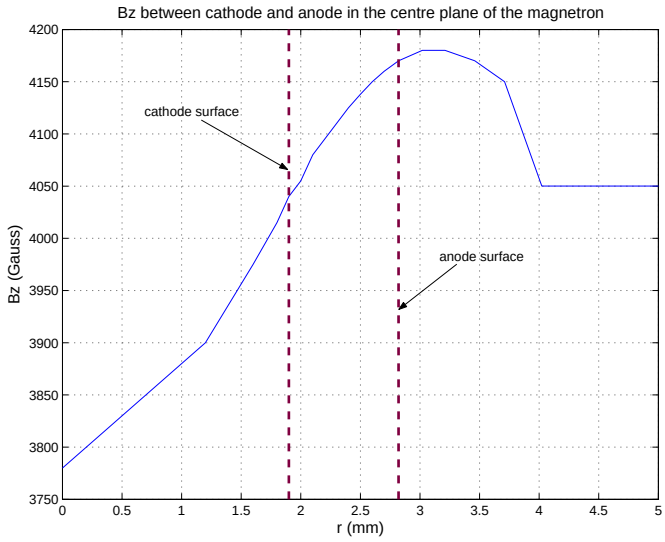

Figure 5.12: radial distribution of the axial component Bz of the real magnetic field, B_{max}=0.418T.

5.4 Hot Test Modelling with Different Cathode Emission Models

5.4.1 Introduction

With the computer model being optimised, more hot test modelling will be described in this section in order to investigate the detail of the operation of the X band magnetron. The hot test modelling is based on two cathode emission models, the space-charge-limited emission model and the beam emission model, which have been described in Chapter 3. The effects of the real magnetic field distribution has been investigated using both emission models. The anode copper surface losses have been simulated in order to be able to study their effect on the start-up of oscillations. The output coupling loop has been investigated in order to obtain a complete set of results, which reveal the effect of the output circuit on the magnetron performance. So far, the cathode secondary emission has not been included, but its effect will be considered in Chapter 7.

5.4.2 The beam emission model

5.4.2.1 Uniform magnetic field 0.405T

The beam emission has first been modeled with a uniform static magnetic field of 0.405T. In the real magnetron, the cathode emission current density is about $15A/cm^2$. With this value simulations have been carried out with the anode voltages varying from 5.17kV to 5.89kV. Table 5-D presents the simulation results. In Figures 5.13(a) to 5.13(c), the computed V-I curves, the output power against average anode current and the overall efficiency against the anode voltage are compared with e2v measured values, for three different magnetic field distributions.

Here an explanation must be given of the type of units used in the performance diagrams. In the hot test modelling, the common EM run time is 40ns. The computed anode current and output power are peak values. The X band magnetron is pulsed, with a duty cycle of 1/1000. Thus, the average anode current in 'mA' is equivalent to the peak anode current in amps; the average output power in 'W' is equivalent to the peak output power in 'kW'.

With the anode voltage varied from 5.17kV to 5.89kV, anode current increased from 1.26A to 3.98A. Compared with the set of experimental results obtained with $B_{max} = 0.398T$, the computed currents are higher at lower anode voltages 5.17kV and 5.30kV; close to the measured values at anode voltages 5.53kV and 5.71kV; and much lower at a high anode voltage of 5.89kV. The computed point '5.89kV, 3.98A' is a rogue result, which deviates from the performance line. This indicates that the beam emission model cannot provide enough current for operation at high anode voltage and high anode current levels. The calculation didn't include the anode copper surface loss. According to the e2v measurements, the circuit efficiency is about 85%. Therefore in Table 5-D and the diagram 5.13(b), the output powers are modified by this amount. The modified output powers are still much higher than the experimental results. The computed overall

Table 5-D: Investigation of beam emission model with uniform magnetic field 0.405T

Magnetic field: uniform 0.4050T					
Q_{ext} from cold test: 244					
Cathode emission model: beam voltage=5eV; beam current density=$15A/cm^2$					
Cathode emission current (A): 6.26					
Effective anode voltage (kV)	5.17	5.30	5.53	5.71	5.89
π mode oscillation start time (ns)	25	V_a step up	7	V_a step up	V_a step up
π mode frequency (GHz)	9.454	9.455	9.451	9.448	9.452
Back bombardment current (A)	5.05	4.50	3.65	2.51	2.25
Anode current (A)	1.26	1.80	2.64	3.70	3.98
Total system energy (J)	59.9e-6	69.0e-6	85.5e-6	98.7e-6	106.0e-6
DC energy (J)	43.6e-6	45.8e-6	50.5e-6	53.8e-6	57.3e-6
System RF energy (J)	16.3e-6	23.2e-6	35.1e-6	44.9e-6	48.7e-6
Hot test $Q_exT = 2\pi f_0 \frac{W}{P_out}$	218	220	222	225	227
Output power (kW)	4.43	6.26	9.40	11.83	12.74
Output power modified by circuit efficiency 85% (kW)	3.77	5.32	7.99	10.06	10.83
Power dissipation on cathode (kW)	0.345	0.429	0.581	0.864	0.930
Power dissipation on anode (kW)	1.76	2.74	4.75	8.80	10.14
Overall efficiency (%)	57.9	55.8	54.7	47.6	46.2
Vane voltage (kV) (amplitude)	2.93	3.38	4.25	4.80	5.00
Output voltage (kV) (amplitude)	0.65	0.75	0.95	1.07	1.11
Output current (A) (amplitude)	13.06	15.06	18.97	21.39	22.29

efficiency is shown in Figure 5.13(c), which increases as the anode voltage decreases. The legends of Figure 5.13(b) and Figure 5.13(c) are same as that of Figure 5.13(a).

The π mode oscillation frequency does not change much with different anode voltages. The hot test Q_{ext}s have been calculated with the knowledge of the system's stored RF energy and the output power, which values are slightly lower than the cold test measured Q_{ext}, but are consistent with different anode voltages.

The rate of rise of anode voltage is another important parameter in magnetron operation. In reality, the RRV (rate of rising voltage) is $100kV/\mu s$, which is not used in the computer simulation because of the unbearably long simulation time it leads to. In

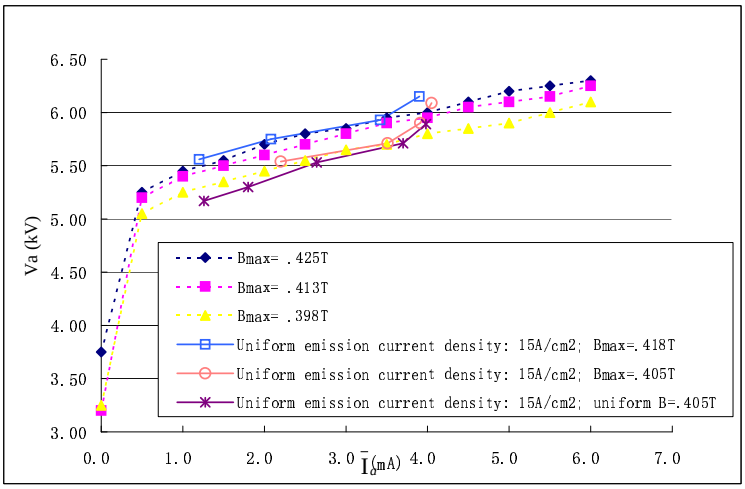

(a)

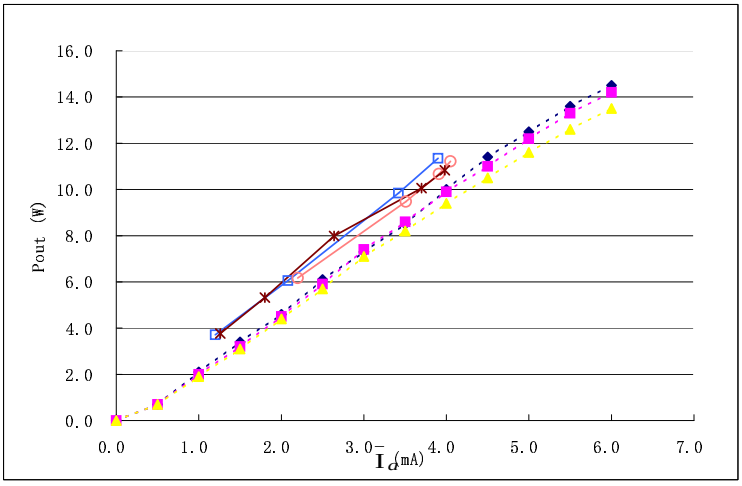

(b)

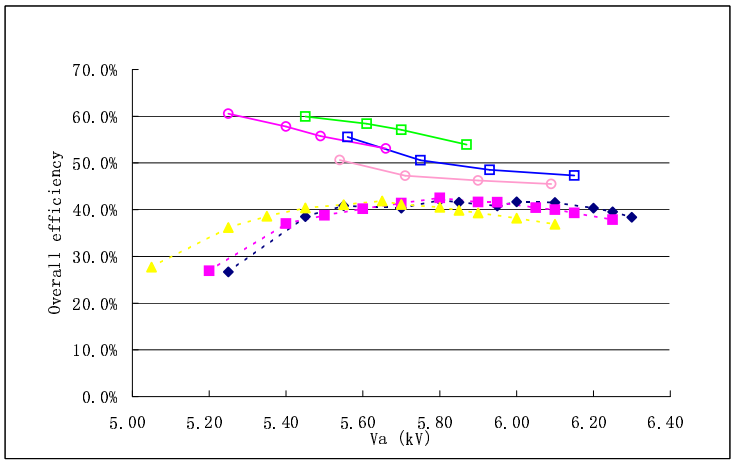

(c)

Figure 5.13: Comparison of the performance of beam emission model with the experimental performance of MG5241P. Solid lines: MAGIC calculation; Dashed lines: e2v measurements. (a) Anode voltage vs anode current. (b) Output power modified by circuit efficiency of 85% vs anode current. (c) Overall efficiency vs anode voltage.

modelling the anode voltage is driven to its full magnitude in 2ns. An investigation of the magnetron operation with slow rate of rising voltage of $100kV/\mu s$ will be carried out in section 5.5.

It can be seen from Table 5-D that at certain anode voltages, magnetron can quickly reach π mode oscillations. For example when $V_a = 5.53kV$, the magnetron develops π mode oscillations within 7ns. At other anode voltages, especially at higher levels, due to a rapid increase of the anode voltage, mode competition becomes very strong and the magnetron may never develop π mode oscillations. Thus in computer modelling, in order to obtain information about the operation of the magnetron at a given anode voltage, when it is known that is difficult in reaching a π mode oscillation, the simulation will be usually started at a voltage that is known to be suitable for π mode oscillations; while the system is stabilised in the π mode, the voltage can then be stepped up or down to reach the desired value.

5.4.2.2 Investigation with the real magnetic field distribution

The real magnetic field distribution is introduced into the computer modelling at this stage. Table 5-E presents the simulation results with real magnetic field distribution of $B_{max} = 0.418T$. With this magnetic field profile, the B_z component at the cathode surface in the center plane of the magnetron is close to 0.405T, making it convenient to compare with the simulation results of the uniform magnetic field distribution. The cathode emission density is kept unchanged. The anode voltage is varied from 5.56kV to 6.15kV. For the convenience of comparison, all the computed performance of the beam emission model with uniform and real magnetic fields are plotted together in Figure 5.13.

At given anode voltages, the computed anode currents with $B_{max} = 0.418T$ are lower than the measured values with the real magnetic field distributions $B_{max} = 0.425T$ and $B_{max} = 0.413T$; the computed output power, even when modified by the circuit efficiency, is much higher than the value measured at the same anode current. Here

Table 5-E: Investigation of beam emission model with real magnetic field, $B_{max} = 0.418T$

Magnetic field: real magnetic field distribution $B_{max} = 0.418T$				
Q_{ext} from cold test: 244				
Cathode emission model: beam voltage=5eV; beam current density=$15A/cm^2$				
Cathode emission current (A): 6.26				
Effective anode voltage (kV)	5.56	5.75	5.93	6.15
π mode oscillation start time (ns)	16	7	30	V_a step up
π mode frequency (GHz)	9.456	9.452	9.452	9.453
Back bombardment current (A)	5.07	4.19	2.83	2.32
Anode current (A)	1.20	2.08	3.42	3.90
Total system energy (J)	66.5e-6	80.7e-6	101.8e-6	113.3e-6
DC energy (J)	50.7e-6	54.2e-6	58.3e-6	62.7e-6
System RF energy (J)	15.8e-6	26.5e-6	43.5e-6	50.6e-6
Hot test $Q_exT = 2\pi f_0 \frac{W}{P_out}$	216	221	223	225
Output power (kW)	4.36	7.12	11.58	13.35
Output power modified by circuit efficiency 85%	3.71	6.05	9.84	11.35
Power dissipation on cathode (kW)	0.381	0.491	0.685	0.821
Power dissipation on anode (kW)	1.90	4.34	8.18	10.20
Overall efficiency	55.6%	50.6%	48.5%	47.3%
Vane voltage (kV) (amplitude)	2.94	3.73	4.73	5.05
Output voltage (kV) (amplitude)	0.66	0.83	1.05	1.13
Output current (A) (amplitude)	13.10	16.63	21.08	22.05

again the copper surface losses are not included in the simulation, instead we use the measured circuit efficiency of 85% to modify the simulated output power and efficiency. Just as in the uniform magnetic field model, the anode current is much lower than the experimental value at high anode voltage of 6.15kV. Though in general the overall efficiency is about 10% higher than the experimental value, it decreases when the anode voltage increases. On this point, it is consistent with the experimental performance.

Modelling has also been carried out with the real magnetic field distribution, but scaled to $B_{max} = 0.405T$ in order to test the magnetron performance at a lower magnetic field level. The anode voltage is varied from 5.54kV to 6.09kV. The simulation results

Table 5-F: Investigation of beam emission model with real magnetic field, $B_{max} = 0.405T$

Magnetic field: real magnetic field distribution $B_{max} = 0.405T$				
Q_{ext} from cold test: 244				
Cathode emission model: beam voltage=5eV; beam current density=$15A/cm^2$				
Cathode emission current (A): 6.26				
Effective anode voltage (kV)	5.54	5.71	5.90	6.09
π mode oscillation start time (ns)	7	V_a step up	V_a step up	V_a step up
π mode frequency (GHz)	9.453	9.453	9.452	9.456
Back bombardment current (A)	4.06	2.72	2.30	2.19
Anode current (A)	2.20	3.51	3.91	4.05
Total system energy (J)	77.2e-6	96.0e-6	105.1e-6	111.7e-6
DC energy (J)	50.5e-6	53.6e-6	57.3e-6	61.0e-6
System RF energy (J)	26.7e-6	42.4e-6	47.8e-6	50.7e-6
Hot test $Q_e xt = 2\pi f_0 \frac{W}{P_o ut}$	219	226	226	228
Output power (kW)	7.26	11.15	12.55	13.20
Output power modified by circuit efficiency 85%	6.17	9.48	10.67	11.22
Power dissipation on cathode (kW)	0.467	0.681	0.801	0.884
Power dissipation on anode (kW)	4.61	8.40	10.21	11.00
Overall efficiency	50.6%	47.3%	46.3%	45.5%
Vane voltage (kV) (amplitude)	3.76	4.65	4.95	5.07
Output voltage (kV) (amplitude)	0.84	1.04	1.10	1.13
Output current (A) (amplitude)	16.76	20.76	22.09	22.59

are consistent with those of the real magnetic field $B_{max} = 0.418T$, nut only at higher anode current levels, see Table 5-F. Anode currents are lower and the overall efficiencies are higher than the experimental results. At high anode voltage levels of 5.90kV and 6.09kV, the anode currents are much lower than the measured values. It can be seen from Figure 5.13 that the computed performance with real magnetic field $B_{max} = 0.405T$ is close to that of the uniform magnetic field 0.405T when the anode voltage is higher than 5.7kV. At lower anode voltages, the computed performance at a given anode voltage with the uniform magnetic field tends to yield more anode current than that with the real magnetic field. The important effect of the real magnetic field is not limited to this phenomenon, in Chapter 6, discussion of further effects due to the real magnetic field

will be presented.

In the above simulation power dissipation due to electron bombarding of the cathode and anode has also been obtained, see Table 5-D, 5-E and 5-F. As mentioned in Chapter 1, this is a great advantage of computer modelling since power dissipation inside a magnetron is difficult to measure experimentally. In all these simulations, energy balance is fully satisfied. Besides the power dissipation on both cathode and anode, the power dissipation on the other parts inside the magnetron such as the pole pieces, has also been investigated and is found to be negligible and therefore omitted from the tables. This also confirms the confining effect of the cathode end hats, which prevent the electrons from flowing sideways and beyond the cathode (see Figure 5.4(b)).

It can be summarised from the above that the current computer model cannot provide enough anode current, especially at high anode voltages, so that the overall efficiency of the model is about 10% higher than in a real magnetron. Therefore there must be some factors missed out in our magnetron model that may induce more anode current and at the same time reduce the efficiency. These factors may be the spurious current from the end hats, the copper surface losses, the cathode secondary emission, or some other features that have been neglected. In the following modelling work, all these factors will be investigated one by one.

5.4.2.3 Investigation of different emission current densities

In all the above modelling work, the cathode emission current density was assumed to be $15A/cm^2$. In order to investigate the effect of different cathode emission current densities, modelling has been carried out with the cathode emission current density of $8A/cm^2$, $10A/cm^2$ and $18A/cm^2$ respectively. The magnetic field was set at 'real' $B_{max} = 0.418T$ and the anode voltage at 5.75kV or 5.74kV (roughly the same). For the convenience of comparison, the simulation results with cathode emission current density $15A/cm^2$ and magnetic field $B_{max} = 0.418T$ are presented again in Table 5-G. It can

be seen from the table that at given anode voltage when reducing the cathode emission current density from $18A/cm^2$ to $8A/cm^2$, the overall efficiency is slightly reduced and at the same time the anode current is also reduced. At a high emission density $18A/cm^2$, the anode current is close to the measured value, but still the high efficiency problem persists.

Table 5-G: Investigation of beam emission model with varied cathode emission density

Magnetic field: real magnetic field distribution $B_{max} = 0.418T$				
Q_{ext} from cold test: 244				
Cathode emission beam voltage: 5eV				
Cathode beam current density (A/cm^2)	8	10	15	18
Cathode emission current (A)	3.35	4.19	6.26	7.54
Effective anode voltage (kV)	5.75	5.75	5.75	5.74
π mode oscillation start time (ns)	9	9	7	8
π mode frequency (GHz)	9.451	9.451	9.452	9.451
Back bombardment current (A)	1.45	2.24	4.19	5.25
Anode current (A)	1.89	1.94	2.08	2.30
Total system energy (J)	76.8e-6	78.5e-6	80.7e-6	83.7
DC energy (J)	53.6e-6	54.2e-6	54.2e-6	54.2e-6
System RF energy (J)	23.2e-6	24.3e-6	26.5e-6	29.5
Hot test $Q_ext = 2\pi f_0 \frac{W}{P_out}$	225	220	221	222
Output power (kW)	6.12	6.56	7.12	7.89
Output power modified by circuit efficiency 85%	5.20	5.58	6.05	6.71
Power dissipation on cathode (kW)	0.350	0.382	0.491	0.596
Power dissipation on anode (kW)	4.54	4.40	4.34	4.78
Overall efficiency	47.8%	50.0%	50.6%	50.8%
Vane voltage (kV) (amplitude)	3.46	3.57	3.73	3.92
Output voltage (kV) (amplitude)	0.77	0.80	0.83	0.88
Output current (A) (amplitude)	15.42	15.94	16.63	17.50

5.4.3 The space-charge-limited emission model

The space-charge-limited emission model has been investigated with uniform and real magnetic field respectively. Different from the beam emission model, which has the cath-

ode emitting at a fixed current density, the space-charge-limited model has the cathode emission limited by the amount of the space charge facing it. The space charge field combined with the DC field keep the normal electric field at the cathode surface equals to zero. In the space-charge-limited emission model, the magnetic field distribution is another factor affecting the cathode emission. This issue will be discussed in detail in Chapter 6.

Simulation has been carried out with uniform magnetic field 0.405T and real magnetic fields $B_{max} = 0.418T$ and $B_{max} = 0.405T$. For all magnetic field distributions, modelling has been carried out with varied anode voltages. The results are summarised in Table 5-H, Table 5-I and Table 5-J. Figure 5.14 compares the VI curves, the output power against the anode current and the overall efficiency against the anode voltage for the computed and e2v measured results. Figures 5.14(b) and 5.14(c) use the same legends as Figure 5.14(a). The calculated performance with a beam emission model are again presented in these diagrams for comparison.

The calculated performance with uniform magnetic field 0.405T coincides with the calculated performance with real magnetic field $B_{max} = 0.418T$, as shown in Figure 5.14(a). At given anode currents, their output powers and overall efficiencies are very close. Here, the output power was modified by including the circuit efficiency of 85% to account for the anode copper surface losses. At given anode voltages, the calculated anode currents of the uniform magnetic field 0.405T are about 0.2Amps higher than for the real magnetic field $B_{max} = 0.418T$.

Comparing the simulation results of the two non-uniform magnetic field distributions with the experimental results, one can see that at a given anode voltage the computer model tends to provide anode current about 50% higher than that of the experimental value. The simulated output power is also much higher than the experimental values at a given anode current, resulting in the calculated overall efficiency more than 10% higher than the corresponding experimental value.

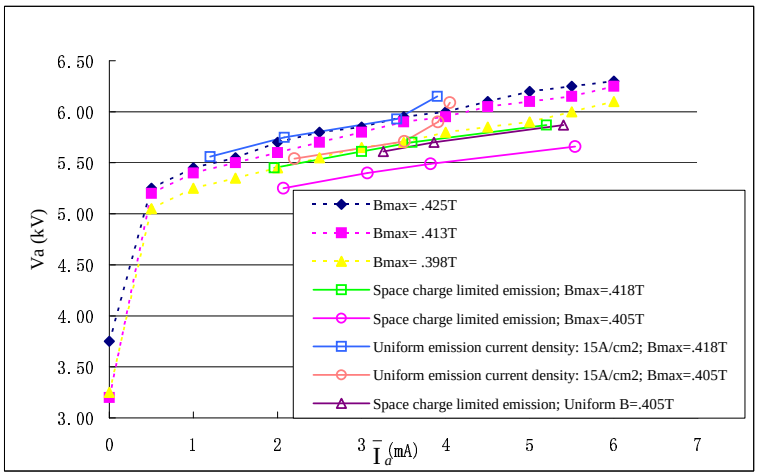

(a)

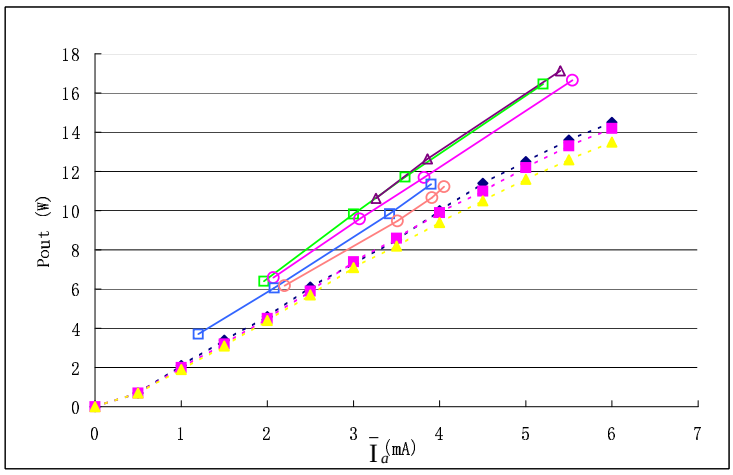

(b)

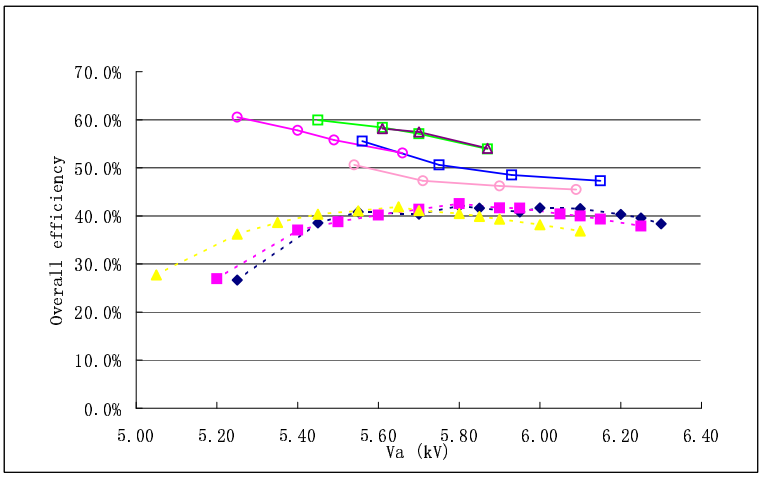

(c)

Figure 5.14: Comparison of the performance of space-charge-limited emission model with the experimental performance of MG5241P. Solid lines: MAGIC calculation; Dashed lines: e2v measurements. (a) Anode voltage vs anode current. (b) Output power modified by circuit efficiency of 85% vs anode current. (c) Overall efficiency vs anode voltage.

Table 5-H: Investigation of space-charge-limited emission model with uniform magnetic field B=0.405T

Magnetic field: uniform B=0.405T			
Q_{ext} from cold test: 244			
Cathode emission model: space-charge-limited			
Cathode emission current (A)	8.59	9.74	11.62
Effective anode voltage (kV)	5.61	5.70	5.87
π mode oscillation start time (ns)	16	12	V_a step up
π mode frequency (GHz)	9.456	9.455	9.453
Back bombardment current (A)	5.36	5.86	6.21
Anode current (A)	3.26	3.86	5.40
Total system energy (J)	99.3e-6	110.1e-6	134.3e-6
DC energy (J)	52.2e-6	54.0e-6	57.3e-6
System RF energy (J)	47.1e-6	56.0e-6	77.0e-6
Hot test $Q_e xt = 2\pi f_0 \frac{W}{P_o ut}$	224	224	226
Output power (kW)	12.51	14.87	20.16
Output power modified by circuit efficiency 85%	10.63	12.64	17.14
Power dissipation on cathode (kW)	0.550	0.640	0.907
Power dissipation on anode (kW)	5.41	7.17	11.30
Overall efficiency	58.1%	57.4%	54.1%
Vane voltage (kV) (amplitude)	4.90	5.36	6.26
Output voltage (kV) (amplitude)	1.09	1.13	1.40
Output current (A) (amplitude)	21.88	25.80	27.92

Another important difference between the calculation and measurement is that when varying the magnitude of the magnetic field, the experimental efficiency won't change much, but the calculated efficiency varies significantly, see Figure 5.14(c). When the anode voltage is between 5.4kV and 6.0kV, the experimental efficiency varies about 2 to 3%; but the calculated efficiency drops by about 5% when the magnetic field is reduced from $B_{max} = 0.418T$ to $B_{max} = 0.405T$.

Comparing the two emission models, the space-charge-limited emission model can provide more than enough anode currents at given anode voltages, while the beam model cannot provide sufficient anode current. The space-charge-limited model also operates

Table 5-I: Investigation of space-charge-limited emission model with real magnetic field, $B_{max} = 0.418T$

Magnetic field: real magnetic field distribution $B_{max} = 0.418T$				
Q_{ext} from cold test: 244				
Cathode emission model: space-charge-limited				
Cathode emission current (A)	7.03	8.90	9.97	12.53
Effective anode voltage (kV)	5.45	5.61	5.70	5.87
π mode oscillation start time (ns)	V_a step down	V_a step down	14	V_a step up
π mode frequency (GHz)	9.457	9.454	9.453	9.453
Back bombardment current (A)	4.95	5.74	6.19	7.20
Anode current (A)	1.96	3.00	3.60	5.20
Total system energy (J)	76.9e-6	95.8e-6	106.1e-6	131.2e-6
DC energy (J)	49.5e-6	52.4e-6	54.1e-6	57.4e-6
System RF energy (J)	27.4e-6	43.4e-6	52.0e-6	73.8e-6
Hot test $Q_e xt = 2\pi f_0 \frac{W}{P_o ut}$	217	223	224	226
Output power (kW)	7.53	11.56	13.78	19.36
Output power modified by circuit efficiency 85%	6.40	9.83	11.71	16.46
Power dissipation on cathode (kW)	0.457	0.665	0.792	1.180
Power dissipation on anode (kW)	2.80	4.91	6.38	10.76
Overall efficiency	59.9%	58.4%	57.1%	53.9%
Vane voltage (kV) (amplitude)	3.84	4.73	5.19	6.12
Output voltage (kV) (amplitude)	0.86	1.06	1.16	1.37
Output current (A) (amplitude)	17.15	21.13	23.18	27.32

at a higher efficiency than the beam model. For the beam model, when increasing the cathode emission density, both the anode current and the overall efficiency tend to increase. This is reasonable because if the cathode emission density keeps increasing, the beam emission model will eventually approach the space-charge-limited model.

From the above analysis, it can be concluded that firstly, the current computer model with both beam emission and space-charge-limited emission can represent the magnetron performance to some degree, the simulated performance curves of these two emission models agreeing with the experimental performance over a range of values; secondly, the space-charge-limited emission model should be used for further investigation, since the

Table 5-J: Investigation of space-charge-limited emission model with real magnetic field, $B_{max} = 0.405T$

Magnetic field: real magnetic field distribution $B_{max} = 0.405T$				
Q_{ext} from cold test: 244				
Cathode emission model: space-charge-limited				
Cathode emission current (A)	6.72	8.60	9.79	12.53
Effective anode voltage (kV)	5.25	5.40	5.49	5.66
π mode oscillation start time (ns)	V_a step down	16	13	V_a step up
π mode frequency (GHz)	9.454	9.453	9.452	9.451
Back bombardment current (A)	4.57	5.42	5.92	6.87
Anode current (A)	2.07	3.07	3.82	5.54
Total system energy (J)	74.3e-6	90.9e-6	102.4e-6	127.9e-6
DC energy (J)	46.0e-6	48.7e-6	50.5e-6	53.7e-6
System RF energy (J)	28.3e-6	42.2e-6	51.9e-6	74.2e-6
Hot test $Q_e xt = 2\pi f_0 \frac{W}{P_o ut}$	217	222	224	225
Output power (kW)	7.74	11.27	13.76	19.59
Output power modified by circuit efficiency 85%	6.58	9.58	11.70	16.65
Power dissipation on cathode (kW)	0.387	0.575	0.720	1.120
Power dissipation on anode (kW)	2.89	5.03	6.83	11.54
Overall efficiency	60.5%	57.8%	55.8%	53.1%
Vane voltage (kV) (amplitude)	3.92	4.67	5.17	6.16
Output voltage (kV) (amplitude)	0.87	1.04	1.15	1.37
Output current (A) (amplitude)	17.49	20.83	23.07	27.46

beam emission model will eventually approach the space-charge-limited emission model when its emission current density is sufficiently increased; thirdly, the current computer model shows a high overall efficiency and the real magnetic field distribution is not the reason. Possible reasons for this discrepancy will be investigated in the following sections.

5.5 Electric Field Distribution between Cathode and Anode

The radial and azimuthal electric field distribution between the cathode and the anode when the magnetron is oscillating in a stable π mode has been computed for both the

space-charge-limited cathode emission and the beam emission models. An initial objective of the computations was to confirm whether the electric field at the cathode was zero for the space-charge-limited emission and to compare this with the field distribution in the beam emission model for a current density of $15A/cm^2$. However, the variation of the field with radius has revealed some interesting features which justified further investigations.

5.5.1 The calculation paths

The E_r and E_θ components have been observed at three different points of an RF cycle, when the system was in stable π mode oscillations. The calculations have been carried out along four radial paths:

$$r \in (r_c, r_a), \theta = 30^0, z = 0; \tag{5.1}$$

which is a radial line in a radial plane through the centre of a cavity, at z=0.

$$r \in (r_c, r_a), \theta = 20^0, z = 0; \tag{5.2}$$

which is a radial line in a radial plane through the centre of a vane, at z=0.

$$r \in (r_c, r_a), \theta = 30^0, z = -1.5mm; \tag{5.3}$$

which is a radial line in a radial plane through the centre of a cavity and near one of the end hats.

$$r \in (r_c, r_a), \theta = 20^0, z = -1.5mm; \tag{5.4}$$

which is a radial line in a radial plane through the centre of a vane and near one of the end hats.

Here $r_c = 1.9mm$ is the cathode radius and $r_a = 2.82mm$ is radius of the inner

anode vane surface. Figure 5.15 shows the angular position of the different paths used for calculations.

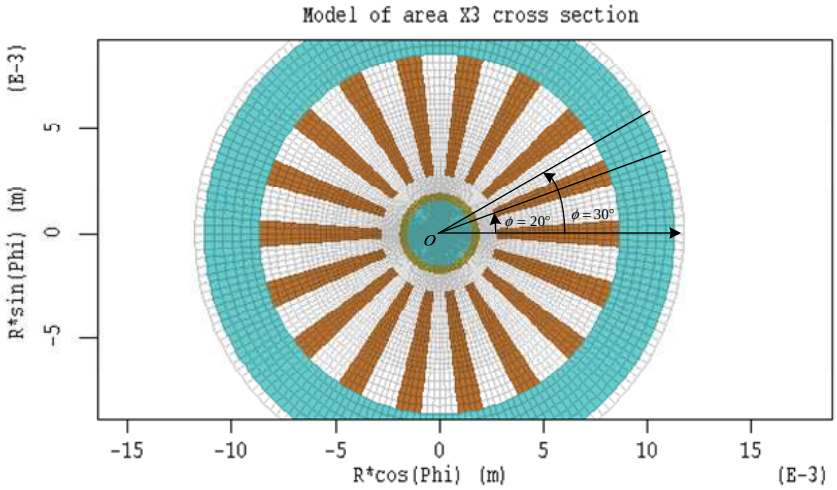

Figure 5.15: Electric field is measured along the solid lines indicated in drawing

5.5.2 Electric field distribution in the beam emission model

The electric field distribution has first been calculated in the beam emission model. The operating conditions are anode voltage 5.75kV, non-uniform magnetic field $B_{max} = 0.418T$, anode current 2.08Amps and cathode emission density $15A/cm^2$ (for detailed operation parameters, see Table 5-E). Figures 5.16 and 5.17 show the variation of E_r and E_θ along the four different paths. The position of the cathode and anode surfaces is indicated on the diagram. The electric fields are marked by '$*$' and '$\circ$' for E_r and E_θ respectively. In the computer model, the calculation grids are allocated so that the anode and cathode surfaces are just on the cell edge. As mentioned in Chapter 3, MAGIC is an FDTD code, in which the radial and azimuthal electric components are calculated alternately at the edge and in the middle of a cell. Therefore on the diagrams the E_θ component is calculated at the cell edges and the E_r component at half cell points.

When a magnetron is oscillating in a stable π mode, there is a core of space charge surrounded by rotating 'spokes' of charge. In Figure 5.16(a), which is plotted along a radial line through the center of a cavity, the field strength at the cathode surface

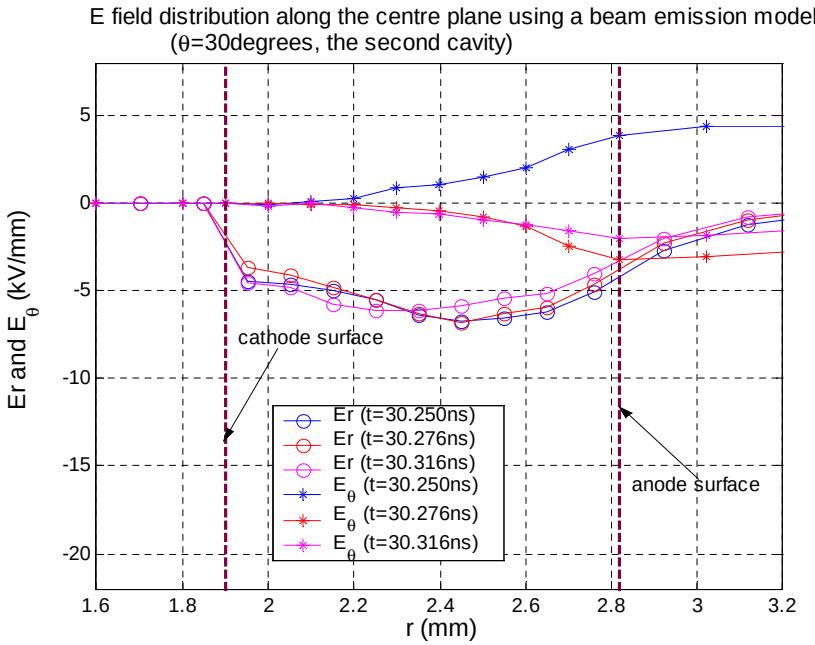

(a)

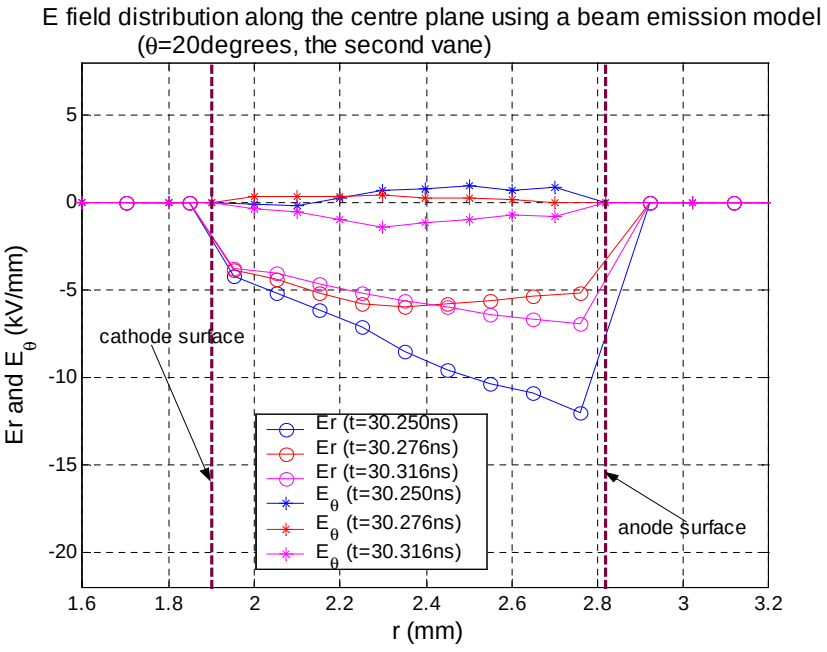

(b)

Figure 5.16: Electric field components are measured along (a) $r \in (r_c, r_a), \theta = 30^0, z = 0$; (b)$r \in (r_c, r_a), \theta = 20^0, z = 0$;

is not zero. The E_r components increase gradually towards the anode and reach a maximum at the boundary of the core of the space charge at about 2.5mm, and then

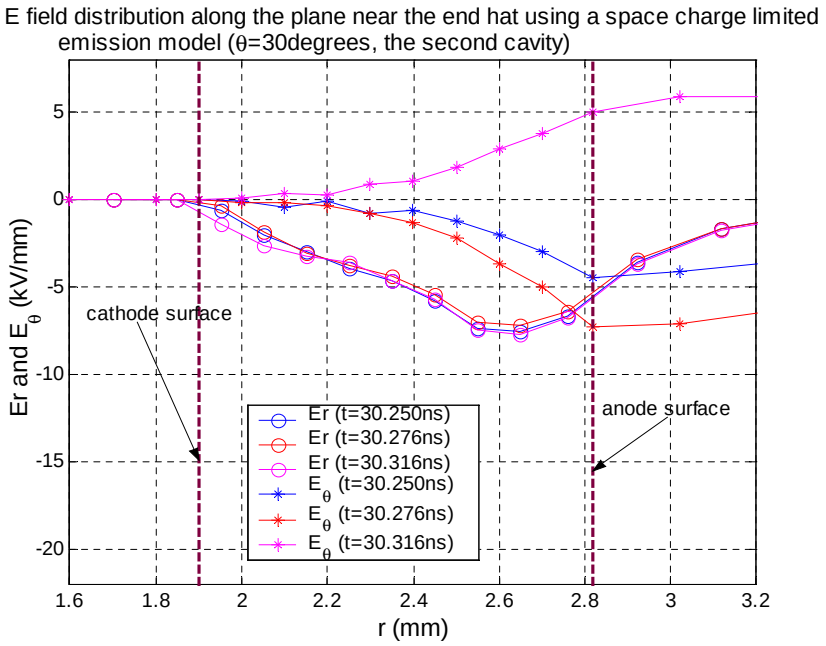

(a)

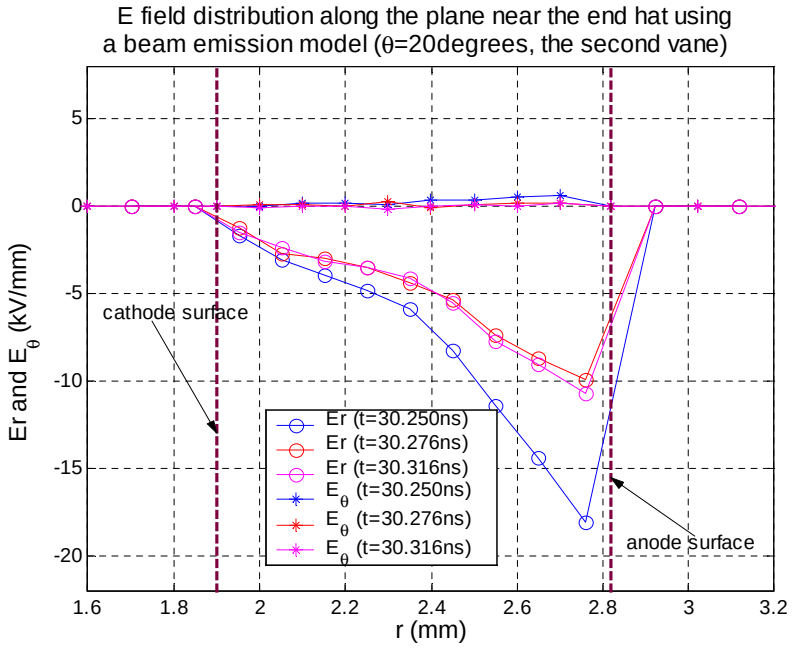

(b)

Figure 5.17: Electric field components are measured along (a)$r \in (r_c, r_a), \theta = 30^0, z = -1.5mm$; (b)$r \in (r_c, r_a), \theta = 20^0, z = -1.5mm$

fall off, approaching zero at the back of the cavity. There is little variation with time, either because the radial electric field due to the electron spokes is small or because the

spokes are opposite the vanes at the instant of measurement. The azimuthal electric field, E_θ, has a small variation in the charge core and then varies with the RF, the amplitude between the vanes being approximately 4kV/mm. In Figure 5.16(b), which shows conditions along a radial line through the center of a vane, there is only slight variation of E_θ with time. This, of course, should be zero, except for space charge fluctuations.

It should be noted that there is an axial variation of the back bombardment current (for detailed discussion, see Chapter 6), therefore the radial electric field variation at the end of the cathode near the end hats is interesting. Figures 5.17(a) and 5.17(b) show this effect, as measured along the lines through the cavity and the vane respectively. It can be seen from these two figures that the E_r components are in general bigger near the anode surface and smaller near the cathode surface than in Figures 5.16(a) and 5.16(b) respectively. This is due to the fact that the gap between the cathode end hats and the anode is quite narrow.

5.5.3 Electric field distribution in the space-charge-limited emission model

With the space-charge-limited emission model, the operating conditions are the anode voltage 5.70kV, the real magnetic field $B_{max} = 0.418T$ and the anode current 3.6Amps (for detailed operation parameters, see Table 5-I).

The computation results plotted in Figures 5.18(a) and 5.18(b) for space-charge-limited emission show that the electric field at the cathode surface is near zero and then increases almost linearly until the boundary of the space charge core is reached at about 2.4mm. This confirms the space-charge-limited emission model discussed in Chapter3. E_θ varies similarly to the beam emission model but its amplitude is greater. The field variation near the end hats also exhibits similar pattern as the beam emission model but at a greater amplitude.

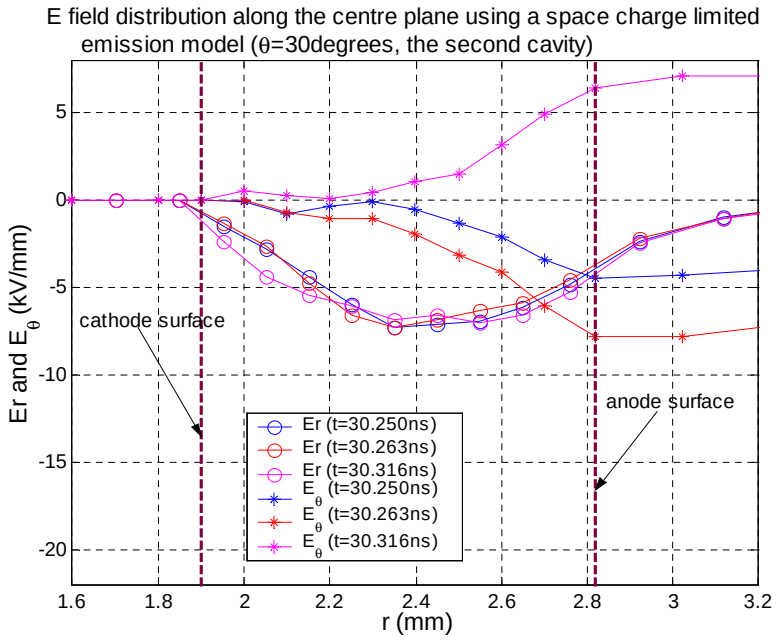

(a)

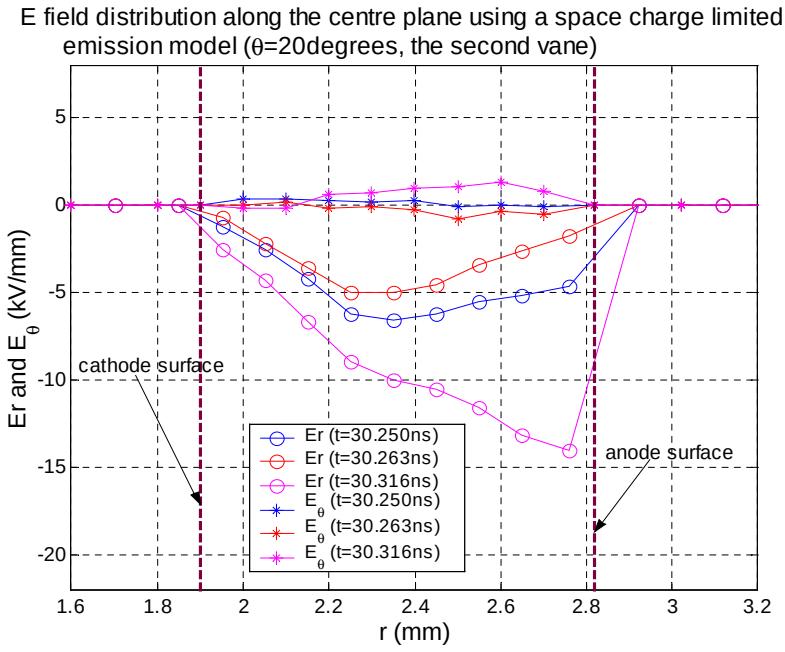

(b)

Figure 5.18: Electric fields are measured along (a) $r \in (r_c, r_a), \theta = 30^0, z = 0$; (b)$r \in (r_c, r_a), \theta = 20^0, z = 0$;

The above investigations of the electric field distribution with both beam emission model and space-charge-limited emission model show quantitatively the differences

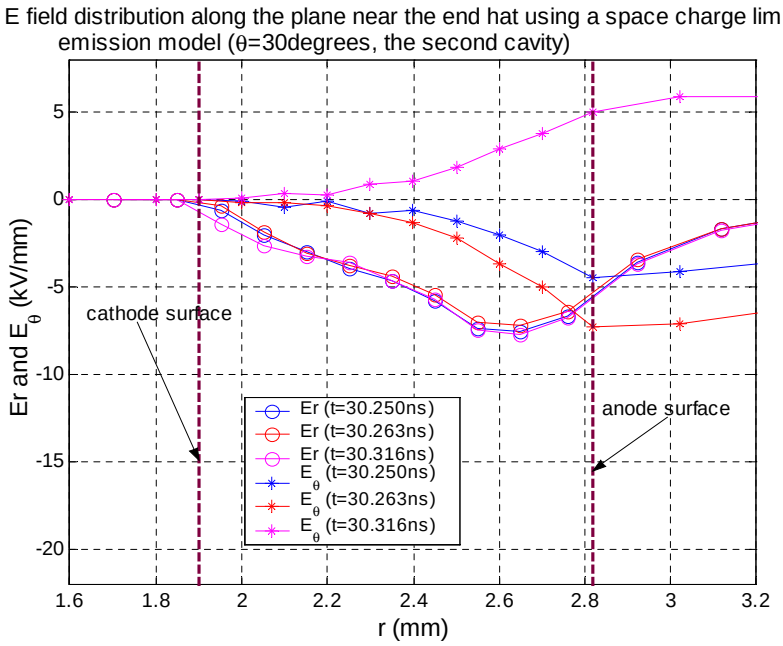

(a)

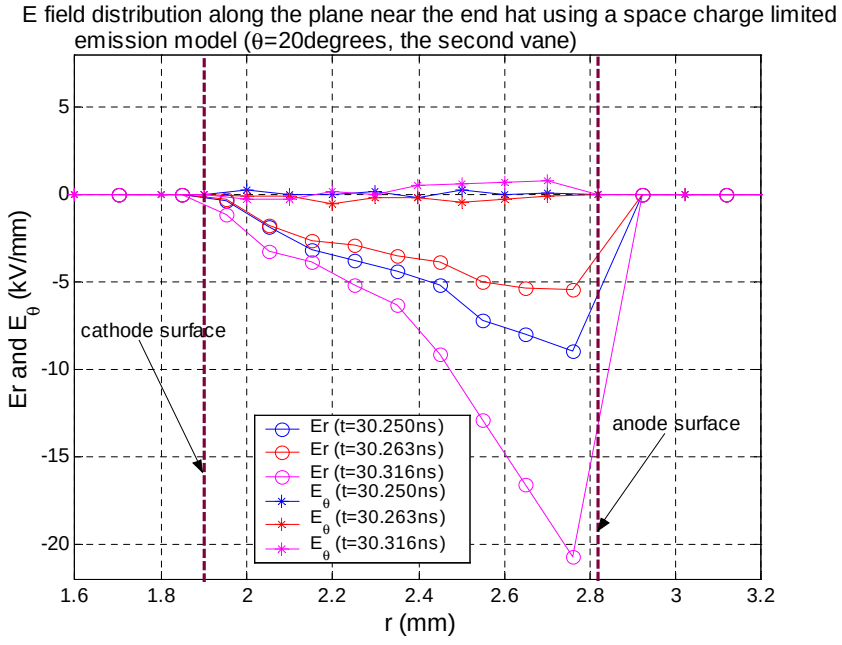

(b)

Figure 5.19: Electric fields are measured along (a)$r \in (r_c, r_a), \theta = 30^0, z = -1.5mm$; (b)$r \in (r_c, r_a), \theta = 20^0, z = -1.5mm$

between the two models. Also from the electric field distribution between the cathode and anode, the radius of the electron cloud when in a stable π mode oscillation can

be measured. Actually the electron cloud radius can always be obtained from an electron cloud snapshot, for example using Figure 5.4(a), which clearly shows the electron cloud in the case of a thick tapering vane model. Thus the method discussed here is a double check on the accuracy of our simulation results. An analysis of the electric field distribution can also help in understanding the intrinsic operation mechanisms of the magnetron.

5.6 Varying the Output Coupling Loop

The output coupling circuit plays a very important role in magnetron operation. Varying the output coupling area, the magnetron performance such as the output power, the anode current and electronic efficiency can change greatly. Figure 5.20 illustrates the geometry of the output coupling circuit. The intrusion length of the coupling loop into the anode is denoted as 'd' in the picture and it will be varied in the following simulations.

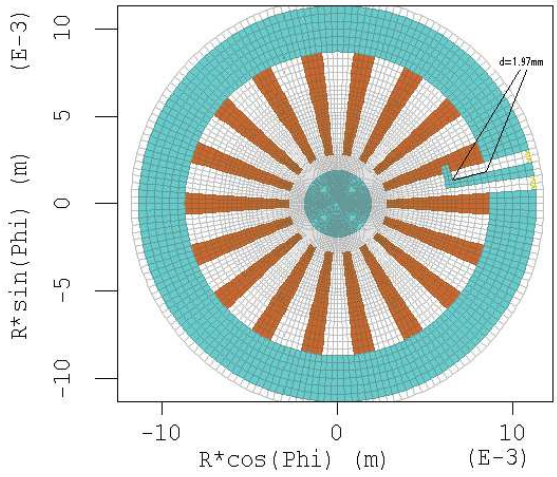

Figure 5.20: The geometry of the output coupling circuit

The initial objective of this investigation is to study the reason for a high overall efficiency of the computer model. It is found that by tuning the output coupling circuit, the overall efficiency is decreased at the expense of Q_{ext} being increased at the same time and a comprehensive set of results has been achieved by varying Q_{ext}, as shown

in Table 5-K. Hot test simulations have been carried out with the output coupling loop length being varied from 2.765mm to 0.78mm. The Q_{ext} varies correspondingly from 183 to 680 and the anode current increases from 3.36A to 6.25A. As mentioned before, the overall efficiency is obtained from the value of output power as modified by the circuit efficiency, which is determined by the Q_0 and Q_{ext} (see section 5.7).

$$\eta_{cold} = \frac{1}{1 + \frac{Q_{ext}}{Q_0}}$$

With $Q_{ext} = 183$, $\eta_{cold} = 85\%$, the Q_0 is 1037. If the Q_0 does not change, increasing the Q_{ext} from 183 to 680 reduces the circuit efficiency from 85% to 60%. The overall efficiency therefore decreases significantly from 60.7% to 21.7%.

Table 5-K: Investigation of the different output coupling with space-charge-limited emission model

Magnetic field: uniform 0.405T							
Cathode emission model: space-charge-limited							
Effective anode voltage (kV): 5.70							
The output coupling loop length d (mm)	2.765	1.97	1.58	1.38	1.18	0.98	0.78
Q_{ext} from cold test	183	260	330	387	440	540	680
Circuit efficiency	85%	80%	76%	73%	70%	66%	60%
π mode oscillation start time (ns)	8	7	7	7	8	8	7
π mode frequency (GHz)	9.418	9.461	9.454	9.451	9.450	9.448	9.446
Anode current (A)	3.36	3.83	4.40	4.84	5.10	5.60	6.25
Output power (kW)	13.68	14.30	14.96	14.95	14.70	14.00	12.86
Output power modified by circuit efficiency	11.63	11.44	11.37	10.91	10.29	9.24	7.72
Power dissipation on cathode (kW)	0.494	0.640	0.830	0.972	1.100	1.200	1.410
Power dissipation on anode (kW)	5.23	7.17	9.80	12.11	13.90	17.20	21.66
Overall efficiency	60.7%	52.4%	45.3%	39.6%	35.4%	29.0%	21.7%
Vane voltage (kV)	4.15	5.15	6.32	7.07	7.50	8.20	8.95

Table 5-K presents detailed results of such modelling, e.g. the vane voltage, anode current, output power and the anode and cathode electron power dissipation. The mag-

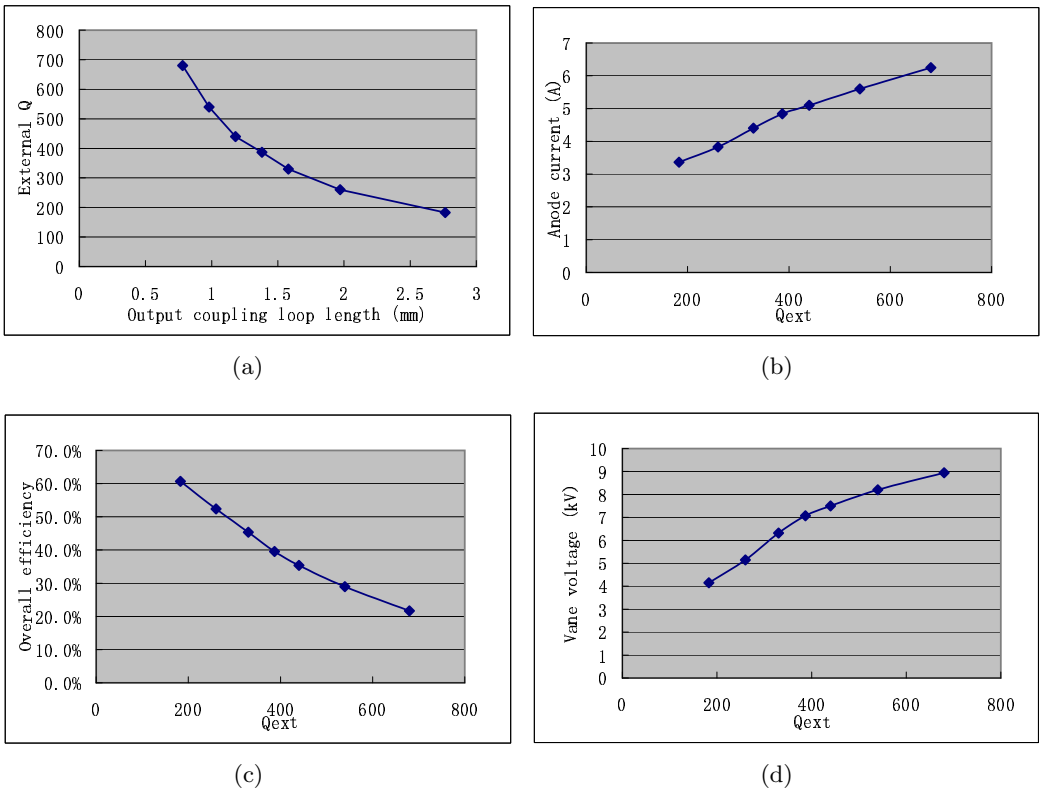

Figure 5.21: Magnetron performance as a function of the output coupling loop. (a) External Q vs output coupling loop length d (b) Anode current vs external Q (c) Overall efficiency vs external Q (d) Vane voltage vs external external Q

netic field is uniform in the axial direction at 0.405T and the input voltage is 5.70kV. At this point MAGIC could not cope with the real magnetic field distribution. The constrains on boundary condition of this version of MAGIC is also different from those of more recent versions. Therefore with the same geometry, ie., the coupling loop length d=1.97mm, the computed Q_{ext}s is somewhat different in these cases. In the old version of MAGIC, Q_{ext} with d=1.97mm is 260. In the new version of MAGIC, by tuning the absorbing boundary conditions of the output ports, the Q_{ext} with d=1.97mm is 244, which is close enough to the old value for a direct comparison of results. We have used this value of Q_{ext} in previous sections.

In Figure 5.21 various relations between different parameters are presented. Figure 5.21(a) shows that the external Q varies with the output coupling loop length nearly

parabolically. Figures 5.21(b) and 5.21(c) show that the anode current and the overall efficiency vary roughly linearly with the external Q. With increasing Q_{ext}, the overall efficiency decreases linearly. This observation is consistent with e2v measurements. Table 5-L presents one set of measurement of the output mismatch, where the efficiency drops when the hot test Q_{ext} increases. The oscillation frequency has also changed, due to the frequency pulling effect. The dependence of RF voltage between adjacent anode vanes on Q_{ext} is shown in Figure 5.21(d). Basically, with increasing Q_{ext}, the anode current will increase and so does the RF vane voltage. In this section the values of Q_{ext} of different geometries are measured by cold tests, as described earlier in this chapter.

Table 5-L: Measurement of the output mismatch (e2v)

Mismatch phase	Mean current (mA)	Anode voltage (kV)	Pin (Watts)	Pout (Watts)	Efficiency (%)	Hot Qext
No mismatch	5.0	5.8	29	11.1	38.3	187
max. power m/m	4.72	5.85	27.6	12.6	45.6	125
min. power m/m	5.30	5.75	30.5	9	29.5	280

Since the overall efficiency is decreased only when Q_{ext} is increased well above its usual value, the conclusion is reached that the output coupling is not the responsible for the high efficiency of the computer model of the MG5241 magnetron.

5.7 Copper Surface Losses

All previous computations have been carried out without considering the anode copper surface loss. Though the overall efficiency can be obtained by multiplying the electronic efficiency by the circuit efficiency, a process which accounts for the copper surface losses, it is really necessary to simulate the copper surface losses when investigating their effect on the magnetron start-up of oscillations. Since during the start-up of process, competition between π and non-π modes depends directly on their respective loaded Q's.

Although the definitions of Q_{ext}, Q_{load} and Q_0 are available in most microwave books, they are given in Appendix 2 as a convenient reference together with the calculation of

the circuit efficiency.

Two different lossy anode models have been investigated. First, the entire inside surface of the anode was defined as a lossy material with conductivity $\sigma = 5.99e7 mhos/m$, this gives a loaded Q of 220, see Table 5-M. But with this model, the simulation time is unbearably long, about twice that for a normal model. Therefore another approach, which introduces lumped lossy elements into the anode system, has been developed in order to reduce the simulation time. Figure 5.22 shows the geometry of the lumped lossy elements. Now the simulation time is greatly reduced and is nearly the same as the ordinary simulation without any copper losses. By properly selecting the size and conductivity of the lossy elements, Q_{ext}, Q_{load} and the cold efficiency can all be tuned close to their experimental values.

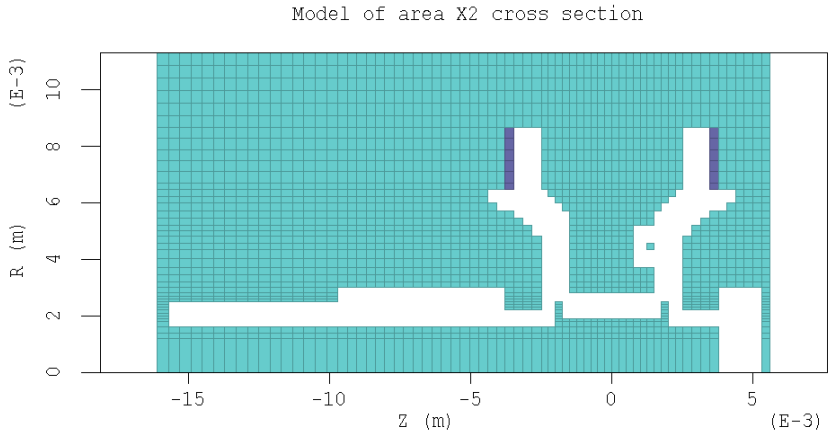

Figure 5.22: The geometry of the lumped lossy elements is shown in dark blue (The conductivity of the two lossy rings is 5.99e5mhos/m)

In the two models, $Q_{ext} = 260$. The corresponding calculation of Q_{load} is based on the cold test energy decay process, which is the same as the calculation for Q_{ext}, but with the surface losses or lossy elements being added. Table 5-M presents Q_{ext}, Q_{load}, Q_0 and the circuit efficiency for the two models.

Three hot test simulation runs have then be carried out respectively without surface loss, with distributed copper surface losses and with lumped lossy elements. Table 5-N summaries the detailed results for these three simulation processes. The space-charge-

Table 5-M: Calculation of Q_0 and circuit efficiency

Loss arrngements	Distributed surface loss	Lumped lossy elements
Q_{ext}	260	260
Q_{load}	220	212
Q_0	1430	1148
Circuit efficiency	84.6%	81.5%

Table 5-N: Investigation of the copper surface losses

Q_{ext}: 260			
Magnetic field: uniform 0.405T			
Cathode emission model: space-charge-limited			
Surface loss arrangement	No surface loss	Distributed surface loss $\sigma = 5.99e7mhos/m$	Lumped lossy element
Q_{load}	/	220	212
Oscillation start at (ns)	7	14	14
Effective anode voltage (kV)	5.84	5.85	5.82
π mode frequency (GHz)	9.460	9.460	9.462
Anode current (A)	5.07	4.83	4.58
Output power (kW)	18.50	16.20	15.17
Power dissipation on cathode (kW)	0.839	0.740	0.685
Power dissipation on anode (kW)	10.87	9.45	8.64
Surface power loss (kW)	/	2.50	2.84
Overall efficiency	53.1%*	57.3%	56.9%
Vane voltage (kV)	6.03	5.60	5.40

* The overall efficiency is obtained by correcting the electronic efficiency with the circuit efficiency of 85%.

limited emission model has been used for all these runs and the magnetic field was kept uniform at 0.405T. In order to help the π mode to dominate, all three simulations start at a lower anode voltage of 5.7kV. This is because at a higher anode voltage, competition between π mode and non π modes is very strong and sometimes may cause the magnetron to jump into non π mode oscillations. When the magnetron settles into stable π mode oscillations, the anode voltages can then be stepped up gradually to obtain a 5Amps anode current, which is the normal operating current in practice. It can be seen from Table 5-N that when without surface losses, the magnetron starts oscillating in the π mode at 7ns; with surface losses or lumped lossy elements, the start of π mode

oscillations is delayed to 14ns. This indicates that by introducing copper losses, the mode competition is getting stronger at the same anode voltage and makes it difficult for the π mode to dominate. The overall efficiency of the two models is still about 10% higher than the experimental value, which is consistent with our earlier investigations in the absence of the copper surface losses.

Therefore, the conclusion can be reached that the copper surface losses are not the reason for the low efficiency of the X band magnetron.

5.8 The End Hat Emission

From the previous investigation, both beam emission model and space-charge-limited emission model operate at overall efficiency levels about 10% higher than the experimental efficiency. Therefore the main objective of the following work is to find out the reason for the lower efficiency of the X band magnetron. It is found from the experimental plots of the output power against anode current as measured at e2v, that a leakage current of about 0.5mA exists in the magnetron. This indicates that a source of spurious current must exist, which has not been included in the current computer model. It is known that cathode end hats emission is a possible source of the spurious anode current and this could reduce efficiency. Therefore in this section, simulation runs will be carried out to investigate the effect of the cathode end hat emission under various conditions. Both space-charge-limited model and beam emission model have been investigated, together with uniform and real magnetic field distributions.

5.8.1 Emission models of end hats

Figure 5.23 illustrates the geometry of the cathode and end hats. The inside surface of both end hats, where possible spurious emission could occur, are divided into 6 cells labeled as 1-6 in our computer calculation. Initially the space-charge-limited emission

model has been used for both the cathode and the end hats. The copper surface losses have not at this point been included in order to reduce the simulation time. Instead, all the output power is corrected by 85% referring to circuit efficiency.

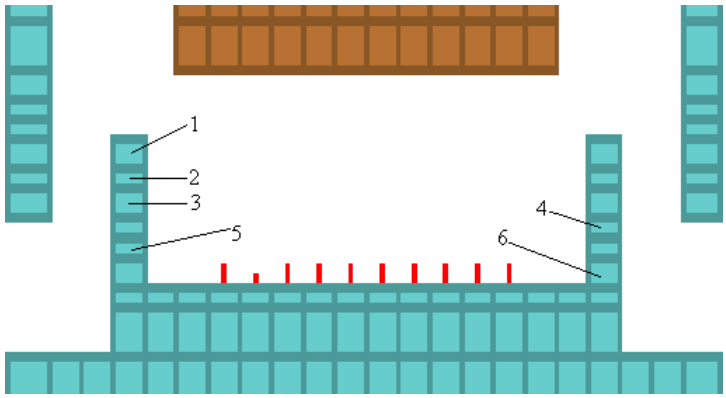

Figure 5.23: The geometry of the cathode end hats

First, preliminary simulation runs have been carried out to investigate possible end hats emission areas. Table 5-O summarises the results of those calculations. In the first emission model all inside cells of the end hats are allowed to emit electrons. With this setup, the anode current rises to 17Amps within 2ns. Then the emission from one, two and three top layers of cells has been investigated. Still the anode current was unrealistically high. Therefore a conclusion must be drawn that the emission from the top three layers of cells of the end hats using space-charge-limited emission model take the system beyond the cutoff and causes a dramatic increase in the anode current. This in itself is an interesting discovery.

Table 5-O: Investigation of possible emission from different areas of the end hats

Emission area	Anode currents
All cells 1 6	Rise up to 17A within 2ns
Cells 1, 2	Rise up to 15A within 1ns
Cell 1	Rise up to 9A within 2ns
Cells 3, 4, 5, 6	Rise up to 3A within 2ns
Cells 4, 5, 6	π mode oscillation, 4.92A
Cells 5, 6	π mode oscillation, 4.1A

In order to verify the above observation, analytical calculations of the cutoff voltage corresponding to different end hat positions have been carried out. The radial coordinates

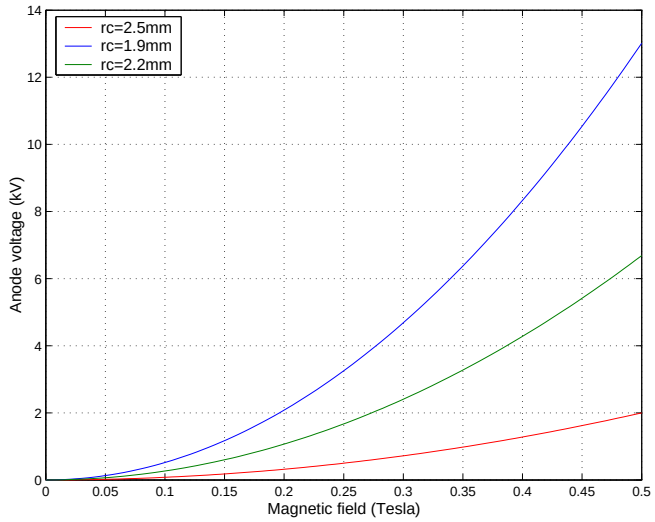

Figure 5.24: Cut off voltage corresponding to different cathode radii

of the top three end hat cells are from 2.2mm to 2.5mm. Figure 5.24 shows the cutoff curves with assumed cathode radii 1.9mm, 2.2mm and 2.5mm. It can be seen that when the magnetic field is 0.405T, the cutoff voltage is 8.50kV with cathode radius 1.9mm and 4.37kV for cathode radius of 2.2mm. The cutoff voltage for cathode radius 2.5mm is even lower. Therefore, the cutoff voltages corresponding to the top three cells of the cathode end hats are far below the operating anode voltage, which is about 5.7kV. This explains why the emission from these cells is so high.

Stable π mode oscillations occurr when end hats emissions are restricted to the bottom two or three layers of cells. Detailed conditions and simulation results are presented in Table 5-P. The magnetic field is kept uniform at 0.405T. For the convenience of comparison, the simulation results without the end hats emission under the same magnetic field and effective anode voltage 5.70kV, are also presented in the table. When including the bottom two layers (cells 5, 6) of the end hats in emission, with the anode voltage 5.69kV, the end hats emitted current is 0.35A from each; the anode current is slightly increased from 3.93A to 4.1A; the overall efficiency is reduced from 55.7% to 53.0%. When including the bottom three layers (cells 4, 5, 6) in emission, the effective anode voltage drops to 5.66kV; the end hats emitted current is 1.15A from each; the anode

Table 5-P: Preliminary investigation of the end hats emission

Q_{ext}: 260			
magnetic field: uniform 0.405T			
Cathode emission model: space-charge-limited			
End hats emission model: space-charge-limited			
End hats emission area	/	cells 4, 5, 6	cells 5, 6
Effective anode voltage (kV)	5.70	5.69	5.66
Oscillation start at (ns)	7	11	14
Cathode emission current (A)	9.74	8.76	9.43
end hats emission current (A)	/	1.15*2	0.35*2
Total cathode back bombardment current (A)	5.86	5.72	5.90
Total anode current (A)	3.93	4.92	4.10
Output power (kW)	14.30	14.73	14.55
Output power modified by circuit efficiency 85%	12.16	12.52	12.37
Power dissipation on cathode	0.640	0.705	0.698
Power dissipation on anode	7.17	12.79	8.20
Overall efficiency	55.7%	45.0%	53.0%
Vane voltage (kV)	5.15	5.24	5.19

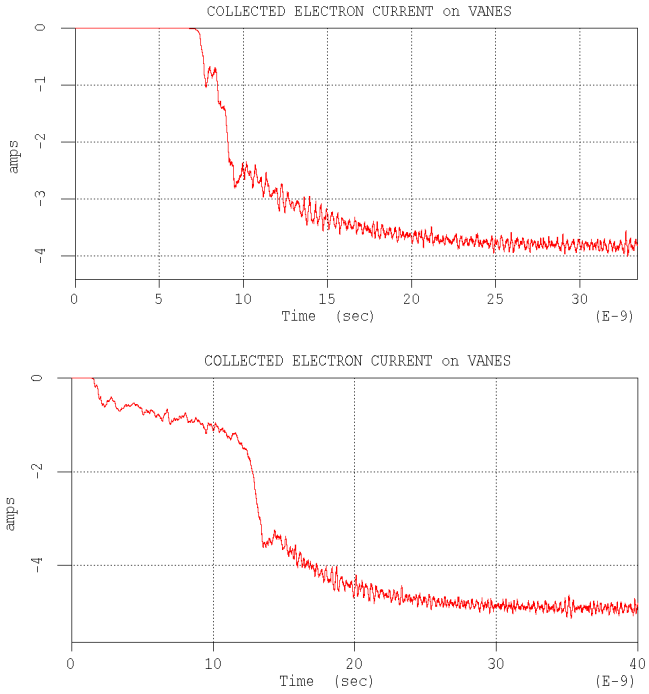

Figure 5.25: Comparison of anode current evolution. (a) Anode current evolution without end hats emission. Anode voltage 5.7kV, magnetic field uniform at 0.405T. (b) Anode current evolution with end hats emission from cells 4, 5, 6. Anode voltage 5.66kV, magnetic field uniform at 0.405T, pre-oscillation anode current $\sim$ 1Amps.

current increases to 4.92Amps and the overall efficiency decreases significantly to 45.0%. Here, in all cases, the overall efficiency is corrected by including the circuit efficiency of 85%.

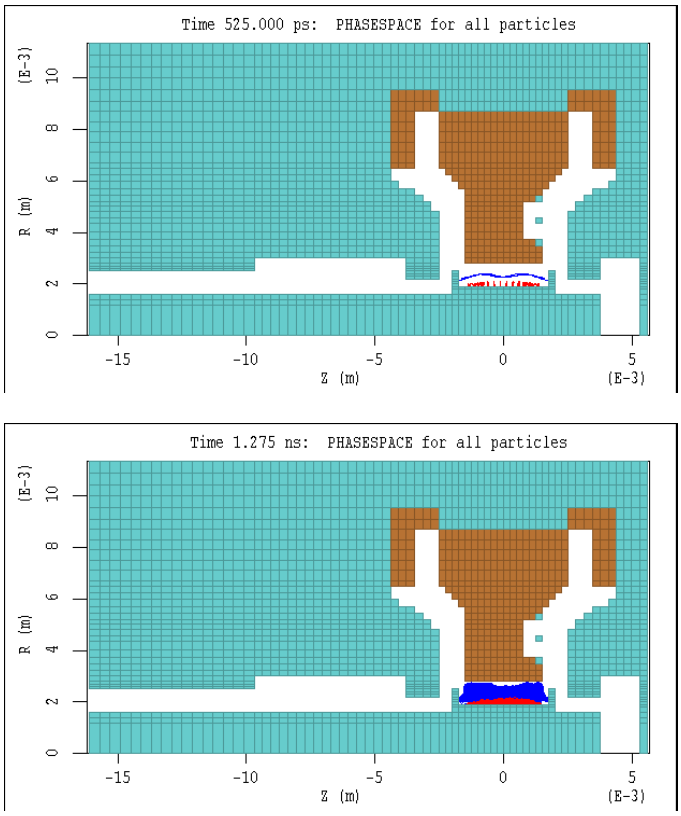

Figure 5.26: The electron cloud including the end hats emission from the bottom three layers of cells 4, 5, 6 at the beginning of the hot test simulation. Anode voltage 5.66kV, magnetic field uniform at 0.405T. (a) t=0.525ns (b) t=1.275ns

Figures 5.25(a) and 5.25(b) compare the anode current evolution with and without end hats emission. Without end hats emission, the waste current or pre-oscillation current is nearly zero. With end hats emission (cells 4, 5, 6), the pre-oscillation current is about 1Amp and the oscillations start at 11ns. Emission from the polepieces has also been observed, but the corresponding current is very weak, about 0.045Amps from each polepiece. The amplitude of vane voltage oscillations does not change significantly. Figures 5.26(a) and 5.26(b) show snapshots of the electron cloud at the beginning of a simulation. It can be seen that the end hat electrons tend to move horizontally towards the centre of the cathode, but do not go straight to the anode.

From our preliminary investigations, it can be concluded that with a space-charge-limited emission model, the end hats emission from the bottom three layers of cells (4, 5, 6) can significantly reduce the overall efficiency and bring it close to the experimental efficiency; this in itself justifies further investigations.

5.8.2 End hats emission with space-charge-limited model and uniform magnetic field of 0.405T

Including electrons emitted from the bottom three layers of cells of the cathode end hats, a number of simulation runs have been carried out with anode voltages varying from 5.70kV to 5.14kV and anode current from 5.11A to 2.24A, the applied magnetic field being uniform at 0.4050T. Since this piece of work was completed before the MAGIC code was updated to include real magnetic field distribution, the cold test external Q of the computer model is 260 in agreement with the early version of MAGIC. Table 5-Q presents the details of the simulation results. In this table, the end hats emission electrons and the cathode emission electrons are treated separately. Therefore their separate contributions to the anode current, back bombardment current, anode power dissipation and back bombardment power are clearly shown. This is very important for the analysis and understanding of the interaction mechanism.

In Figure 5.27, the relations between the anode voltage, output power and anode current are shown. In these diagrams, the results of space-charge-limited emission model without the end hats emission have also been presented for the purpose of comparison. It can be seen from figure 5.27(a) that at given anode current, the output power now agrees well with the experimental result. But at low anode current, i.e., below 3Amps, the output power is lower than the experimental result; extending the curve to zero output power, the intersection point occurs at about 1Amps. This means that the waste current of this computer model is about 1Amps. But the waste current from the measurements is only no more than 0.5Amps. We can see from the diagram of the VI curves (Figure 5.27(b)) that at a given anode voltage, the anode current is far

Table 5-Q: Investigation of the end hats emission with space-charge-limited emission model and uniform magnetic field at 0.405T

Q_{ext}: 260						
magnetic field: uniform 0.405T						
Cathode emission model: space-charge-limited						
End hats emission model: space-charge-limited; emitting from cells 4, 5, 6.						
Effective anode voltage (kV)	5.70	5.66	5.49	5.40	5.24	5.14
Oscillation start at (ns)	14	11	5	2	2	3
Cathode emission current (A)	9.10	8.76	7.34	6.57	5.43	4.81
end hats emission current (A)	1.16*2	1.15*2	1.11*2	1.09*2	1.04*2	1.00*2
Anode current from cathode emission (A)	3.32	3.16	2.13	1.69	1.00	0.70
Anode current from end hats emission (A)	1.79	1.78	1.71	1.68	1.60	1.54
Total anode current (A)	5.11	4.92	3.84	3.37	2.60	2.24
Back bombardment current from cathode emission (A)	5.66	5.62	5.15	4.86	4.46	4.10
Back bombardment current from end hats emission (A)	0.122	0.128	0.177	0.200	0.270	0.316
Output power (kW)	15.25	14.73	11.12	9.40	6.78	5.30
Output power modified by circuit efficiency 85%	12.96	12.52	9.45	7.99	5.76	4.51
Power dissipation on cathode by cathode emission (kW)	0.623	0.600	0.448	0.381	0.284	0.237
Power dissipation on cathode by end hats emission (kW)	0.102	0.104	0.145	0.166	0.215	0.237
Power dissipation on anode by cathode emission (kW)	6.41	5.92	3.67	2.74	1.50	1.00
Power dissipation on anode by end hats emission (kW)	7.04	6.87	6.02	5.59	4.96	4.74
Total power dissipation on polepieces (kW)	0.287		0.201	0.166	0.122	0.089
Overall efficiency	44.5%	45.0%	44.8%	43.9%	42.3%	39.2%
Vane voltage (kV)	5.40	5.24	4.64	4.25	3.61	3.20

higher than the experimentally measured current. Figure 5.27(c) shows that the overall efficiency is lower than the experimental efficiency at low anode current and high at high anode current. The legends of Figure 5.27(a) and 5.27(c) are the same as those of Figure 5.27(b).

It can be concluded that with this emission model, the spurious current being introduced is higher than expected, which affects the magnetron performance more signifi-

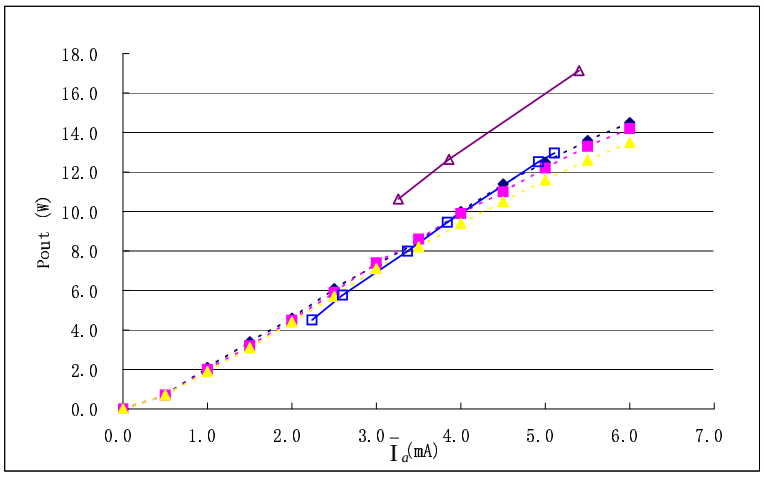

(a)

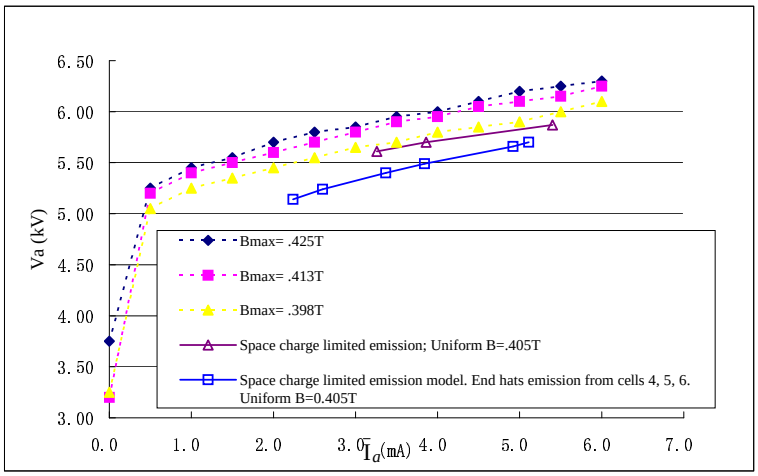

(b)

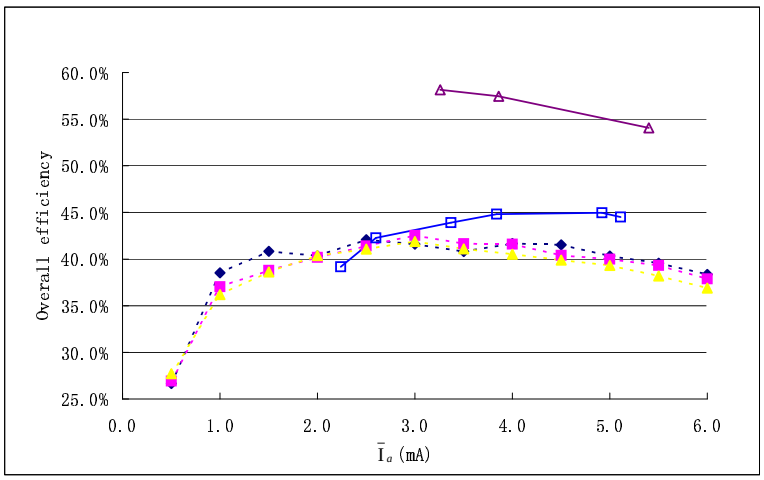

(c)

Figure 5.27: Investigation of the end hats emission from the bottom three cells 4, 5, 6. Uniform magnetic field at 0.405T. Solid lines: MAGIC calculation; Dashed lines: e2v measurements. (a) Output power vs anode current (b) Anode voltage vs anode current (c) Overall efficiency vs anode current

cantly at low anode current levels. This is because at low anode current levels, the contribution of the end hats emission to the total anode current is proportionately greater than at higher anode current levels. For example, when the anode voltage is 5.7kV, the total anode current is 5.11Amps, of which, 3.32Amps is from the cathode emission and 1.79A is from the end hats emission. But when the anode voltage is reduced to 5.14kV, the total anode current is reduced to 2.24A, of which, only 0.70Amps is from the cathode emission and 1.54Amps is from the end hats emission. Although this model can reduce the overall efficiency in general, it cannot give the right results at low anode current.

5.8.3 Reduced spurious current and the real magnetic field distribution

The end hats emission current can be reduced in two ways. One is to reduce number of the end hats emitting cells; the other is to use the beam emission model and control the emitting current density. The first method has already been investigated in section 5.8.1, where simulations have been carried out with different combinations of the end hat emitting cells. We have concluded in that section that with space-charge-limited emission from end hats, only emission from the bottom three layers of cells can give reasonable results and at the same time reduce the overall efficiency significantly. However this model was proved in the previous section to be unrealistic by generating too much spurious current. Therefore the only way to reduce the end hats current is to use the beam emission model and thus control the end hats emission artificially. Since conditions regarding the end hats emission are uncertain and difficult to measure, though artificial, this investigation is still deemed to be useful for studying possible reason for the lower efficiency of the magnetron.

Also at this time, the MAGIC code was updated to allow for a real magnetic field distribution. Therefore in this section, all the simulation runs are carried out with a real magnetic field distribution, in order to diminish possible discrepancy caused by the use of an unrealistic, uniform magnetic field. With a beam emission model, the total end hats emission current is now reduced to 1.664Amps, with 0.832Amps from each

Table 5-R: Investigation of the end hats emission with beam emission model and real magnetic field distribution $B_{max} = 0.418T$

Q_{ext}: 244						
Non-uniform magnetic field: $B_{max} = 0.418T$						
Cathode emission model: beam emission with current density $15A/cm^2$; Total cathode emission current: 6.26A						
End hats emission model: beam emission with current density $10A/cm^2$; Total end hats emission current: 0.832A*2						
Effective anode voltage (kV)	5.90	5.80	5.72	5.63	5.54	5.43
Oscillation start at (ns)	12	10	10	10	10	11
Anode current from cathode emission (A)	3.07	2.29	1.90	1.45	1.10	1.00
Anode current from end hats emission (A)	1.20	1.13	1.10	1.06	1.05	1.04
Total anode current (A)	4.27	3.42	3.00	2.51	2.15	2.04
Back bombardment current from cathode emission (A)	3.19	4.00	4.36	4.85	5.14	5.14
Back bombardment current from end hats emission (A)	0.171	0.222	0.261	0.286	0.295	0.288
Output power (kW)	12.24	9.58	8.15	6.62	5.71	5.18
Output power modified by circuit efficiency 85%	10.40	8.14	6.93	5.63	4.85	4.40
Power dissipation on cathode by cathode emission (kW)	0.627	0.495	0.456	0.410	0.370	0.343
Power dissipation on cathode by end hats emission (kW)	0.088	0.078	0.075	0.067	0.054	0.048
Power dissipation on anode by cathode emission (kW)	7.32	4.95	4.00	2.72	1.75	1.46
Power dissipation on anode by end hats emission (kW)	5.26	5.10	4.70	4.49	4.29	4.16
Total power dissipation on polepieces (kW)	0.353	0.399	0.444	0.509	0.537	0.553
Overall efficiency	41.3%	41.0%	40.4%	39.8%	40.7%	39.7%
Vane voltage (kV)	4.88	4.33	3.99	3.61	3.35	3.17

end hat. Now the emission areas are the whole inside surfaces of the two end hats, that is cells 1-6 in Figure 5.23. The cathode also uses the beam emission model with emission current density of $15A/cm^2$, which gives the total cathode emission current of 6.26Amps. A number of simulation runs have been carried out with anode voltage varying from 5.43kV to 5.98kV. Table 5-R presents detailed simulation results. The cold test Q_{ext} is 244 using this new version of MAGIC, as explained in Section 5.6.

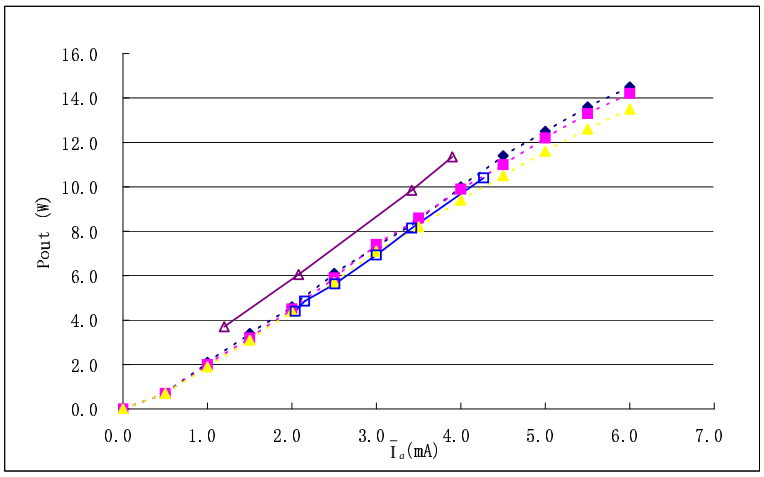

(a)

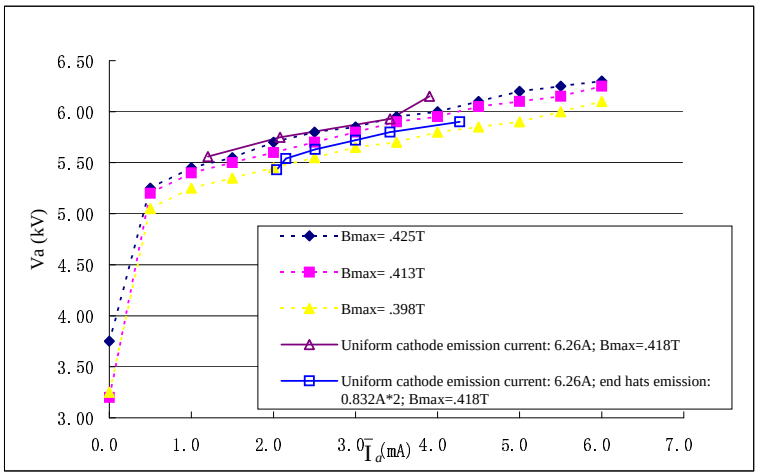

(b)

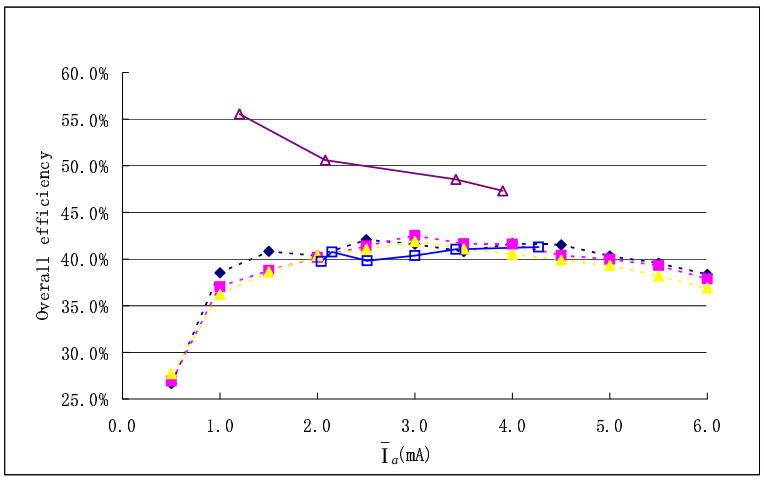

(c)

Figure 5.28: Investigation of the end hats emission with the beam emission model for both the cathode and the end hats. Real magnetic field distribution $B_{max} = 0.418T$. Solid lines: MAGIC calculation; Dashed lines: e2v measurements. (a) Output power vs anode current (b) Anode voltage vs anode current (c) Overall efficiency vs anode current

Figures 5.28(a), 5.28(b) and 5.28(c) show the calculated performance curves together with the measured curves. These three figures share the same legends. For the convenience of comparison, the calculated performance without the end hats emission are also presented on these diagrams. At given anode currents, the difference between the simulated output power and the experimental output power is very small; the overall efficiencies are reduced greatly, especially at low anode currents. But the VI curve is still not right compared with the experimental results. When without end hats emission, at a given anode voltages, the calculated anode currents are always lower than the experimental anode currents. When the end hats emission is included, at a given anode voltage, the anode currents are consistently at least half amp higher than the experimental anode currents; especially when the anode current is as low as 2.04Amps, the calculated anode currents are about 0.8Amps higher than the measured values. Referring to Table 5-R, when the total anode current is 2.04Amps, the contribution from the end hats emission is 1.04Amps. This situation is similar to the previous investigation of the space-charge-limited emission model for the end hats, that is, the waste current is too high at low anode currents. Also from Table 5-R, when the anode voltage varies from 5.9kV to 5.43kV, the contribution of the cathode emission to the total anode current decreases from 3.07Amps to 1.00Amps, but the contribution of the end hats emission to the anode current changes very little, from 1.20Amps to 1.04Amps. Figure 5.29 presents the current contribution relationship between the cathode emission and end hats emission. It can be seen that the end hats emission current actually acts as that in a beyond cutoff diode and therefore does not seem to contribute to the output power.

From the above discussion, the conclusion can be drawn that on its own the end hat emission does not account for the lower efficiency of the X band magnetron, though it can give good agreement with the experimental results for the output power and efficiency, but only at certain anode currents and anode voltages.

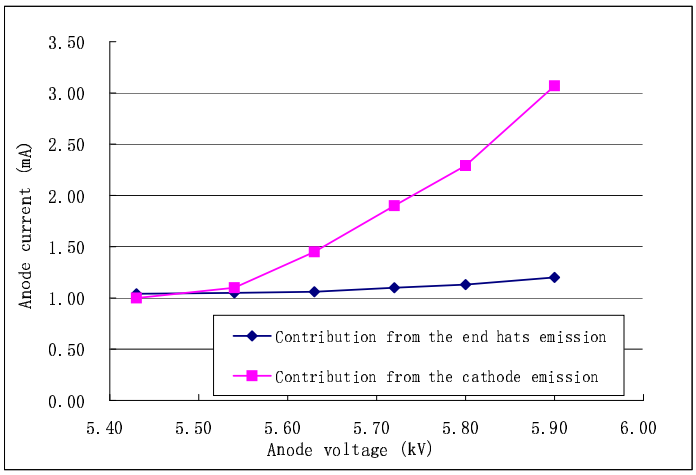

Figure 5.29: The contribution of the cathode emission and end hats emission to the anode current as a function of the anode voltage

5.9 Slow Rate of Rise of Voltage

In all the previous modelling work, in order to save the simulation time, the rate of rise of anode voltage was set at $3000kV/\mu s$, which is 30 times bigger than the value used in practice. In order to investigate the effects of the real RRV on magnetron start-up, which is only $100kV/\mu s$, simulation runs have been done with anode voltage at 5.70kV and 5.87kV. Table 5-S presents the operation conditions. Figure 5.30 shows the transient evolution of the stored system energy, the vane voltage oscillations, the input anode voltage and the anode current while the effective anode voltage is 5.87kV. Figure 5.30(a) shows that the anode voltage rises up to 6.0kV within 60ns and drops to 5.87kV, which is an average value, when the magnetron gets into a stable π mode oscillation. It can be seen from Figures 5.30(b), 5.30(c) and 5.30(d) that before the magnetron gets into a stable π mode oscillation, the anode current is very low, about 0.7A; the RF energy stored in the magnetron is also very low; the voltage oscillation between anode vanes is very noisy due to the spurious oscillations of non-π modes. The calculation of the DC energy and RF energy has been discussed in section 5.2.3. Figure 5.31 presents the spectrum of the vane voltage oscillation during the magnetron start-up between 55ns and 70ns. Apart from the π mode oscillation around 9GHz, there are strong spurious

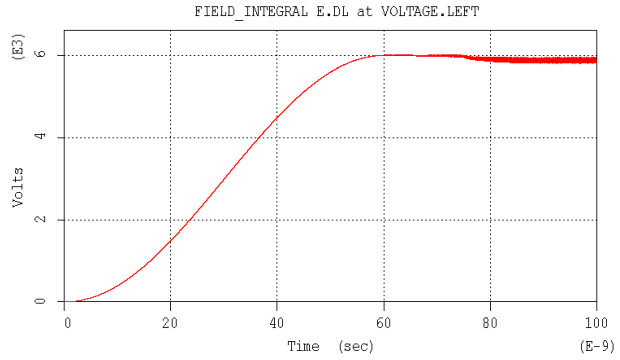

(a)

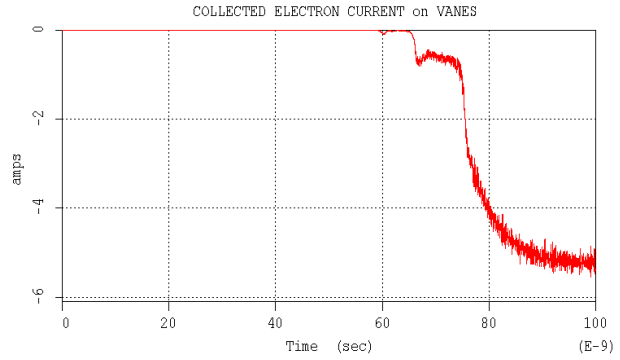

(b)

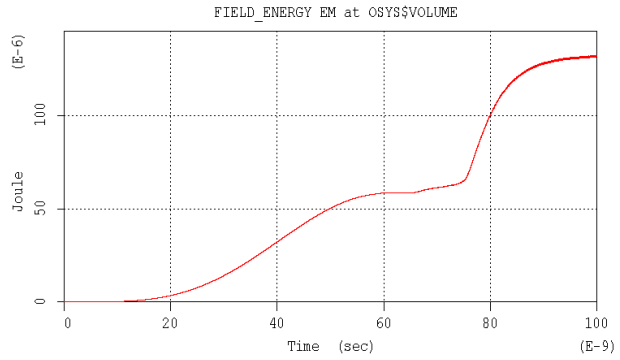

(c)

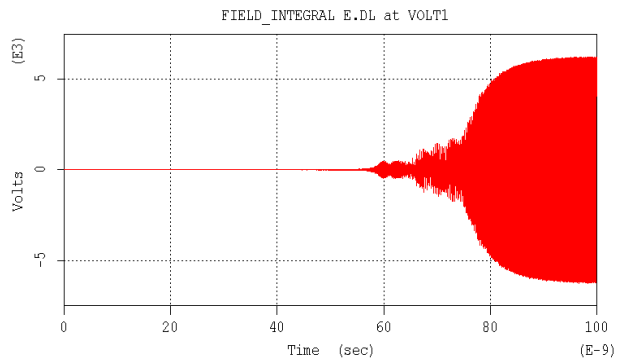

(d)

Figure 5.30: The simulated transient evolution of the main parameters obtained with the slow RRV of $100kV/\mu s$. (a) The effective anode voltage 5.87kV. (b) The anode current 5.26A. (c) The system stored energy, the DC energy is 58.5e-6J; the RF energy is 73.1e-6J. (d) The voltage oscillation between two adjacent vanes.

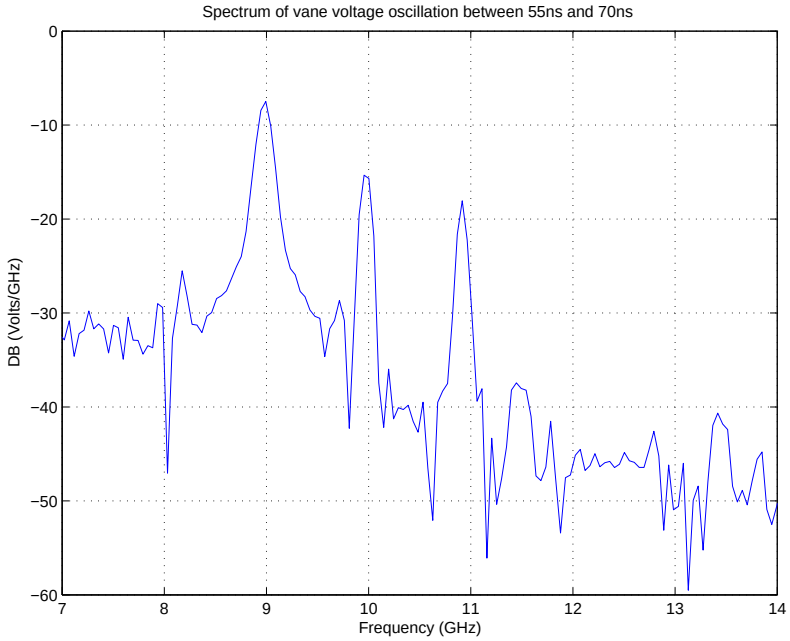

Figure 5.31: Oscillation spectrum of the vane voltage during the start-up of magnetron oscillations

Table 5-S: Simulation runs with slow RRV of $100kV/\mu s$ and space-charge-limited emission model

Q_{ext}: 244		
Non-uniform magnetic field: $B_{max} = 0.418T$		
Effective anode voltage (kV)	5.70	5.87
Oscillation frequency (GHz)	9.454	9.454
Anode current (A)	3.26	5.62
Output power (kW)	13.87	19.42
Overall efficiency	57.1%	53.4%
Vane voltage (kV)	5.20	6.13

modes at 10GHz, 11GHz, etc.

Therefore by applying an experimental value of the RRV in our simulations, details of the transient oscillations in a magnetron have been revealed, such as the mode competition, the RF energy build-up and the anode current evolution.

5.10 Summary

In this chapter, an X band magnetron has been modelled in some detail. Investigations of different computer models show that the 'thick tapering vane' model is the best to represent this particular X band magnetron. Different cathode emission models together with uniform or non-uniform magnetic fields have been investigated, in order to obtain a complete set of results for comparison with experimental results. The computer model generates an overall efficiency which is about 10% higher than the experimental efficiency. Possible reasons for the discrepancy have been investigated, such as the copper surface losses, the output coupling loop circuit, the end hats emission and the rate of rise of anode voltage. Though most of these factors have been proved not to be the reason for the low efficiency of the magnetron, in the process, some important insights into the operation of the X band magnetron have been gained. The quantitative relations between the output coupling loop area, the overall efficiency and the Q_{ext} have been obtained. Though the end hats emission can bring the simulated performance close to the experimental one, the effect appears to be artificial, bring the tube beyond cutoff condition. Simulation using a real RRV has revealed details of the start-up characteristics of a magnetron. So far, no simulation included the important cathode secondary emission because of some instability problems. The conditions for cathode secondary emission and its possible effects on magnetron operation will be discussed in Chapter 6 and 7.

References

[1] S.Y.Liao, Ed., *Microwave devices and circuits.* Prentice Hall Internationsl, 1990.

Chapter 6

The Effects of Non-Uniform Cathode Emission and Electron Back Bombardment

6.1 Introduction

In this chapter, the cathode emission and back bombardment distribution along the length of the cathode have been investigated using two different cathode emission models, the space-charge-limited emission and the beam emission. For each emission model, simulation runs have been conducted both with the uniform magnetic field and the real magnetic field distributions respectively. Their corresponding effect on magnetron performance is then carefully considered. Since a non-uniform electron back bombardment distribution along the cathode length would result in a complicated secondary emission distribution, its possible effect on magnetron performance was investigated by artificially simulating cathode emission with a Gaussian profile.

6.2 Simulation Model

In our previous work the cathode was treated as a single unit, which emits electrons and absorbs back bombarding electrons. In this chapter, in order to investigate the distribution of the cathode emission and back bombardment along the cathode length, the cathode is divided into 14 ring shaped units, as shown in Figure 6.1.

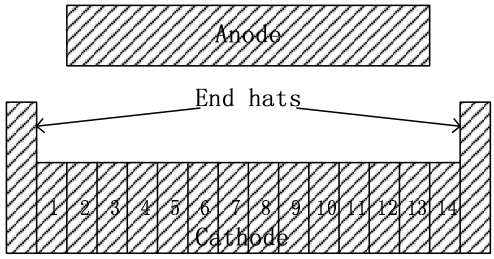

Figure 6.1: The length of the cathode is divided into fourteen rings

Here 'cath1' is located adjacent to the left end hat, its axial coordinates being (-1.75mm to -1.5mm);

$$\begin{aligned}
\text{cath2:} \quad & z \in (-1.5mm, -1.25mm); \\
\text{cath3:} \quad & z \in (-1.25mm, -1.0mm); \\
& \cdots\cdots \\
\text{cath7:} \quad & z \in (-0.25mm, 0); \\
\text{cath8:} \quad & z \in (0, 0.25mm); \\
& \cdots\cdots \\
\text{cath14:} \quad & z \in (1.5mm, 1.75mm).
\end{aligned}$$

Calculations of the cathode emission and back bombardment have been carried out individually on each ring.

6.3 Investigation of the space-charge-limited Emission Model

6.3.1 Characteristics of cathode emission and back bombardment distribution along the cathode length

With the space-charge-limited emission model, modelling has been carried out with different DC voltages and different values of both uniform and real magnetic field. The results show that in all the cases, the cathode emission current is non-uniformly distributed along the cathode length, see Figure 6.2. When the real magnetic field distribution is applied, the distribution of the emitted current density along the cathode length is approximately Gaussian. When using a uniform magnetic field, the current density distribution becomes somewhat unexpected; there are two spikes in the distribution curves which are situated near the end hats. The magnitude of the DC voltage or the magnetic field (uniform or real) do not affect the emission distribution curves significantly.

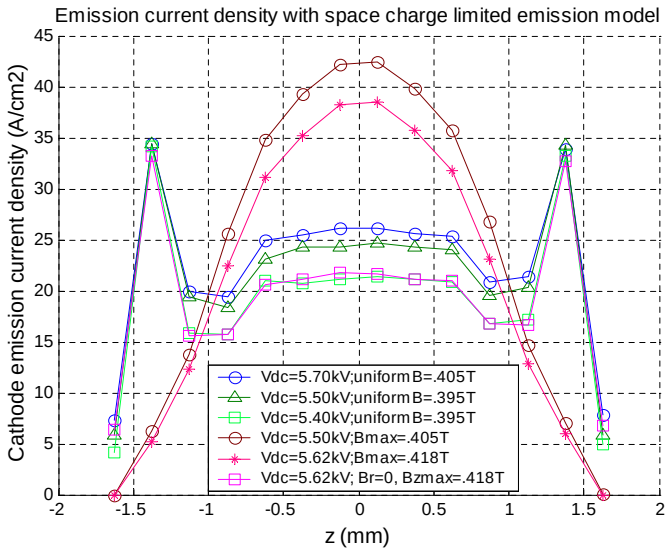

Figure 6.2: Cathode emission current density distribution along the cathode length when using the space-charge-limited emission model

Tables 6-A and 6-B present the corresponding results and operating conditions. As introduced in Section 5.3, the real magnetic field distribution is 2D with both B_z and B_r components, while a uniform magnetic field has only the B_z component. Is this then

the B_r component that cause the difference in the cathode emission distribution? In order to test this hypothesis, a simulation was carried out with zero B_r component but retaining the B_z component as measured at e2v (B_{max}=.418T). Now, the two spikes appear in the emission current density distribution appear again as they did in the case of a uniform magnetic field. This confirms that the B_r component affects the cathode emission distribution significantly and in modelling the real magnetic field distribution should never be replaced by a uniform magnetic field.

Table 6-A: Simulation results with the space-charge-limited emission model and real magnetic field distribution

Cathode emission model	space-charge-limited		
Effective input voltage (kV)	5.62	5.50	5.62
Non-uniform magnetic field (T)	B_{max}: 0.418	B_{max}: 0.405	Br=0 Bz(max)=0.418
Anode current (A)	3.0	3.82	2.78
Input power (kW)	17.05	21.26	15.60
Output power (kW)	11.56	13.78	10.94
Vane voltage (kV)	4.73	5.17	4.60
Electronic efficiency (%)	67.8	67.8	70.1

Table 6-B: Simulation results with space-charge-limited emission model and uniform magnetic field distribution

Cathode emission model	space-charge-limited		
Effective input voltage (kV)	5.62	5.50	5.62
Uniform magnetic field (T)	0.405	0.395	0.395
Anode current (A)	3.86	3.78	3.05
Input power (kW)	22.40	20.64	16.56
Output power (kW)	14.88	13.40	11.41
Vane voltage (kV)	5.15	5.20	4.71
Electronic efficiency (%)	66.4	64.9	68.9

Figure 6.3 and 6.4 show the back bombardment voltage and current density distributions along the cathode length. The back bombardment electron voltage (or electron power) has an approximately Gaussian distribution along the cathode length, somewhat surprisingly irrespective of a uniform or real magnetic field distribution. However the current density distribution depends on the shape of the magnetic field. When the magnetic field is uniform, the back bombardment current density is roughly uniform in the

center region, but drops sharply to zero towards both ends of the cathode. When the real magnetic fields is used, back bombardment current gradually decreases towards the ends of the cathode. Thus again the B_r component plays an important role in the back bombardment distribution. An explanation of this phenomenon is provided in the next section, using simple particle kinematics.

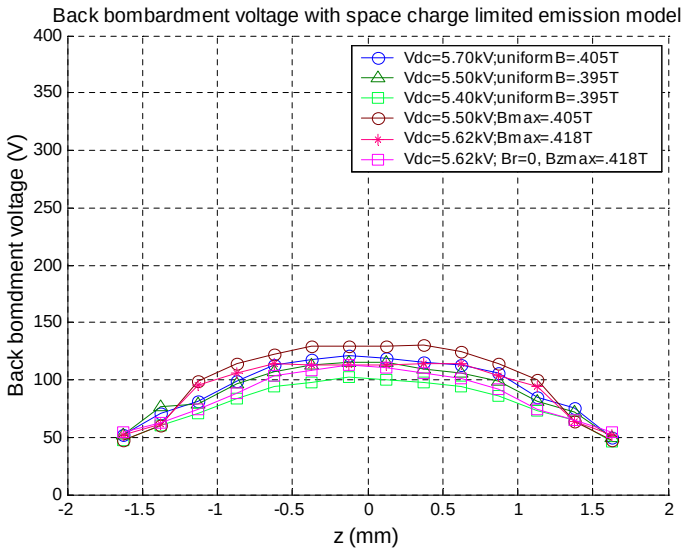

Figure 6.3: Back bombardment Voltage distribution along the cathode length

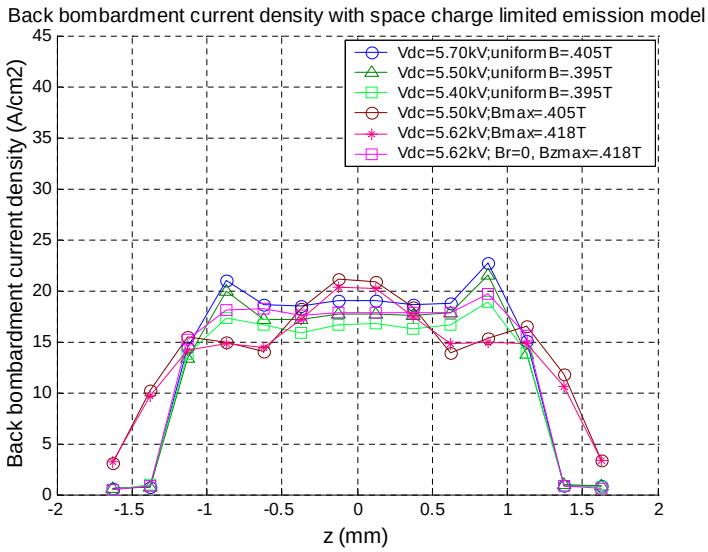

Figure 6.4: Back bombardment current density distribution along the cathode length

6.3.2 Electric and magnetic field variation along the cathode surface

In order to reveal how the B_r component affects the cathode emission and back bombardment distribution along the cathode length, the electric and magnetic fields above the cathode surface and the electron motion under their influence are investigated. As shown in Figure 6.1, the cathode is divided into fourteen rings along its length. Since the boundary conditions on a metal surface require that the tangential electric field component must be zero, in the region near the inside surface of the end hat the electric field is mainly in the E_z direction; moving towards the center of the cathode, the electric field becomes mainly radial or E_r. Figures 6.5 and 6.6 show the variation of E_r, E_θ and E_z along the cathode length at different azimuthal and radial positions, respectively when uniform and real magnetic fields are.

With the space-charge-limited emission model, very few electrons are emitted from the cathode rings 1 and 14 because the E_r component near the end hat ($z = \pm 1.75mm$) is too weak; E_r component distribution along the cathode length is roughly uniform between rings 2 and 13 (-1.5mm -1.5mm).

In the presence of a uniform magnetic field, the only force on the electrons in the longitudinal direction is eE_z, so that electrons leaving rings 2 and 13 tend to move towards the cathode center under the influence of the E_z component. This keeps the space charge density above those two rings quite low. When using the space-charge-limited emission model, this is no longer the case, since more electrons will be emitted from the two cells. This explains the two spikes in the emission current density distribution in the presence of a uniform magnetic field.

Figure 6.7 shows the electron cloud emitted from different cathode sections at the beginning of the emission and at the magnetron oscillates in a stable π mode. It is obvious from these diagrams that electrons emitted from the sections near the end hats tend to move towards the cathode center.

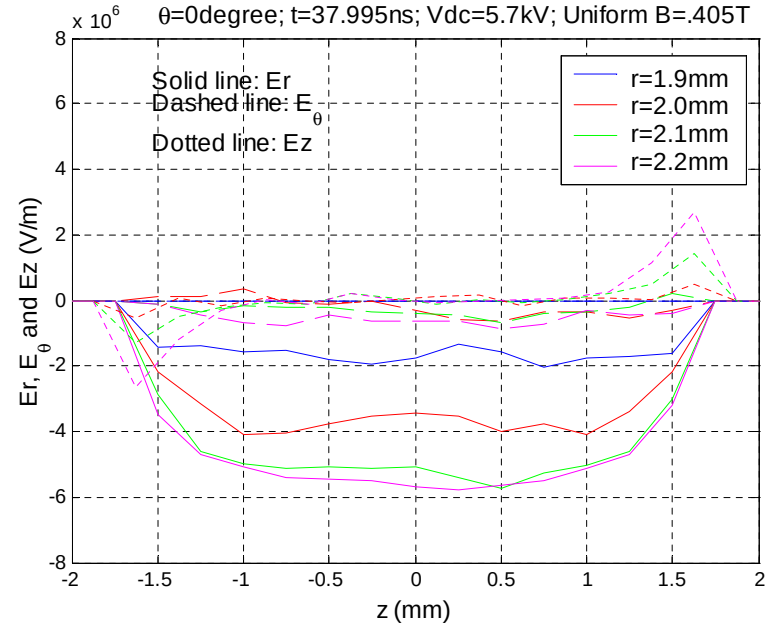

(a)

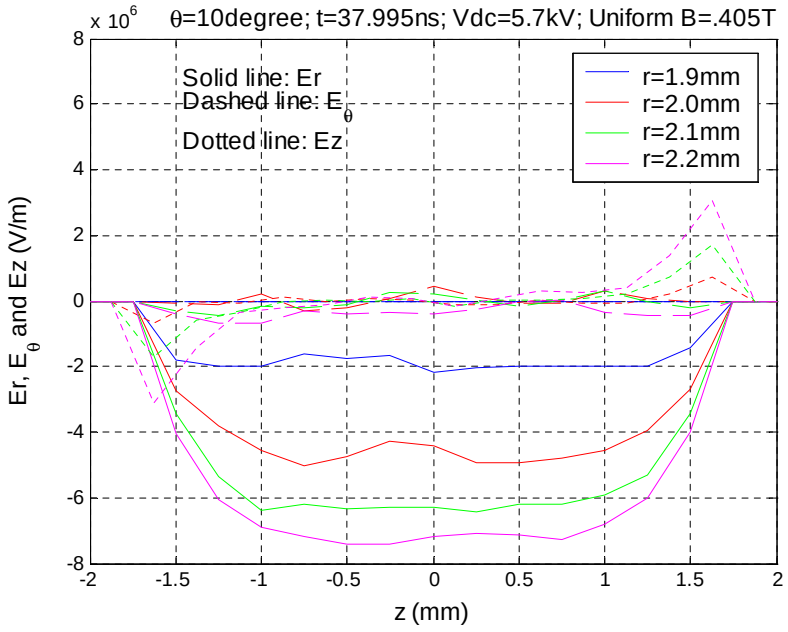

(b)

Figure 6.5: Electric field distribution along the cathode length at different azimuthal positions. $V_{dc} = 5.7kV$, uniform magnetic field 0.405T. (a) Opposite the vane, $\theta = 0°$ (b) Opposite the cavity, $\theta = 10°$

But the situation is different when the real magnetic field is applied. Figure 6.8 shows the B_r and B_z variation along the cathode length. It can be seen that the B_z component

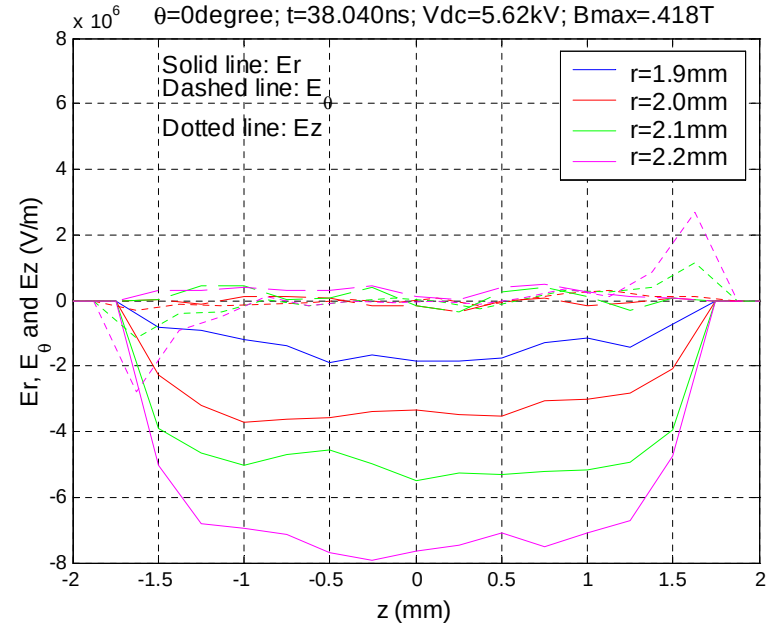

(a)

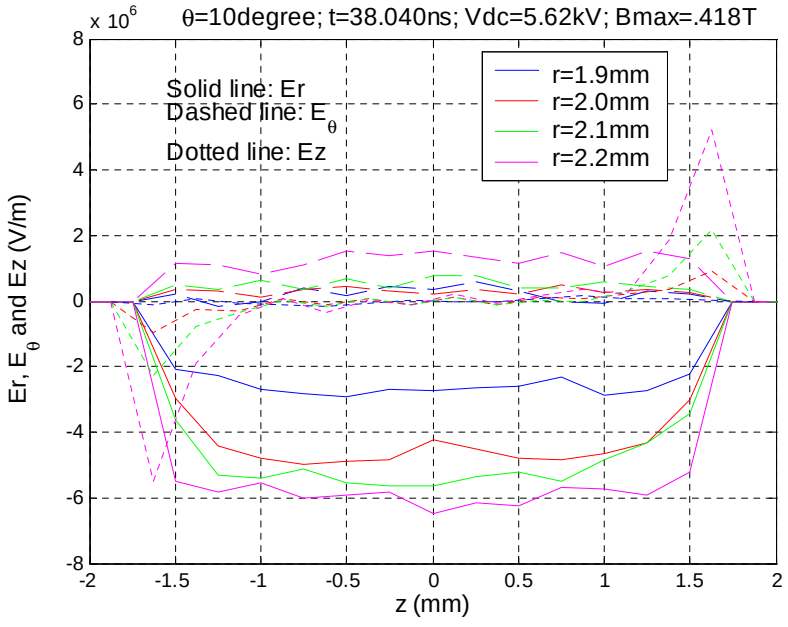

(b)

Figure 6.6: Electric field distribution along the cathode length at different azimuthal positions. $V_{dc} = 5.62kV$, real magnetic field B_{max} 0.418T. (a) Opposite the vane, $\theta = 0°$ (b) Opposite the cavity, $\theta = 10°$

does not vary much, but the sign of the B_r component changes along the cathode length, its magnitude increases from zero at the cathode center to about $\pm 0.1T$ near the end

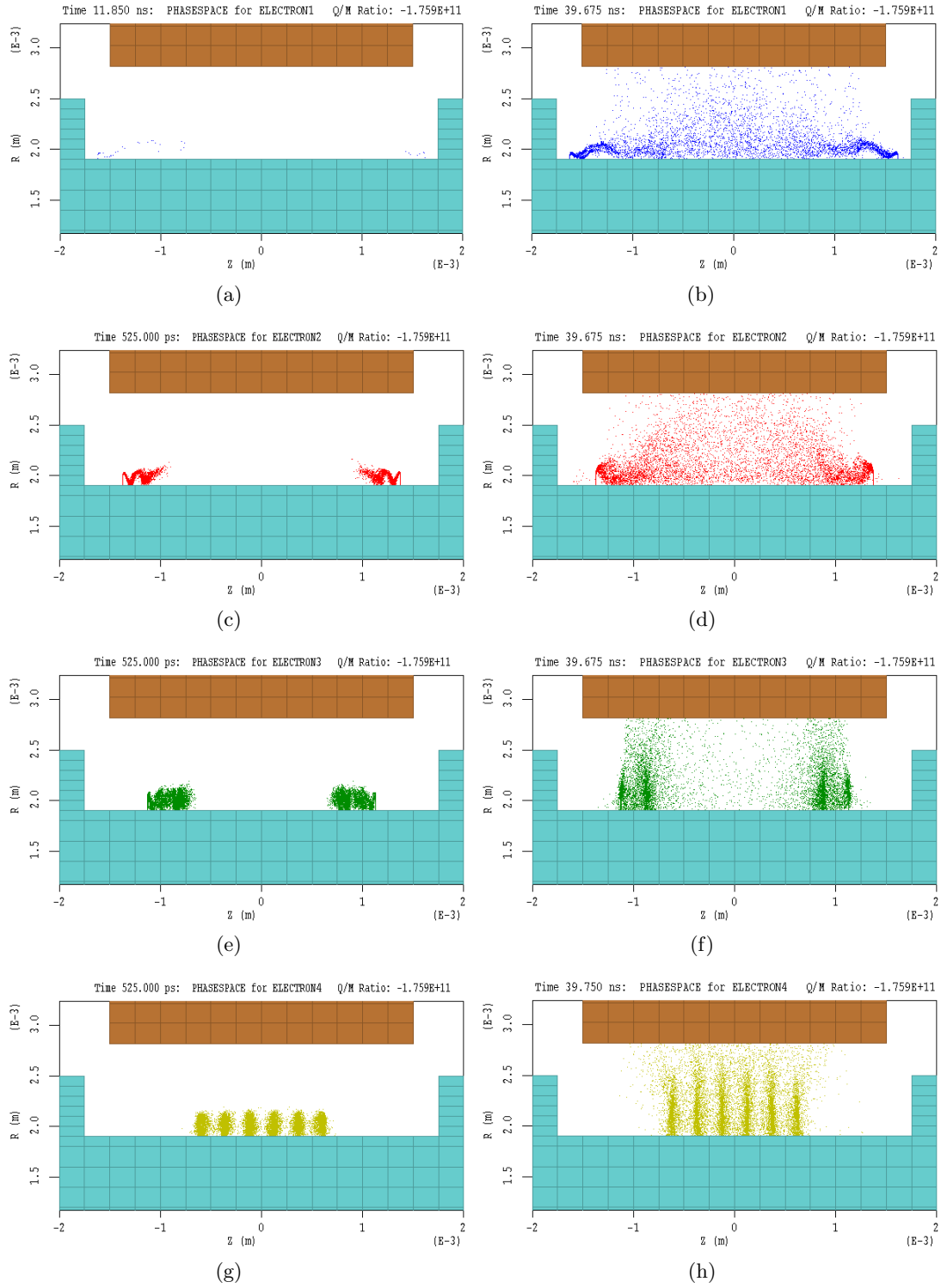

Figure 6.7: Electrons emitted from different cathode sections at the beginning of the emission (a, c, e and g) and when the magnetron is oscillating in a stable π mode (b, d, f and h) when the magnetic field is uniform. Vdc=5.70kV; Uniform B=.405T (a)(b) Electrons from rings 1 and 14 (c)(d) Electrons from rings 2 and 13 (e)(f) Electrons from rings 3, 4, 11 and 12 (g)(h) Electrons from rings 5 to 10.

hat.

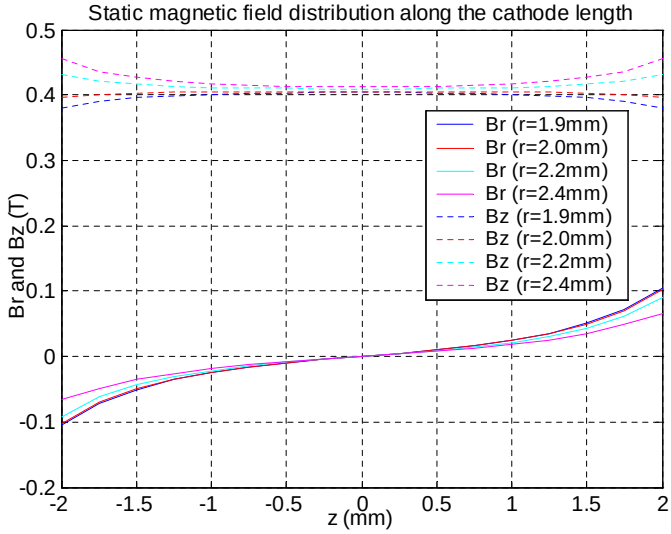

Figure 6.8: Real magnetic field (Bz and Br) distribution along the cathode length, B_{max}=0.418T.

The B_r component exerts an axial Lorentz force on the electrons near the end hats, $\vec{F_z} = \hat{z}ev_\perp B_r$. Together with the eE_z force, the net effect is for the electrons to move towards the end hats, causing the space charge density to grow there. With the space-charge-limited emission model, emission from these areas will hence be suppressed. That's the reason of the cathode emission distribution being roughly in Gaussian shape when the real magnetic field is used. Figure 6.9 illustrates the electron cloud emitted from different cathode sections at the beginning of the cathode emission and when the magnetron oscillates in a stable π mode. It can be seen that the electrons tend to move towards the two ends of the cathode.

In back bombardment the electron motion is more complicated, but according to the above analysis, the difference in the back bombardment distributions along the cathode length when uniform and non-uniform magnetic fields are applied is also due to the axial Lorentz force generated by the B_r component of the field.

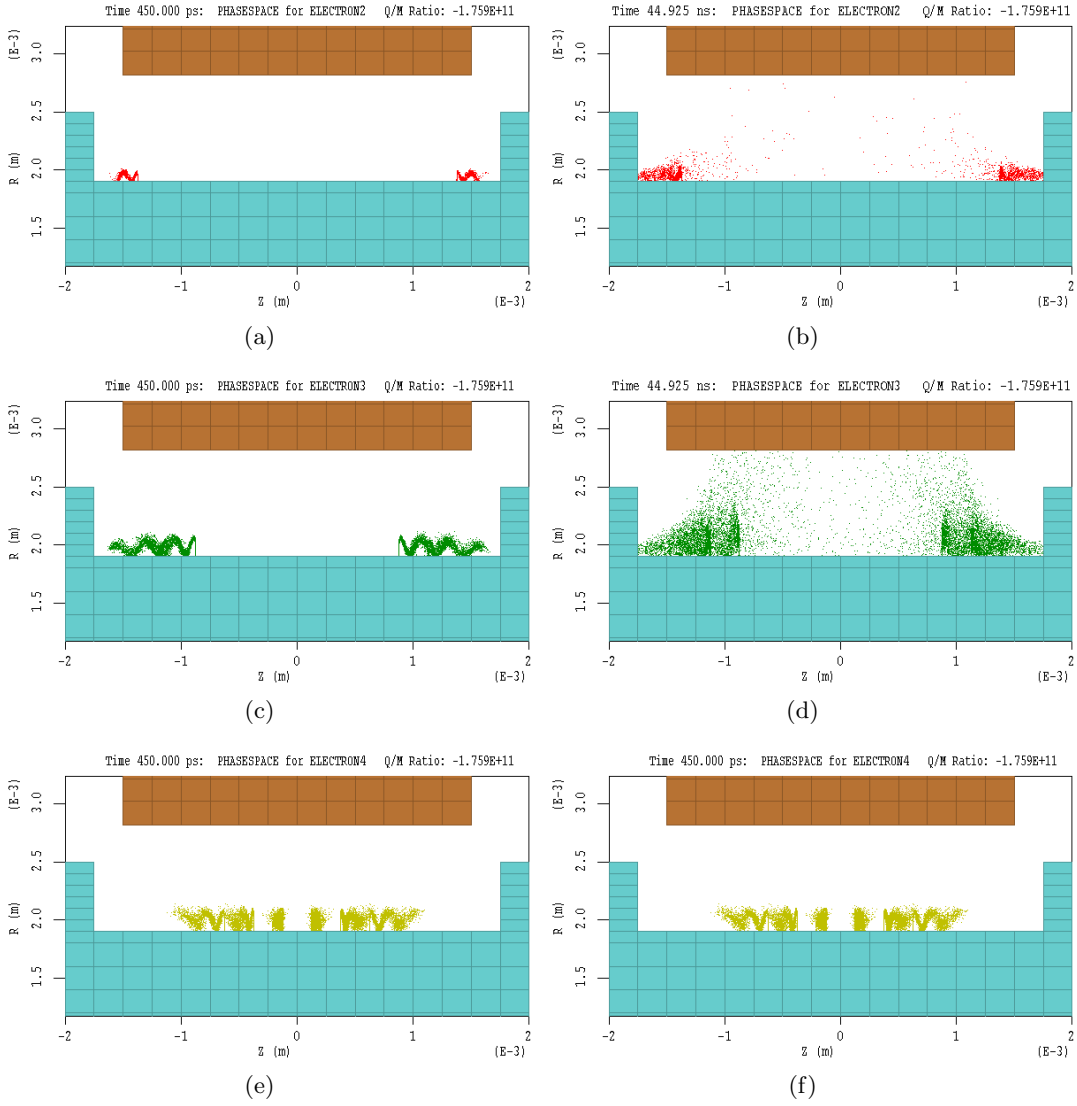

Figure 6.9: Electrons emitted from different cathode sections at the beginning of the cathode emission (a, c and e) and when the magnetron is oscillating in a stable π mode (b, d and f) using the real magnetic field distribution. Vdc=5.62kV; B_{max}=0.418T. Very few electrons are emitted from the two rings 1 and 14, therefore no electron cloud diagrams are displayed for those two sections. (a)(b) Electrons from rings 2 and 13 (c)(d) Electrons from rings 3, 4, 11 and 12 (e)(f) Electrons from rings 5 to 10.

6.4 Investigation of the Beam Emission Model

In Chapter 5, the X band magnetron has been investigated using both space-charge-limited cathode emission and a beam emission model, the back bombardment distribution of the beam emission model will therefore be investigated here for comparison. The beam

emission model assumes an initial voltage of 5eV and we have chosen beam current density of $15A/cm^2$. With the beam emission model, the cathode emission current density distribution is uniform along the whole cathode length. Here our investigations are focused on the back bombardment and its distribution. Modelling has been carried out with both uniform and real magnetic field distributions. Figures 6.10 and 6.11 show the back bombardment current density and the back bombardment voltage distribution with uniform and real magnetic fields respectively. Table 6-C summarizes the simulation results.

Table 6-C: Simulations of beam emission with uniform and non-uniform magnetic fields

Cathode emission model	Beam current density:15A/cm2 Beam voltage:5eV	
Effective input voltage (kV)	5.75	5.62
Magnetic field (T)	Real B field: B_{max}=0.418	Uniform B=0.405T
Anode current (A)	2.08	3.21
Input power (kW)	12.0	18.28
Output power (kW)	7.12	10.58
Vane voltage (kV)	3.73	4.54
Electronic efficiency (%)	59.3	57.9

It can be seen from Figure 6.10 that the back bombardment current density distributions are more or less uniform in the centeral region of the cathode irrespective of whether uniform or real magnetic field is used. But the back bombardment voltage distribution presents a very different picture. When a real magnetic field is applied, the back bombardment voltage has a Gaussian distribution, which is consistent with the results obtained in the case of a space-charge-limited emission; but when the uniform magnetic field is applied, the distribution is roughly uniform except two spikes occurring at rings 3 and 12. A detailed explanation for the two spikes must be quite involved because of the complicated motion of the electrons. But the reason for the spikes again must lie in an unrealistically uniform magnetic field distribution, as indicated in the previous section.

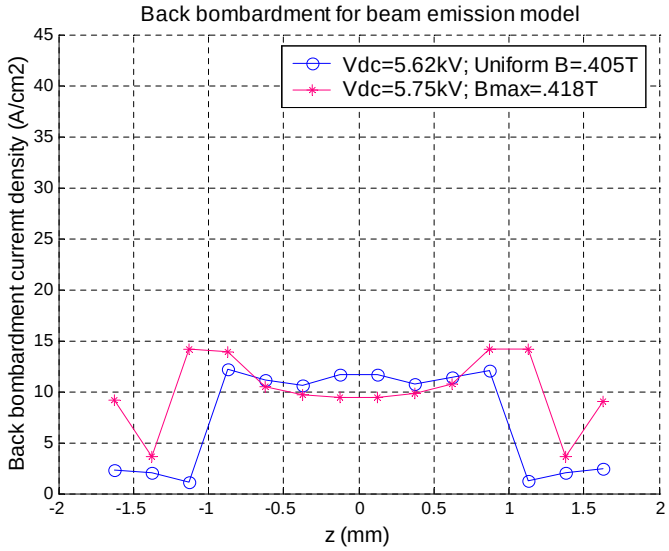

Figure 6.10: Back bombardment current density distribution with beam emission model

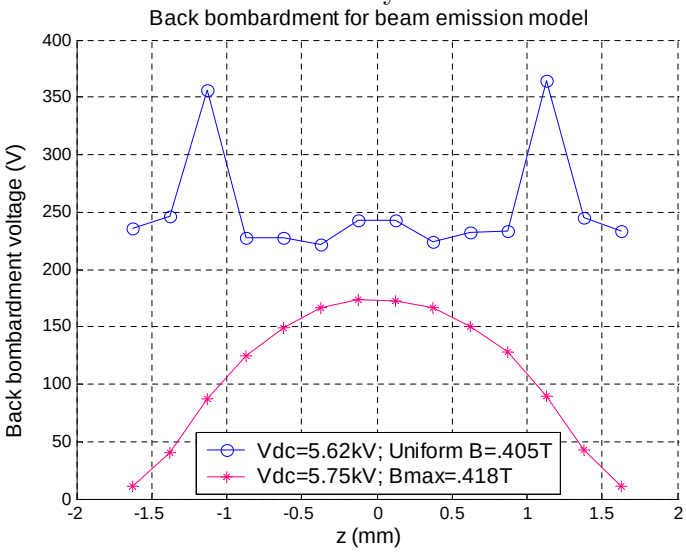

Figure 6.11: Back bombardment voltage distribution with beam emission model

6.5 Influence of a Non-Uniform Cathode Emission on the Operation of a Magnetron

The existence of a non-uniform back bombardment distribution has been demonstrated in the previous sections. This phenomenon confirms that the cathode emission must be non-uniformly distributed when the secondary emission process is included. Currently a complete model of performance including secondary emission is numerically unstable.

Therefore instead of introducing the secondary emission into the full magnetron model, the non-uniformity of the cathode emission has been represented in a simple way by applying different emission profiles along the cathode surface. Although the actual cathode emission profile, including secondary emission, is yet not fully known, the effects of a non-uniform emission can be investigated. It is hoped that this is way some useful information can be revealed on the relation between magnetron operation and the non-uniform cathode emission.

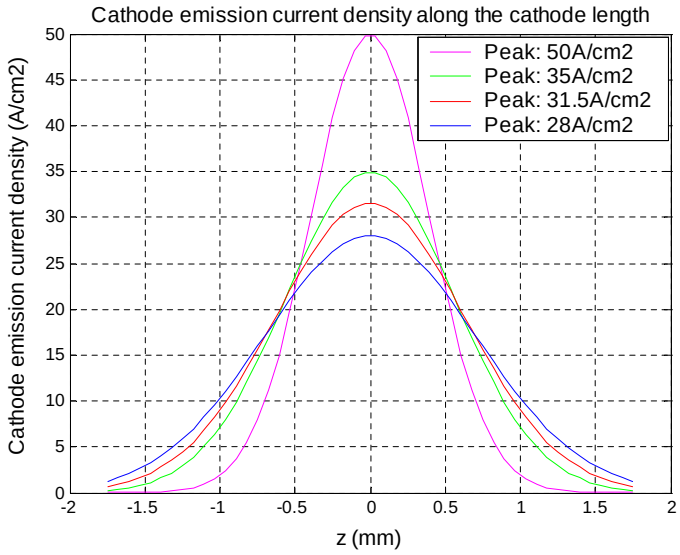

Figure 6.12: Cathode emission current density distributions (Total emission current is about 5.89A for all emission profiles)

All our cathode emission profiles are Gaussian. Figure 6.12 shows several cathode emission current density distributions along the cathode length, each with a different peak value.

Table 6-D: Simulation runs with different cathode emission current density distributions

Peak cathode emission current density	$28A/cm^2$	$31.5A/cm^2$	$35A/cm^2$	$50A/cm^2$
Effective input voltage (kV)	5.73	5.73	5.73	5.72
Anode current (A)	2.50	2.65	2.80	3.17
Input power (kW)	14.5	15.3	16.3	18.3
Output power (kW)	8.0	8.4	8.7	9.4
Electronic efficiency (%)	55.1	54.5	53.5	51.2

Following the modelling results of Chapter 5, here the total emission current has

been adjusted to about 5.89A, which is close to the cathode emission current with a uniform beam emission current density of $15A/cm^2$. The peak current densities range from $28A/cm^2$ to $50A/cm^2$. The simulation results are summarized in Table 6-D. It can be seen that the anode current and output power increase when the peak cathode emission density is increased and thus the shape of the Gaussian distribution is narrowed. However the anode current is increased more than the output power, so the efficiency would decrease. Figure 6.13 illustrates the variations of the anode current and the overall efficiency against the peak cathode emission current density. This shows that the variation of the cathode emission distribution affects the magnetron efficiency by about 4%.

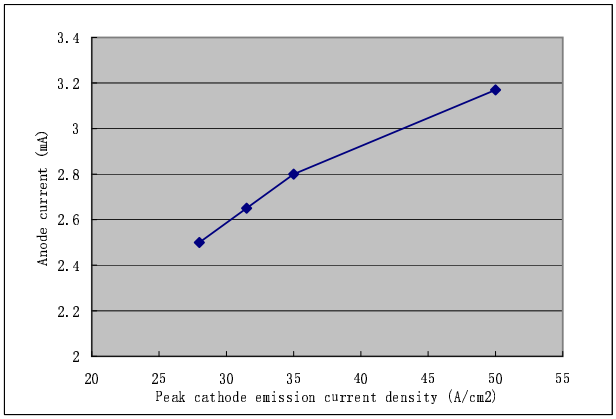

(a)

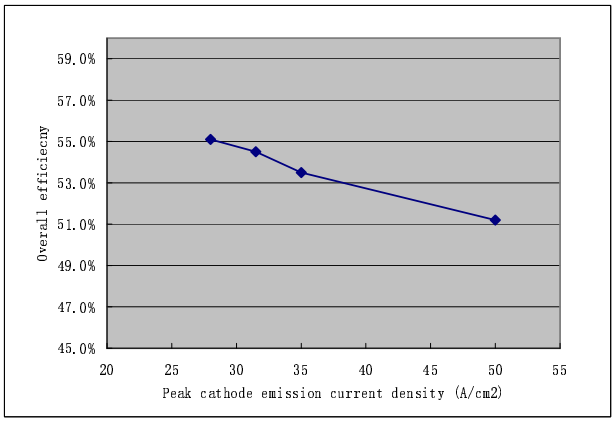

(b)

Figure 6.13: (a) Anode current vs Peak cathode emission current density. (b) Overall efficiency vs Peak cathode emission current density.

6.6 Summary

In this chapter, the cathode emission and electron back bombardment distributions along the cathode length have been investigated for both space-charge-limited emission model and beam emission model. Their non-uniform distribution along the cathode length have been demonstrated for the first time using computer modelling. It has been found that the axial Lorentz force caused by the B_r component of the magnetic field plays an important role in shaping the distributions. Since a non-uniform back bombardment distribution obviously would affect secondary emission, different Gaussian cathode emission profiles have been used to check their effect on the magnetron performance. It has been shown that the cathode emission profiles only affect the magnetron efficiency to a small extent.

Chapter 7

The Effect of Cathode Emission Voltage

7.1 Introduction

One significant difference between our current computer model and the real magnetron is that only the primary emission is modelled, while in a real magnetron the cathode emission comprises both primary and secondary emission. In all previous modelling, the initial cathode emission voltage is very low, at most a few volts, whether we use a space-charge-limited or a beam emission model; these values are typical of thermionic emission. However experimental results have shown that at some circumstances high energy secondaries are present in an oscillating magnetron. Figure 7.1 shows energy distributions of secondary electrons emitted by silver [1, 2]. There are three regions in the diagram, representing the true secondaries (below 50eV), inelastically reflected or rediffused primaries (above 50eV, but below the primary energy) and elastically reflected primaries (near the primary energy). Will these high energy 'secondaries' affect magnetron operation significantly? Our investigations carried out by using computer modelling have indicated, as described in this Chapter, that the energy distribution of the back bombardment elec-

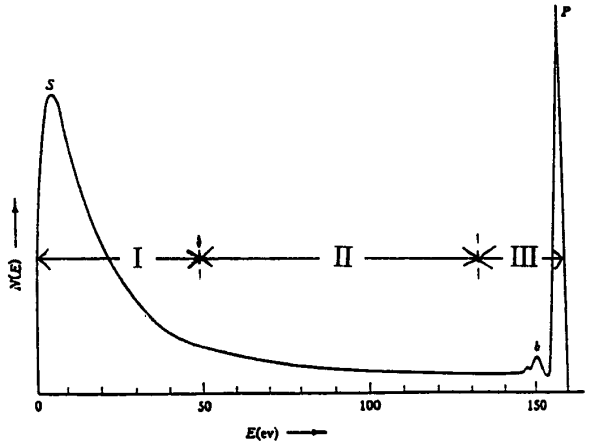

Figure 7.1: Energy distribution of secondary electrons emitted by silver [1]

trons is quite high, a significant fraction having kinetic energy large enough to produce high energy secondary electrons. Since at present a MAGIC model of secondary emission becomes numerically unstable, we have artificially increased initial cathode emission voltage in order to partially simulate the process.

7.2 Energy Distribution of Electron Back Bombarding

In order to estimate the energy of secondary electrons, the energy distribution of the back bombarding primary electrons has been investigated. Modelling has been carried out with anode currents of 3.60A, 4.13A and 5.14A respectively. Simulation results show that the back bombardment energy distribution ranges from 0eV to 500eV when the anode current is 3.60A; the upper limit of the back bombardment energy increases to 600eV when the anode current reaches 5.14A. Table 7-A presents simulation results with I_a = 3.60A, 4.30A and 5.14A; for average initial cathode emission voltages of 4.0eV, 5.0eV and 5.7eV, the average back bombardment voltages are respectively 130eV, 147eV and 163eV.

Figure 7.2 shows the energy distribution at different time intervals when the magnetron is oscillating in a stable π mode and the anode current is 5.14A. It can be seen

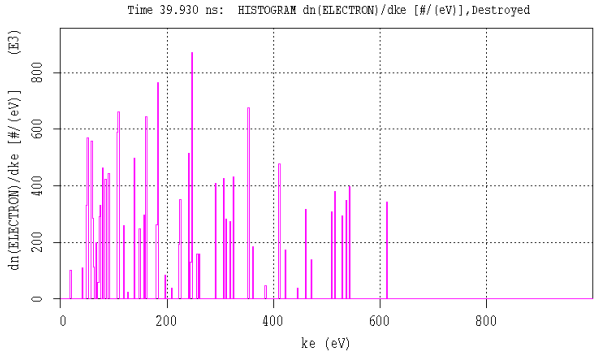

(a)

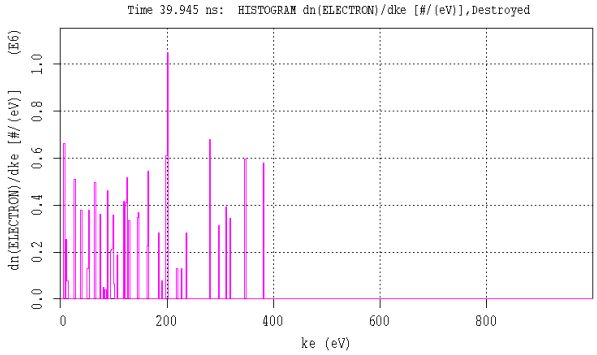

(b)

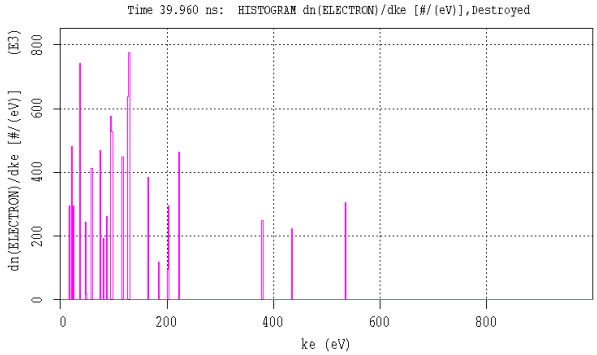

(c)

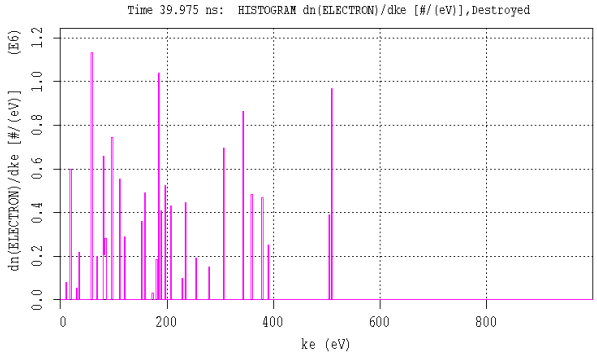

(d)

Figure 7.2: The back bombardment energy distribution at different time intervals. Vdc=5.87kV, Ia=5.14A. (a). t1=39.930ns (b). t2=t1+0.14RFperiod (c). t3=t1+0.28RFperiod (d). t4=t1+0.42RFperiod

Table 7-A: The average electron back bombardment energy at different anode currents

Emission model: space-charge-limited			
Magnetic field: $B_{max} = 0.418T$			
Effective input voltage (kV)	5.70	5.79	5.87
Anode current (A)	3.60	4.35	5.14
Output power (kW)	13.77	16.35	19.0
Overall efficiency	57.0%	55.2%	53.5%
Average emission voltage (V)	4.0	5.0	5.7
Average back bombarding voltage (V)	130	147	163

that a significant fraction of the back bombarding electrons exhibit kinetic energy higher than 100eV; this is large enough to produce high energy secondaries. Figures 7.3 and 7.4 provide a contour distribution along the cathode length of the electron back bombardment energy taken at the same time intervals as in Figure 7.2. Figure 7.5 presents the RF voltage between two adjacent anode vanes during one RF cycle. The red stars '$*$' denote the instants when the electron back bombardment energy has been calculated.

In Figures 7.2, 7.3 and 7.4, the electron back bombardment energy distribution has been obtained over a very short accumulation time of 75fs, which is about 1/700 of one RF cycle. It is desirable to evaluate the electron back bombardment energy distribution over a longer period. Figure 7.6 shows the electron back bombardment energy distribution measured over 10RF cycles when the magnetron is in stable π mode oscillations. It can be noticed from this figure that maximum back bombardment occurs at 30eV and that 57% of the total back bombarding electrons have kinetic energy in excess of 100eV. This again suggests a possible mechanism for generating in large numbers high energy secondary electrons.

The above results indicate that in the real operation of a magnetron, the initial velocity, or the initial voltage of a fraction of the cathode emitted electrons can be up to several hundred volts. But in our current modelling, the initial voltage of the emitted electrons is only a few volts for either space-charge-limited or beam emission model. This justifies further investigation using high initial voltage of the emitted electrons.

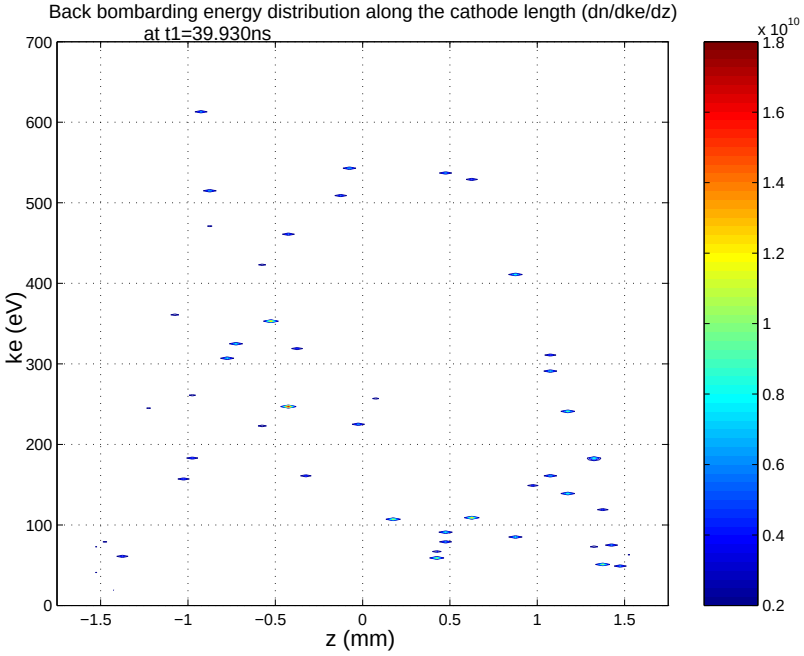

(a)

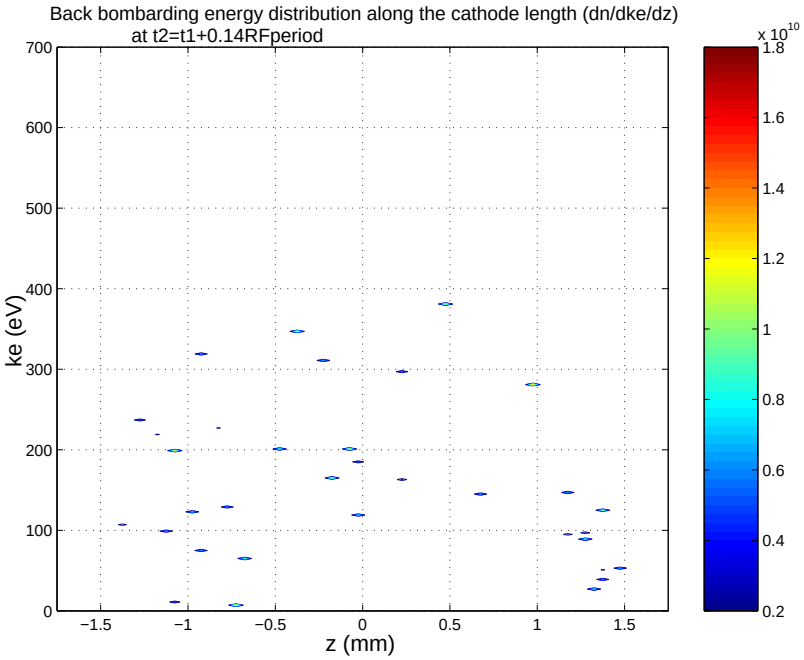

(b)

Figure 7.3: The back bombardment energy distribution along the cathode at different time intervals. Vdc=5.87kV, Ia=5.14A. (a) t1=39.930ns (b) t2=t1+0.14RFperiod

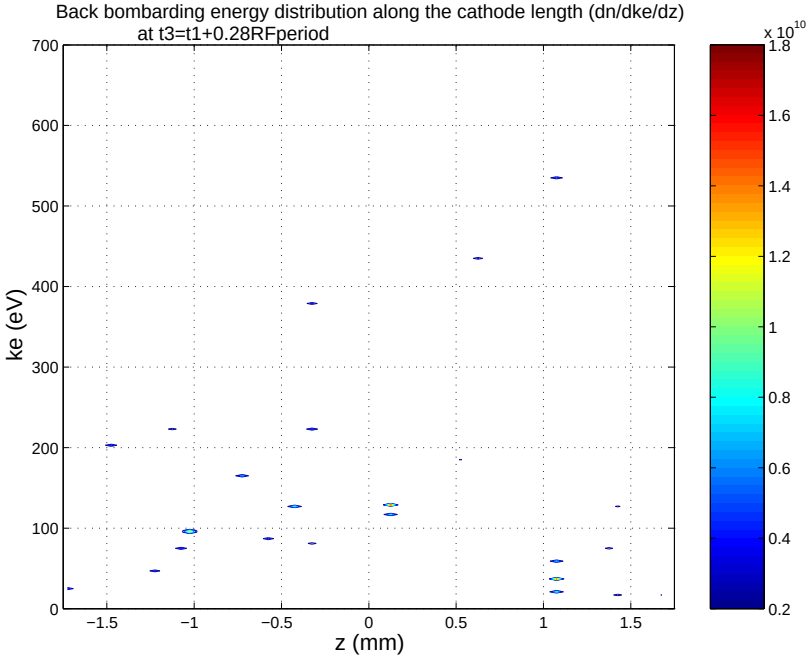

(a)

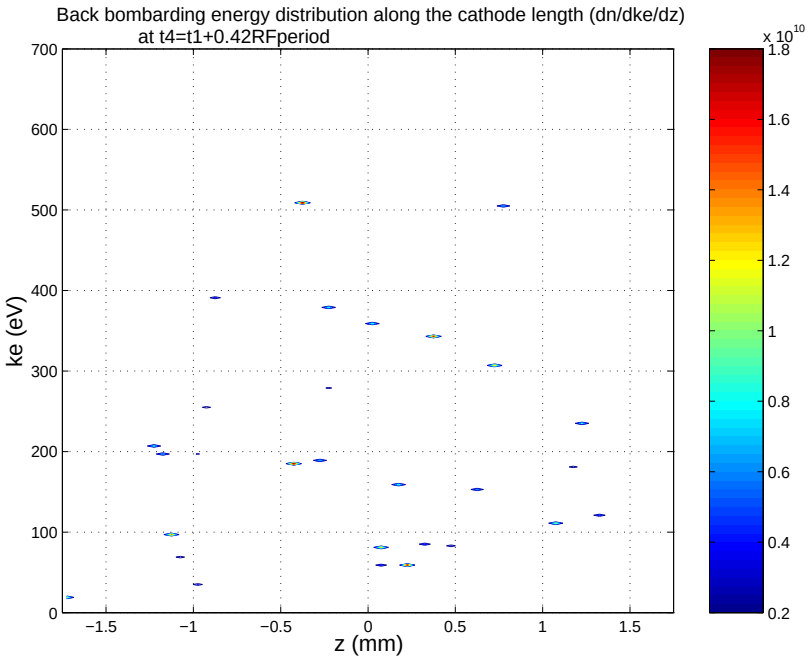

(b)

Figure 7.4: The back bombardment energy distribution along the cathode at different time intervals. Vdc=5.87kV, Ia=5.14A. (a) t3=t1+0.28RFperiod (b) t4=t1+0.42RFperiod

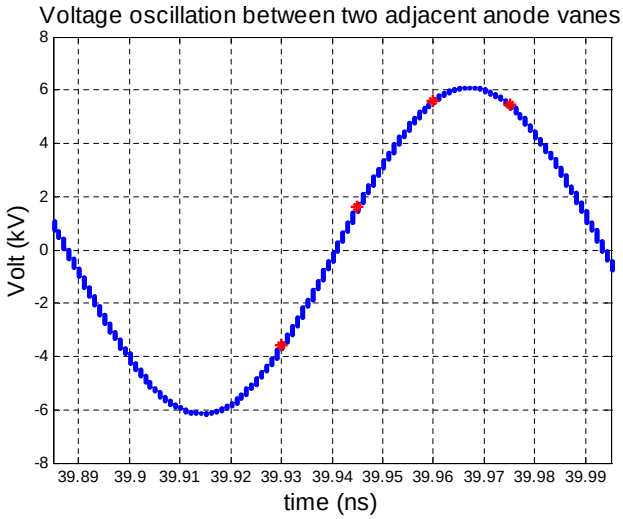

Figure 7.5: The RF voltage between adjacent anode vanes within one RF cycle. Vdc=5.87kV, Ia=5.14A. Electron back bombardment energy distributions shown in Figures 7.2, 7.3 and 7.4 have been calculated at points indicated by a red star '∗'.

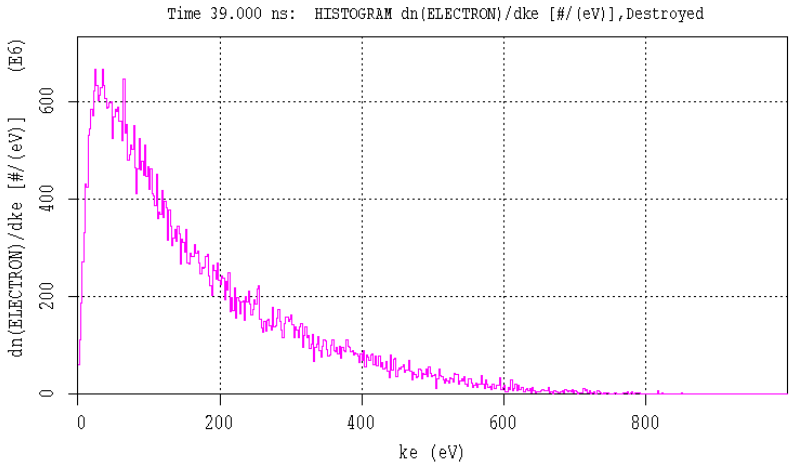

Figure 7.6: The electron back bombarding energy distribution measured over 10RF cycles.

7.3 High Initial Cathode Emission Velocity

Since a direct simulation of cathode secondary emission is not yet possible, an equivalent method has been developed to investigate the effect. The space-charge-limited emission model has been modified with an artificially high initial velocity spread in order to simulate high energy secondary emission. Basically the velocity distribution of the emitted electrons is Maxwellian, multiplied by the sine-of-polar angle from vertical.

A number of simulation runs have been carried out using various peak values. For simplicity, the average emission voltage is used to evaluate the initial velocity of emission.

Table 7-B: Magnetron performance as a function of the initial velocity of the emitted electrons

Effective input voltage (kV)	5.70	5.70	5.69	5.68	5.68
Anode current (A)	3.60	3.86	4.03	4.29	4.45
System RF energy ($1 \times 10^{-6} J$)	52.11	49.25	48.2	47.32	46.58
Output power (kW)	13.77	13.18	12.92	12.72	12.52
Overall efficiency	57.0%	50.9%	47.9%	44.4%	42.1%
Back bombarding power (kW)	0.807	1.49	1.95	2.68	3.24
Average cathode emission power (kW)	0.040	0.709	1.25	2.14	2.81
Average cathode emission voltage (V)	4.0	54.5	87.3	134.6	167.1
Average back bombarding voltage (V)	130	168	197	241	273
Vane voltage (kV)	5.18	5.05	5.02	4.95	4.92

Table 7-B summarizes the simulation results. The anode voltages is kept constant at around 5.70kV. When the average initial velocity is increased from 4eV to 167eV, the anode current grows from 3.60A to 4.45A; the output power decreases from 13.77kW to 12.52kW; therefore the overall efficiency decreases from 57.0% to 42.1%. The explanation is that when electrons are emitted with high initial velocity, some synchronous electrons loss their excess kinetic energy by striking the anode. This reduces the overall efficiency, even though there is more DC power being supplied. Figure 7.7 compares the electron cloud when the initial velocity is 4eV and 100eV. With the average initial velocity of 4eV, the electron spokes are well defined; when the initial velocity is increased to 100eV, the spokes become blurred and get bigger, indicating a wide energy spread among asynchronous electrons.

Another phenomenon to note is that when the cathode emission velocity is increased, the cathode emission power significantly changes from 40Watts to 2.81kW. In magnetron operation, the only power source is the DC power supply, so the extra emission power is thought to come from the back bombardment, which has been shown to produce high energy secondary emission.

Thus, by increasing the cathode emission voltage, one can reduce the computed

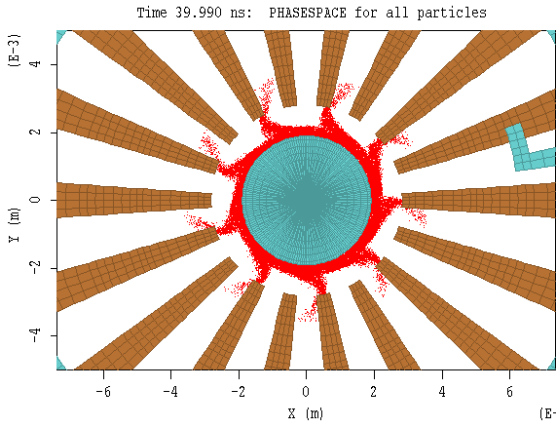

(a)

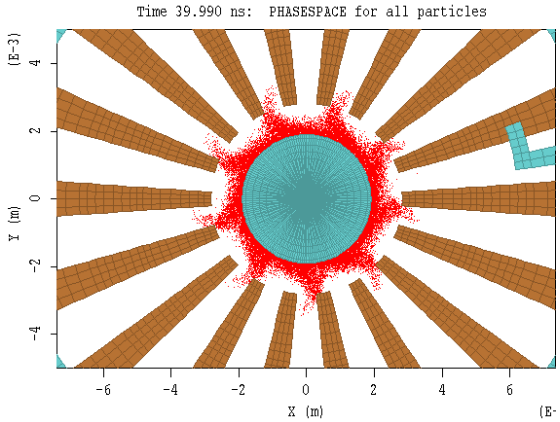

(b)

Figure 7.7: Electron clouds in stable π mode oscillations with different cathode emission initial velocities. (a). The average initial velocity of cathode emission is 4eV. (b) The average initial velocity of cathode emission is 167eV.

efficiency of the magnetron significantly and bring it close to the experimental result.

7.4 Summary

By investigating the energy spread of the back bombarding electrons, it is shown that the X band magnetron is capable of producing high energy secondary electrons. Simulations have then been carried out with an artificially increased emission voltage in order to investigate the effect of high energy secondary electrons. It is found that when the initial voltage is increased from 4eV to 167eV, the overall efficiency of the X band magnetron

drops from 57.0% to 42.1%. It is concluded that the high energy secondary emission is the main reason for the low efficiency of the X band magnetron.

References

[1] D.Chernin, A.Drobot, and M.Kress, "A model of secondary emission for use in computer simulation of vacuum electronic devices," in *Eelctron Devices Meeting*, ser. Technical Digest., International, Dec 1993, pp. 773–776.

[2] J.Rodney and M.Vaughan, "A new formula for secondary emission yield," *IEEE Transactions on Electron Devices*, vol. 36, no. 9, pp. 1963–1967, Sept. 1989.

Chapter 8

Conclusions and Future work

8.1 Conclusions

The research presented in this thesis comprises 3D computer modelling of magnetrons using an FDTD/PIC code called MAGIC. The modelling process has been vastly extended to include realistic performance details of two e2v technologies' S and X magnetrons, all in close collaboration with e2v engineers. Considerable insight into the characteristics of magnetron operation have been gained through modelling. The following is a summary of the key items considered in this work.

1. Investigation of the melting of the output coupling rods in the S band MG5193 magnetron.

    - It is found that when the glass dome is replaced by a ceramic one, the impedance match is improved, therefore the RF power reflection cannot be the reason for the melting of the rods.

    - Investigation of the RF current distribution along coupling rods shows that the RF current in the input coax is much higher than that on the coupling rods, therefore RF current overheating can also be eliminated as the cause for

rod melting.

- Preliminary work on a multipactor effect indicates that electron bombarding of the coupling rods and of the central support could last long enough to cause melting.

2. Analysis of the frequency spectrum of an S band anode (e2v MG5193).

   A computer model for an S band anode has been optimised by considering the bare anode and the strapping system. When a 'tuner' is included, simulation spectrum agrees well with experimental result.

3. Simplification and approximation rules in setting up a computer model for the whole magnetron.

   There are two important aspects in building a computer model. One is to fit the model to the code's underlying symmetry in order to maximise computing efficiency. Another is that when an approximation cannot be avoided, it should be kept away from the beam/wave interaction region. Based on these two rules, a 'thick tapering' vane model is selected for the X band (MG5241) magnetron as being the best fit.

4. Investigation of a high overall efficiency of the X band magnetron model.

   In hot test modelling two different cathode emission models have been used, the space-charge-limited model and the beam emission model. Both models yield higher overall efficiency than that of a real magnetron. Possible reasons for the efficiency discrepancy have been investigated, including the end hats emission, the output coupling circuit, the copper surface losses and the rising rate of voltage, but all have failed in explaining the effect. However, the above investigations have revealed some interesting features of operation of magnetrons, such as the role of the end hat emission, the relationship between the output coupling loop area and the Q_{ext}, the oscillation start-up and its dependence on the rate of rise of anode

voltage.

5. Investigation of non-uniform cathode emission and back bombardment distribution in the X band magnetron.

   Both non-uniform cathode emission and back bombardment distribution have been demonstrated for the first time by computer modelling; this indicates the inherent complexity of the cathode emission process when secondary emission is included. Investigation of uniform and non-uniform or real magnetic field distribution clearly shows that the B_r component plays an important role in the cathode emission and back bombardment distribution pattern along the cathode. Artificially created cathode emission distribution of Gaussian shape has been used to show that different emission profiles can cause marked differences in the overall efficiency.

6. Investigation of the effect of high initial velocity of emission.

   Investigation of the energy spread in back bombardment electrons hitting the cathode indicates that high energy secondary emission is present in the X band magnetron. Since a direct simulation of cathode secondary emission so far proved to be numerically unstable, simulation with artificially increased initial electron velocity has been substituted. The results show that a high initial velocity of cathode emission reduces the overall efficiency significantly. A clear conclusion is that a high energy secondary emission is capable of substantially lowering the efficiency of a magnetron.

As mentioned in Chapter 1, it is hoped that our computer modelling should help to substantially reduce the time and cost of development of new devices. In our project, a range of modelling techniques has been developed towards this objective. Though there are still limitations in current magnetron modelling, such as proper simulation of secondary electrons and the modulator/magnetron interaction, at least we were able to show that computer modelling is an effective and reliable way to investigate magnetron operation.

8.2 Future Work

At this stage various details of operation of the X band magnetron have been investigated and the reason for the low operating efficiency has been deduced. Future work should be concerned with magnetron/modulator interaction and with further development of secondary emission model.

1. Magnetron/Modulator interaction

   The start-up of oscillations is important in magnetron operation, it is then that mode competition and stability problems occur. In section 5.9, the magnetron start-up of oscillations has been investigated, preliminarily by simulating a slow RRV. But this investigation cannot provide adequate information because the influence of the modulator is not included in the computer model, even though the modulator plays an important role in magnetron operation. The interaction between the magnetron and the modulator determines the rate of rise up of anode voltage. Investigation of the magnetron/modulator interaction process is therefore strongly recommended to be carried out in the future.

2. Cathode emission

   Our current investigation of cathode high energy secondary emission has shown that it reduces the magnetron efficiency significantly. To confirm this observation, a magnetron that does not depend on secondary emission from the cathode (e.g. BM75L) should be modelled to see if the computer predicted electronic efficiency agrees with measured values.

   At this stage of work, the energy distribution of cathode emitted electrons is artificial, whether it is maxwellian or uniform. It is necessary and of considerable interest to investigate the real energy distribution of the cathode emission and its possible effect on magnetron operation.

Appendix A

Definitions of Qs and Circuit Efficiency

The definitions of the external Q, loaded Q and internal Q of a resonant cavity are given below [1, 2]

$$Q_{ext} = 2\pi f_0 \frac{W}{P_{out}} \tag{A.1}$$

$$Q_{load} = 2\pi f_0 \frac{W}{P_{out} + P_{loss}} \tag{A.2}$$

$$Q_0 = 2\pi f_0 \frac{W}{P_{loss}} \tag{A.3}$$

where W is the system's stored RF energy, f_0 is the resonant frequency, P_{out} is the output power and P_{loss} is the cavity copper surfacer loss. Substituting equations A.1 and A.2 in equation A.3, the Q_0 can be expressed in terms of Q_{ext} and Q_{load} by writing

$$Q_0 = \frac{Q_{ext} Q_{load}}{Q_{ext} - Q_{load}} \tag{A.4}$$

When Q_{ext} and Q_{load} are obtained using computer simulation, Q_0 can then be obtained from A.4.

The circuit efficiency of the cavity is $< 100\%$ due to copper surface losses and it can be expressed in terms of the Qs.

$$\eta_{cold} = \frac{Q_{load}}{Q_{ext}} \tag{A.5}$$

or

$$\eta_{cold} = \frac{1}{1 + \frac{Q_{ext}}{Q_0}} \tag{A.6}$$

References

[1] S.Y.Liao, Ed., *Microwave devices and circuits.* Prentice Hall Internationsl, 1990.

[2] J.D.Kraus and D.A.Fleisch, Eds., *Electromagnetics with Applications.* WCB McGraw-Hill, 1999.

Appendix B

Author's Publications

Journal Papers

1. L. Ma, X. Chen, M. Esterson and P. Lindsay, "The effects of the initial velocity of cathode emission in an X band magnetron," *in preparation* .

Conference Papers

1. **L. Ma**, X. Chen, M. Esterson and P.A. Lindsay, "Computer Modelling of the Possible Multipactor Effect in the Output System of an Experimental S Band Magnetron", *3rd IEEE International Vacuum Electronics Conference*, Monterey, California, USA, April 2002, pp. 246.

2. **L. Ma**, X. Chen, M. Esterson, P.A. Lindsay, P. Burleigh and M. Brady "3D Computer Modelling of an X band Magnetron", in *4th IEEE International Vacuum Electronics Conference*, Seoul, Korea, April 2003, pp. 281.

3. **L. Ma**, X. Chen, M. Esterson, P.A. Lindsay, P. Burleigh and M. Brady, "3D cold test modelling of an S band magnetron", in *9th International Conference on Microwave & RF Heating*, Loughborough University, UK, Sept 2003, pp. 233.

4. **L. Ma**, X. Chen, M. Esterson, P.A. Lindsay, P. Burleigh, K. Saleem and D. Wilson, "Investigation of an X band experimental magnetron through MAGIC modelling", in *31st IEEE International Conference on Plasma Science*,Baltimore, Maryland, May 2004, pp. 177.

5. **L. Ma**, X. Chen, M. Esterson, P.A. Lindsay, P. Burleigh, K. Saleem and D. Wilson, "Investigation of the non-uniform back bombardment of an X band magnetron", in *MAGIC user group meeting, 31st IEEE International Conference on Plasma Science*,Baltimore, Maryland, May 2004.

Project reports

1. **L. Ma**, X. Chen, P.A. Lindsay and M. Esterson, "Computer Modelling of X Band Magnetron", 1^{st} Oct. 2003 $\sim$ 30^{th} Oct. 2004.

2. **L. Ma**, X. Chen, P.A. Lindsay and M. Esterson, "Computer Modelling of X Band Magnetrons", 1^{st} Oct. 2002 $\sim$ 30^{th} Oct. 2003.

3. **L. Ma**, X. Chen, P.A. Lindsay and M. Esterson, "Computer Modelling of S/X Band Magnetrons", 1^{st} Oct. 2001 $\sim$ 30^{th} Oct. 2002.